ANALYSIS OF SPATIAL FILTERING IN PHASE-BASED MICROWAVE MEASUREMENTS OF TURBINE BLADE TIPS

A Thesis
Presented to
The Academic Faculty

By

Thomas Arthur Holst

In Partial Fulfillment
Of the Requirements for the Degree
Master of Science in Mechanical Engineering

Georgia Institute of Technology

August, 2005

ANALYSIS OF SPATIAL FILTERING IN PHASE-BASED MICROWAVE

MEASUREMENTS OF TURBINE BLADE TIPS

Approved By:

Dr. Thomas R. Kurfess, Advisor
College of Engineering
Georgia Institute of Technology

Dr. W. Steven Johnson
College of Engineering
Georgia Institute of Technology

Dr. Jerrol W. Littles, Jr.
Pratt & Whitney

Dr. Shreyes N. Melkote
College of Engineering
Georgia Institute of Technology

Date Approved: May 20, 2005

ACKNOWLEDGEMENTS

This work is not truly the work of the author alone; rather, the author owes a costly debt of gratitude to those surrounding him who have assisted and guided him along the way. First, the author would like to acknowledge his advisor, Dr. Thomas Kurfess for his encouragement and effort toward making this thesis a possibility. Without the seed that Dr. Kurfess planted in beginning this project, it would never have come to fruition. The author would also like to thank the rest of his committee for taking the time to evaluate and add insight into this work.

The author would like to thank all of the employees of Radatec, Inc. for their support throughout the project. It is these men who have worked with the author through all aspects of the project—from the overarching planning and strategizing to the fine and practical details of the research. Especially, the author would like to acknowledge Scott Billington and Jon Geisheimer for countless hours of labor toward this end.

The greatest debt of gratitude the author owes is the one he owes his wife, Katie Holst. She, more than any other, has stood with him, encouraging him and helping him to press on to the goal. She has stayed up late with him, gotten up early with him, fought to keep him well-fed and healthy, endured hours of monotonous work, and spent many lonely nights all in order that he should complete his task. It is her love that has kept him going.

Finally, the author would like to recognize that all honor and esteem received is due to God for allowing this to occur. It is for his glory that the universe exists and it is for his glory that this thesis has been completed.

TABLE OF CONTENTS

LIST OF TABLES

LIST OF FIGURES

LIST OF SYMBOLS AND ABBREVIATIONS

(Symbols and abbreviations are listed in order of appearance)

Symbol or Abbreviation	Definition
PHM	Prognostics and Health Monitoring
DARPA	Defense Advanced Research Projects Agency
DSO	Defense Sciences Office
TOA	time-of-arrival
ATS	Advanced Turbine System
FOD	foreign object damage
FMCP	frequency modulated capacitance probe
C	Capacitance
E	dielectric constant
S	common capacitance area
D	Distance
IFOLP	integrated fiber optic laser probe
NASA	National Aeronautics and Space Administration
RADAR	radio detection and ranging
TOF	time-of-flight
T	Target
$\vec{T}$	target vector
c_{air}	speed of light in air

P_r	received power
P_t	transmitted power
G	antenna gain
Λ	Wavelength
Σ	radar cross-section of target
CW	continuous wave
FMCW	frequency modulated continuous wave
PSF	point spread function
$d_{far\text{-}field}$	distance to the beginning of antenna far-field
D	antenna aperture diameter (or electrical length)
$d_{reactive\ near\text{-}field}$	distance to the end of antenna reactive near-field
I	Inphase channel
Q	Quadrature channel
RCS	radar cross-section
Θ	Phase
$\theta_{relative}$	relative phase change to target
θ_o	Initial system phase lag
$d_{absolute}$	absolute distance to target
λ_{air}	wavelength in air
$d_{relative}$	relative distance to target
N	integer number of full wavelengths to target
DC	direct current
CMM	coordinate measurement machine

PA	photo-acoustic
SEM	scanning electron microscopy
PC	personal computer
NI	National Instruments
DAQ	data acquisition
RF	radio frequency
PCB	personal computer board
VCO	voltage-controlled oscillator
BNC	Bayonet Neill Concelman
Pt-Pl-Ag	Platinum-Palladium-Silver
RAM	random access memory
A/D	analog to digital
P_{peak}	nodal peak power output
I_r	received signal intensity
I_s	source signal intensity
k_d	diffusion constant
N	normal vector
L	vector in direction of reflection
θ_i	angle-of-incidence
k_s	specularity constant
H	vector bisecting direction of reflection and incidence
M	shininess factor
A	Area

DOE	design of experiments
I_{DC}	Inphase DC component
Q_{DC}	Quadrature DC component
Y_i	experimental responses
β_0	regression intercept factor
β_1	regression slope factor
X_i	regression input factors
ε_i	regression errors
H_0	null hypothesis
H_a	alternate hypothesis
ANOVA	analysis of variance approach
F*	F-statistic
MSR	mean squared regression
MSE	mean-squared error
A	alpha level of significance
df_{factor}	input factor degrees of freedom
df_{data}	response degrees of freedom
C_i	confidence level
r^2	r-squared value

SUMMARY

In-process turbine measurement and monitoring has been a subject of research since the advent of gas turbines. However, obtaining these measurements is often difficult because it requires precision measurements to be made in the harsh turbine environment. The in-situ measurement of turbine blade tips is especially intriguing because of the potential it holds to increase the efficiency of engine operation and maintenance. A sensor recently developed at Georgia Tech answers this challenge. The sensor operates by measuring the phase change of reflected microwaves to measure blade tip displacement. It is robust and can operate even in the harshest turbine environments.

One characteristic of the sensor is a wide antenna pattern, which causes a phenomenon called spatial filtering to occur. Essentially, spatial filtering is a blurring of measurements. In measuring turbine blades, only the tip information is vital, and blurring is not necessarily detrimental. However, changing measurement geometry can affect the amount and character of spatial filtering and hence the accuracy of the measurement.

This thesis presents an analysis of this phenomenon, focusing on its effect on turbine blade tip measurements. A five-factor, full-factorial design of experiments is presented to qualitatively and quantitatively understand the effect of geometric factors on three different tip measurements—phase response, maximum radar cross-section (RCS), and apparent blade width. Three of the five factors change during normal turbine operation (tip clearance, tilt, and approach angle), and two of the factors resemble changes between different stages or engines (twist angle and blade width).

Phase response is the most important response to sensor operation since tip clearance measurements are directly proportional to phase response. Experimental

clearance is the only input factor that changes during normal turbine operation that has a significant affect on phase response, so use of the sensor for measurement of relative tip clearance is valid. All of the other factors have less than 1% of the influence of clearance during normal turbine operation. However, the sensor is influenced by the particular turbine geometry, so measurements are not absolute or comparable between geometrically different turbines without further development. Blade twist and width both influence phase response more than 5% of the influence of clearance over the operational range of these input factors. However, neither of these factors changes to the degree measured during actual turbine operation.

Experimentally measured maximum RCS and apparent blade width behave differently from phase response because of spatial filtering. With this additional information, it is possible to decouple clearance changes from other geometric variations. Hence, it is possible to detect changes in other of the input factors by noting changes in RCS and blade width relative to the changes in phase response. For example, blade twist causes a significant change in apparent blade width, but it does not affect phase response significantly. Therefore, a change in apparent blade width without a change in phase response possibly signifies a change in blade twist.

Along with experimentation, a three-dimensional, ray-tracing, electromagnetic model is presented, which was developed to further understand spatial filtering from a theoretical standpoint. The same set of experiments was repeated with the model, and the results are discussed and compared with the physical experiments.

In general, the model correlates with reality in the major trends while deviating in some of the less influential trends. The model is idealized, and this likely accounts for

the discrepancies. For phase response and maximum RCS, clearance is the main influencer as shown experimentally. Phase response is again only significantly influenced by clearance of the input factor that changes during normal turbine operation. Also as in experimental data, RCS and apparent blade width are more strongly affected by the other input factors than clearance. Again, it is possible with this information to decouple clearance changes from other geometric changes.

This research represents significant advance in understanding the causes and effects of spatial filtering on turbine blade tip measurements. Microwave measurements are more complex because of the nature of spatial filtering, but by analyzing the characteristics of spatial filtering in measurements, it is possible to extract previously unknown information from data.

CHAPTER 1 INTRODUCTION

Gas turbines are the standard in energy transfer for aviation and power generation. A vast number of aircraft and almost all power plants in operation today have one or more turbines as a major component of system functionality. As a result, these machines have been the subject of intense research and development so that they are among the most advanced mechanical systems in the world. The trend toward turbines as the power system of choice shows no sign of slowing. Indeed, power plants, industry, and aircraft continuously call for more powerful and efficient turbine power systems.

Much of the focus of turbine research is directed toward the development of efficient airflow, better materials, and better mechanical design. However, recent advances in computational power and information technology offer new capability to make intelligent systems that adapt in real-time to measured operating conditions. This allows systems to operate at optimal efficiency. In any case, there are two major steps to becoming an autonomous, intelligent system. The first is to gather needed data, and the second is to develop algorithms to determine an action based upon the data received. For turbines, the limiting task is the former: the most advanced mechanical systems in the world also require the most advanced sensors in the world. The environment inside of a turbine is extremely unfriendly toward sensors. Primarily, it is hot, and there are always large amounts of vibration—both of these factors make survivability a major sensor issue. In addition, large amounts of combustion products are always present, moving components travel extremely quickly, and measurements need to be exceptionally precise. These factors often make valid measurements difficult to obtain.

This thesis is one step toward the goal of developing a microwave sensor capable of overcoming these difficulties. There are many types of displacement sensors available today, and some of these are much better suited to precision measurements required by this application. However, none of these is robust to the hostility of a turbine environment. This microwave sensor is one potential candidate to enable turbine monitoring. This research is designed to delve into one difficulty the microwave sensor faces in turbine measurement, spatial filtering. The completion of the research is one step closer to an intelligent machine capable of monitoring and optimizing itself autonomously.

The problem that this thesis focuses on is that of spatial filtering. A microwave sensor of this type sends out a beam of microwaves that reflect off of a target and return to the sensor. The returned signal is related to the transmitted signal to determine how far the reflected waves have traveled—the displacement. The beam transmitted by the sensor does not converge to a point at the surface of the target; rather, some portion of the beam spreads out in all directions. This spreading is the root cause of spatial filtering. The measurement beam covers some area of the target, and energy is reflected everywhere that it encounters the target. All of these reflections are at various distances from the sensor, and they all average together in the final measurement. This averaging—or filtering—is spatial filtering, and it serves to distort or blur all measurements taken by the microwave sensor. Since the measurements are so precise and of small targets (the blades of a turbine) relative to the size of the beam, spatial filtering has a significant effect. The main task of this research is to analyze this effect, study the factors that change it significantly, and quantify the problem.

Both experimentation and theoretical modeling are used here to understand the effect of spatial filtering in microwave measurements of turbine blades. Experiments seek to analyze sensor data for major trends showing the influence of spatial filtering, while a computational model develops the theoretical base of understanding. Ideally, the model exactly represents reality. However, the differences between the model and reality are helpful for determining where the current theoretical understanding breaks down.

This thesis begins with an in-depth background study of turbine operation and measurement—especially tip-clearance and vibration monitoring. The difficulties faced in measurement are discussed and a review of other sensors proposed for use in this application is presented. An introduction to radars, and specifically this microwave sensor, provides the basis for a detailed discussion of the phenomenon of spatial filtering in measurement with this sensor and others. The experimental setup is discussed next. This is followed by background and a description of the computational model that simulates the experimental setup. Next, the experiments that were conducted are presented and discussed. The model is subjected to the same set of experiments, and these results are presented and compared to physical experimentation. The results of experimentation and modeling provide evidence that spatial filtering indeed has a significant influence on sensor measurements. This influence is analyzed and discussed for both actual experiments and computational modeling. This understanding lays the foundation for further analysis of the influence of spatial filtering on turbine blade measurements.

CHAPTER 2 MOTIVATION AND TURBINE MEASUREMENT BACKGROUND

Thesis Motivation

This research is one part of a large movement in turbine technology development directed toward more efficient and powerful turbine systems enabled by performance monitoring. In the modern world, turbines are crucial to the fields of power generation, transportation, and other heavy industry. The prevalence of turbines in today's energy and transport markets makes technological advances that promise to increase efficiency and effectiveness appealing. Measurement in these environments is challenging because they are among the hottest and fastest mechanical systems in the world. However, such measurements are critical to further turbine technology. Specifically, this research is aimed at furthering the development of a turbine blade tip measurement system. The driving forces behind blade tip measurement are mainly 1) increased emphasis on prognostics and health monitoring (PHM) and 2) a desire to increase fuel efficiency of the turbine system by fine tuning blade tip clearance. A more in-depth view of these two goals of sensor development illustrates why in-process turbine blade tip measurement is critical.

Prognostics and Health Monitoring

Prognostics and health monitoring are two concepts that are important in machine evaluation and maintenance. The term prognostics refers to evaluation and prediction of remaining lifetime of a system and its parts based on the measured parts of system wear. Effective use of system health monitoring can greatly enhance on-going engine maintenance by providing additional specific feedback to the maintenance and overhaul

routines. The alternative to advanced prognostics and health monitoring is a conservative maintenance schedule of changing parts based on time-in-service rather than actual condition.

Military aviation is now beginning to investigate condition-based technologies to reduce costs of operation for its large engine inventory. The 2002 DARPA/DSO Prognosis Bidder's Conference is an example of this call for advanced PHM from the military. At this conference, Leo Christodoulou praises prognosis for its potential to enhance present and future battle-readiness. Prediction of failure is necessary for safety, maintenance, asset usage, and mission success. He points out that the development of effective prognostics would change the mindset from "fear-of-failure" to one of "risk management". Establishing this level of prognostics also brings the statistical prediction of reliability down to the individual asset (a single engine or component) rather than that of a type of assets (a fleet of engines or type of component). This offers significant savings of money and time (Christodoulou, 2002). Andrew Hess continues the conference, saying that increased prognostic abilities are a major element in elevated effectiveness for advanced military weapons platforms such as the Joint Strike Fighter. The goal is improved reliability, safety, and maintenance efficiency with reduced cost. However, Hess notes that advanced sensors must be developed to detect flaws reliably in their early stages to manage maintenance costs. Specifically, several engine monitoring sensors were identified: eddy current probes, electro-static exhaust debris sensors, electro-static wear detectors, and microwave probes; all of these are non-traditional detection technologies useful for engine monitoring applications. He cites the

development of sensing devices as the second step behind problem identification in the strategy for improved prognostics (Hess, 2002).

In turbine health monitoring, a primary metric is blade tip measurement for the purpose of vibration detection. Some level of vibration is normal—turbine components are built to handle this environment; however, these vibrations put components in a constant state of oscillating stress, and this stress may eventually cause failure. It is important to note that a change in the vibration levels may indicate a change in the system stemming from some elevated level of damage. Computer models show that structural damage in turbine blades causes a change in the resonance characteristics of the blades (Tappert, 2001). By monitoring blade vibrations, it is possible to detect these degradations before they become significant causes of inefficiency or system failure. In the future, it is hopeful that this monitoring will greatly aid maintenance personnel in the upkeep of turbine systems. With the proper technology and understanding of turbines, maintenance personnel will detect problems early and even diagnose the causes of those problems. Blade vibration is monitored primarily by detecting changes in the time-of-arrival (TOA) of blades in turbines. Normally, these blades should be evenly spaced, but in reality, vibrations cause slight changes in these time of arrival measurements that are recorded by blade monitoring sensors. Bill Hardman, also at the DARPA/DSO Prognosis Bidder's Conference, provides an example of successful implementation of vibration sensing to monitor crack propagation in a helical gear, and proposes testing for high-speed turbine measurements (Hardman, 2002).

Turbine component wear is another metric for turbine prognostics and health monitoring. Wear, in this sense, refers to the surface deterioration of turbine

components. There are a few major causes of wear in turbines. First, the mechanical interaction of turbine components causes wear. For example, blades rubbing against the turbine casing can carve swaths out of the casing while destroying the tips of the blades. The friction caused by mechanical interaction can also degrade components, destroying protective coatings and surface finishes important to machine integrity. Next, extreme temperatures—especially those found in the combustion gas path—can eventually oxidize and erode the surfaces of blades and other exposed components, causing loss of structural soundness over time and, ultimately, failure. These elevated temperatures may also exacerbate problems caused by other sources of stress (Bhaumik et al, 2001 and Salam et al, 2001).

Additionally, some extent of turbine wear is directly detected by monitoring tip clearance changes over time. If blades rub against the casing, it is likely that many of the blades in the turbine disk will suffer some loss of material. These blades will be shortened, and the tip clearances will increase. Gallardo et al note the failure of the first stage of a gas turbine used in a chemical plant well before its designed length of service due to uneven clearance between blade tips and casing. Wear caused by interaction between blades and casing ended with premature failure (Gallardo et al, 2001); this type of scenario could be avoided given the proper sensor technology to detect this wear.

Turbine blades also may elongate over their lifetime due to material creep caused by the constant stresses of operation. This creep may occur gradually or in distinct creep events. Monitoring tip clearances over the life of an engine may aid in detecting creep. Another cause of blade elongation is the presence of cracks. These cracks may occur in either the blades themselves or the disks which they are held by. Cracks mostly start as

very small microcracks and grow through engine operation until they are large enough to seriously impact mechanical behavior or even cause failure. Using a combination of clearance and vibration monitoring, serious cracks may be found and the components replaced before failure.

Turbine literature is replete with the expressed need for advances in turbine PHM. However, in the "hot" section of turbines where temperatures can reach 1300° C and speeds are commonly up to 30,000 rpm, the limiting factor in prognostics is sensor technology, which must be capable of operation in this environment. Cotgrove and Wood lay out the current status of gas turbine monitoring as well as the usefulness of data toward increasing life and safety of turbines in the future. They note that more sensor development is needed in order to meet the demands for high-precision, high-quality data from harsh environments. Advanced sensing technology is designed to predict failure, monitor and compensate for deterioration, and further the understanding of turbine technology. Currently, when data is needed from these harsh environments, it is generally supplied by simulations that predict the current state based on a set of previous test data; real-time data could greatly improve this form of diagnostics and control. Cotgrove and Wood report that maintenance on the parts in the hot section accounts for 40-60% of the total maintenance costs for engines, though there are relatively few components in comparison with the whole system. Advanced monitoring techniques hold great potential for reducing these costs (Cotgrove and Wood, 1996).

Increasing Turbine Efficiency Through Active Tip Clearance Control

Turbines transfer energy from air into mechanical motion or vice versa. The efficiency of a turbine, therefore, has to do with the successful achievement of this

transfer of energy. In the achievement of this goal, the clearance between the tips of the blades and the turbine casing is an important factor for two reasons: (1) clearance between the blades and casing allows unwanted bypass air, which travels around the tips of the blades without contributing to the energy transfer, and (2) large tip clearances disrupt ideal airflow resulting in degraded energy transfer and higher temperatures. Overall, the efficiency of each turbine stage decreases by approximately 1-2% with an increase in tip clearance equal to 1% of the overall blade length (Walsh, 2004). This is significant considering the fact that many turbines in commercial jet aircraft or power plants run essentially non-stop and are relatively expensive to operate.

You et al studied another application of turbines in which the fluid flow is liquid. They showed that tip clearances are closely related to cavitation, where the liquid boils due to pressure differentials and friction; cavitation is a major cause of high stresses, noise, and inefficiency in fluid turbines (You, 2003).

Since new sensor technology promises the ability to monitor blade tip clearances accurately in the near future, clearance losses are a topic of much interest. Bannister and Cheruvu provide an overview of the Advanced Turbine System (ATS) program, which is designed to increase the efficiency and applicability of Westinghouse turbine systems. They note that tip clearance losses are a significant area for future improvement. Currently, the clearance in operational turbines is much greater than is desirable, and an active clearance control system would reduce the flow past the tips by as much as half (Bannister and Cheruvu, 1994).

Even early in turbine development, developers suggested that controlling tip clearance in turbines could potentially increase efficiency, but only recently have

advances in sensor technology enabled this possibility. Mattern et al describe the development and testing of an active clearance control system used in a centrifugal test rig. They note that active control systems must be designed to account for all transient behaviors of a turbine such as loading, whirl, wear, and others—all of which could be monitored by adequate sensor technology. For clearance control, their system uses an improvement of the electromagnetic actuator implemented earlier by Weimer. For measurement, Mattern et al use a capacitive sensor with approximately 0.01 mm (0.0005 in.) resolution. Testing shows that the system can be implemented effectively, and that the sensor is the limiting factor rather than the control system. They report an increase in efficiency of approximately 0.5% with a 0.1 mm (0.005 in.) decrease in tip clearance; they also report a 60% reduction in vibration, which was noticeable audibly to the turbine operators (Mattern et al, 1997).

Sensor Development Challenges

Though the need for active measurement of turbine blades is present, these measurements are difficult to make because of the nature of turbine systems. Turbines are among the most advanced machines in the world, and the environment within a turbine is extremely harsh. Sensors that can both survive the environment while making adequate measurements are needed. Environmental concerns, required precision, and speed are the top three challenges that face sensor development for turbine prognostics and clearance monitoring. Each of these is discussed in further detail following.

Environmental Concerns

The environment in a turbine is not friendly to sensors; it is harsh—particularly in the hot section. Measurement probes in turbines must be capable of withstanding a wide range of temperatures and vibrations. Many turbines operate on aircraft that commonly travel at altitudes where the air temperature is well below 0° C (32° F); however, the gas inside the turbine's combustion chamber, even at these altitudes, can reach above 1300° C (2000° F). Situations like these create large temperature extremes that normal sensors cannot tolerate. At the same time, turbine sensors must operate under high vibration for extended periods of time. Mechanical durability and measurement sensitivity to vibration is also important. Lastly, in a turbine's hot section, sensor measurements must be unaffected by combustion products. Many optical sensors, for example, are effective in the cleaner sections of turbines, but cannot maintain performance quality in the presence of combustion products for long periods of operation.

High-precision measurements

Another major challenge to blade tip sensor technology is the high-precision required by the applications of this data. Turbine tip clearances are typically on the order of 0% to 4% of the total blade height (Chivers, 1989), ranging up to 3 mm (0.1 in.) in most turbine engines. In order to control these clearances effectively, the measurements must be significantly better than this—on the order of tens of micrometers (less than 0.001 in.). Smaller turbines may require even better sensing capabilities because of scaling. Time-of-arrival measurements are no less demanding; vibrations in blades are small, and measuring them requires great precision. These vibrations can range up to

about 0.01°, which corresponds to a tangential motion of 0.75 mm (0.030 in.) for a 50 cm (20 in.) turbine disk. In order to accurately detect these small motions, the tangential resolution of sensors must meet these requirements.

High-speed measurements and processing

A final challenge of turbine blade monitoring sensors is the high speed required to collect and process data. Typical military aviation turbines operate at speeds up to and exceeding 18,000 rpm. Considering a 51 cm (20 inch), 64-blade disk spinning at this speed, a blade passes every 52 microseconds, and many data points must be taken over each blade for proper analysis. A data acquisition rate of at least 5 MHz is required. This data may be logged for future processing, or it may be used for real-time monitoring applications. Either way, the data must be logged or processed fast enough to keep up with the data acquisition rate. Computational advances now are beginning to make this practical. But at this point, it is still non-trivial. Tappert et al begin to address the challenge of using computers to actively and autonomously monitor the state of turbines in-situ. The extremely large amount of data requires efficient processing and algorithms designed to maximize the information obtained from data while discarding extraneous information. Tappert et al suggest algorithms designed to recognize the theoretical danger flags in data trends and keep track of the progress of the turbine performance. They present ideas for FOD detection, cumulative fatigue, crack growth, and disk integrity monitoring through blade vibration as well as tip clearance control (Tappert, 2001).

Other Sensors used for this application

Many types of sensors have been implemented in attempts to measure turbine blades during operation. The following is a brief review of sensors used for this and other similar applications in the past. Electromechanical, capacitive, eddy current, optical, and pneumatic probes are each presented here. However, microwave sensors used for turbine applications are omitted in this section since the next chapter is specifically concerned with microwave sensing.

Electromechanical probes

Electromechanical devices couple mechanical action and electrical sensing to make measurements. Davidson et al developed one of the first electromechanical sensors using an electrode to detect clearance between the stationary stator vanes and the rotating drum. The drum is first coated with an electrically conductive paint and grounded, and the electrode is lowered mechanically by means of a precision stepper motor until an electrical charge arcs across the gap to the rotating drum. The distance between the electrode and blade tip is calculated based on the voltage of the charge; a clearance measurement is calculated by adding the distance that the electrode is lowered into the turbine. The electrode is a tungsten wire fed through a Teflon-filled hole drilled in a stator vane into the turbine. A microcontroller detects the flow of a charge, and moves the electrode in and out in response. The response speed of the system is limited to less than 10 samples per second, and the resolution of the system is limited by the resolution of the stepper motor motions and the pitch of the lead screw driving the electrode into the turbine (Davidson et al, 1983).

Sheard and Turner developed a second generation model of Davidson et al's electromechanical blade tip measurement system and demonstrated its durability up to 1500 °C under the normal vibrating conditions of a running engine. Their sensor is approximately 20% the size of Davidson et al's, which is too large for practical use. This version measures passing blades rather than a rotating drum, and operates by driving an electrode down from the casing toward the blades with a stepper motor until it is close enough to the passing blade tips (within 3 to 5 μm—about 0.0002 in.) for an electrical charge to arc. They report an accuracy of 25 μm (0.0010 in.) over a 6 mm (0.2 in.) range; however, the sensor is only used to measure the clearance between the casing and the longest blade since it cannot extend farther towards the other blades without being hit by the longest blade. Sheard and Turner report three laboratory tests with increasing environmental hostility (temperature and vibrations). The probe operated successfully in all three (Sheard, 1992).

A third generation model of the Stepper Motor Driven Probe uses the same design concept to measure the longest blade with a mechanical probe that sparks when it comes close enough to the blade, but adds a frequency modulated capacitance probe (FMCP), developed by Chivers and discussed in the next section, to measure the difference in length between the longest blade and the other blades. The FMCP is attached to the mechanical probe and samples at speeds up to 30 kHz. The accuracy and durability of this probe are similar to the second generation probe; however, since all of the blades are measured, rotordynamics like eccentricity are detectable. Sheard notes a 50 μm (0.002 in.) eccentricity of the bladed disk (Sheard, 1994).

Capacitance Probes

Capacitance sensors make measurements based on the electrical capacitance created by the gap between a blade of the turbine rotor and an electrode installed in the turbine casing. The turbine blades and disk must be electrically conductive or coated with some conductive material in order for this method to be feasible. These turbine blades are then grounded and capacitance is measured from the electrode in the casing. The capacitance is related to the distance between the blade and electrode as well as the common shared electrical area; see Equation (1).

$$C = \frac{\varepsilon \cdot S}{d} \tag{1}$$

In this equation, ε is the dielectric constant of the material in between the blade and casing (gas/air mixture, which is very nearly the same as air), S is the common area, and d is the clearance between the blade tip and the electrode (Bailleul, 1996).

The capacitance between the tip of the blade and the electrode in the casing is very small due to the small area of typical compressor blade tips and the relatively large clearances. This makes measurement very difficult by conventional means. In turbine applications, this capacitance is about 0.02 pF (Müller, 1996). To overcome this difficulty, Chivers developed a method of measuring capacitance indirectly by tying the capacitance level to a frequency modulated oscillator. Thus, a change in capacitance drives a change in the frequency of the oscillator, which is processed by a demodulator and measured at high resolution. This measurement is then used to calculate a change in clearance by direct comparison to a calibration curve (Chivers, 1989). Because of the

significant decrease in capacitance with increased clearance, the combination of the electromechanical probe for coarse measurement and FMCP for fine measurements documented above is appealing.

In conjunction with Sheard, Müller et al developed a static FMCP to measure tip clearance to within 60 μm (0.003 in.) over a range of 203 μm (0.00799 in.), increasing the ease of use and practicality of the sensor. In this sensor, the capacitance probe is rigidly mounted flush with the turbine casing or recessed into the casing. The capacitance and distance are still related by a calibration curve. In engine tests, the probe performed well in the high pressure compressor stage, but in the high pressure turbine stage, environmental effects—especially temperature—were too great on the electrical properties of the probe and measurements were invalid (Müller et al, 1996).

Bailleul and Albijat report on the progress toward the development of capacitive sensors for use in turbines in both the hot and cold sections and designed a sensor in hopes of building upon this base. They suggest a lifetime for turbine sensors of 20,000 hours of operation in commercial turbines. The sensor developed by Bailleul and Albijat only survives temperatures up to the goal of 1300 °C for a short time period. Hence, it is not presently a reasonable choice for an active clearance control turbine (Bailleul and Albijat, 1996).

More recently, Drumm and Haase present another advance in capacitive sensor capability in measuring turbine blades by greatly increasing the spatial resolution of the sensor. They accomplish this by changing the geometry of the measurement situation, making better use of the electrostatic field around the sensor to better suit interaction with

blade passages; also, a number of sensors stacked together are used to increase lateral resolution of time-of-arrival measurements.

Fabian et al developed a tip clearance sensor designed for active clearance control of a palmtop micro gas turbine. Since micro gas turbines spin at much greater speeds than normal turbines (optimal operating condition for the turbine in question is 800,000 rpm), it is not feasible to measure tip clearances blade by blade. Thus, a capacitance probe was developed to use all of the blades as one electrode, and the entire casing of the turbine as the other. The capacitance between the two provides the average tip clearance for the whole turbine through a calibration curve. Fabian et al report excellent results of clearances within 1 μm (0.00005 in.) in a test situation (Fabian et al, 2002).

Eddy Current Probes

As early as 1982, Rickman reports the use of a commercially available eddy current sensor to measure blade speed through the casing of a diesel engine's turbocharger for the sake of fault detection. There are two types of eddy current probes—active and passive. An active eddy current probe actually induces eddy currents in a target, whereas an active probe allows target motion to induce eddy currents through a static magnetic field. The disturbance caused by these eddy currents is measured in a conductive coil; when a blade passes, there is a peak in the voltage in the coil. Rickman notes that the geometry of the measurement situation is important to the calculation of the disturbance in the magnetic field; however, any attempt to quantify this is neglected since the goal is to measure speed. The voltages are calibrated for each sensor, and electronics track the speed of blades (Rickman, 1982).

One advantage of an eddy current sensor is that it is possible to develop a sensor that operates without altering the engine casing at all. Roeseler et al describe an eddy current sensor developed and tested through various shims simulating a turbine's casing in order to establish the feasibility of blade sensing through a turbine's casing without drilling holes. They note that titanium and stainless steel do not affect the sensors significantly while aluminum reduces the signal by approximately half. They also propose an eddy current probe that withstands temperatures of 500 °C (1000 °F), which may be sufficient for turbine use since the temperatures at the outside of the casing are significantly below the gas temperatures inside the casing (Roeseler et al, 2002).

Optical Probes

Optical measurements of turbine blades are appealing because of the high speed of response and the resolution of measurements. The limiting factor concerning speed is the processing speed of the sensor. Jones and Hazell present an optical method of measuring blade vibration using optical fibers to measure reflections of a laser off of blades. The sensor is designed to detect the reflection of a laser off the tips of the blade in order to determine blade-by-blade time-of-arrival for use in vibration monitoring. The system is limited in resolution due to scattering of light off blades causing reduced power to be received back by the sensor (Jones and Hazell, 1992).

Kawasima reports on a method of measuring vibrations in turbines using an optical system built on a semiconductor; this system also simply uses lasers to obtain time-of-arrival measurements in order to determine blade vibrations. The system's advantage lies in its simplicity and compactness, and it represents significant signal

processing advances and speed gains over previous reported optical methods in literature (Kawasima, 1994).

Dhadwal et al presents a method of tip clearance measurement using two integrated fiber optic laser probes (IFOLPs) to detect the apparent width of a passing blade. They note that the blade width changes linearly as the clearance increases due to the increased width of the laser spot relative to the size of the blade. Rather than attempting to measure clearance directly using lasers, apparent width of the blade tip correlates to the actual clearance. The two IFOLPs are angled so that one reflects off an incoming blade and the other off the outbound blade; the time interval between these measurements is used as the apparent blade width, which is correlated with blade clearance. The probe was tested on a NASA spin rig and was found to be accurate to within 13 μm (0.00051 in.) over a range of 2 mm (0.08 in.). However, this probe is suited only for the relatively safe environmental conditions of the compressor section of a turbine engine; any type of combustion materials or debris in the turbine section, along with the elevated temperatures decrease the effectiveness and survivability of the probe (Dhadwal et al, 1998).

Pneumatic Probes

Belsterling suggests the use of air (pressure and flow) as a non-contact method of measuring displacement and orientation. Many different types of sensors are recommended that measure how fluid flow is disrupted or interrupted by the passage of objects. One such example that might be applied to turbine blade passage is a sensor having an input and output port for pressurized air; in between the input and output is a

hole for flow into the inside of the turbine. A blade passage partially blocks the flow into the turbine, and this is detected at the output of the sensor (Belsterling, 1971).

CHAPTER 3 MICROWAVE SENSOR INTRODUCTION

The sensor used in this thesis is essentially a short-range radar system, but it is different than other microwave systems previously used for blade tip measurement. Previous systems measure changes in a microwave resonant cavity, but this system is phase-based like most modern radar systems. Below is an introduction to radar systems and their applications. Following is a brief review of other short-range radar systems; finally, the current measurement system is described in detail.

Radar background

Radar is an acronym standing for **RA**dio **D**etection **A**nd **R**anging. First implemented by Hülsmeyer of Germany in the early 1900's, it was advanced greatly during World War II. From this point, radar quickly rose to its position as the unchallenged leader in long-range detection. The basic concept of a radar system is the transmission, reception, and analysis of electromagnetic waves reflected off of some target. Conventional long-range radar systems transmit pulses of radar waves and measure the time-of-flight (TOF) between transmission and reception of these waves. TOF for a target, *T*, depends directly on the distance traveled according to Equation (2).

$$\mathrm{TOF}_T = \frac{2 \cdot d}{c_{\mathrm{air}}} \tag{2}$$

c_{air} is the speed of electromagnetic waves (the speed of light) through air, and d is the distance to T—this value is doubled since radar waves must travel to T and back to the

receiver. Rearranging this equation gives the distance to a target with a known TOF. The detection of a target at some distance depends on the ability of the radar system to detect and recognize the reflected energy from the target; this is generally a function of the amount of energy reflected back to the radar. The equation governing this is one form of the Fundamental Radar Equation:

$$P_r = \frac{P_t G^2 \lambda^2 \sigma}{(4\pi)^3 d^4}. \tag{3}$$

where

P_r = power received back at radar
P_t = power transmitted
G = antenna gain
λ = wavelength
σ = radar cross – section of target

Originally, radar was simply used for detection of objects, but with the increasing advancement of signal processing capabilities along with the entrance of the Electronics and Computer Age, the quality and usefulness of radar gained momentum until detection, ranging, precise locating, and even identifying with radar have become possible. For a more detailed treatment on the history, development, and theory of radar systems see (Skolnik, 1962 and Sullivan, 2000).

Types of radar Systems and applications

Broadly, radar systems may be divided into three categories: continuous wave (CW) radar, pulse radar, and passive radar. CW radars transmit a continuous sinusoidal

signal and measure modulation or interference of that signal as it is returned; generally, the constructive or destructive interference between the original outgoing signal and the received signal is of highest interest. CW radar systems can be further divided into frequency modulated continuous wave (FMCW) radar and plain CW radar. Pulse radars transmit a pulse or series of pulses and measure TOF and modulation of returned reflections; this is the most common and most well-developed type of radar. Passive radars do not transmit any signal; they measure background radar waves from other sources and glean information from them.

Radar systems can also be differentiated based on the frequency of electromagnetic waves used. Initially, radars were developed using traditional radio frequencies (e.g. 500 MHz) but have mostly moved to higher microwave frequencies for better performance. Higher frequencies give better resolution because the wavelength is small relative to most targets; electromagnetic interaction is more consistent when this is the case. Also, higher frequencies have better electromagnetic propagation characteristics.

In the past, radars have been used for nearly every detection application imaginable. Most commonly, they are used for long range detection of targets through the open atmosphere and space. This includes the location and limited identification of land vehicles, ships, aircraft, and spacecraft, as well as natural atmospheric and terrestrial objects. Air-traffic-control is one familiar civilian application, and a common military application is the detection and tracking of hostile targets. Meteorology is another application that is widely known.

The application of radar for the purposes of this research is conventional CW radar at microwave frequencies. However, this system is unconventional in that it is a short-range radar system, measuring targets much less than 3 mm (1 in.) from the antenna aperture. The ability of a system to work in such conditions depends greatly on its antenna, a subject discussed in the next section.

Antennas and Fields

Antennas come in many shapes and sizes and work in many different ways. In general, however, antennas all perform the same function of propagating electromagnetic waves away from a radar system and/or collecting waves and sending them to a processing unit as electrical signals. Some antennas only transmit; some only receive, but many do both. Antennas can be shaped as wires, horns, loops, rods, tubes, patches, dishes, panels, etc and can be implemented singly, in groups, or in arrays.

There are a few concepts that direct the use of antennas. One of these is the concept of a power output and reception pattern. Antennas do not propagate electromagnetic waves perfectly evenly in all directions. All have some pattern that describes the power output and reception in every direction; each direction releases or receives a certain amount of the total power of the system. Also, electromagnetic waves themselves are directional, or polarized and this contributes to the shape of the antenna pattern. Some antennas are intended to be directional, sending out more power in certain directions than otherwise; others are non-directional, propagating evenly in all directions. A function describing this pattern is often called a point-spread function (PSF).

Other important concepts of antennas are the band and bandwidth of the antenna. Each antenna is designed to propagate certain frequencies of radar waves, this is referred

to as the band of the antenna. The range of frequencies for which the antenna is useful is the bandwidth. Radar waves outside the band of the antenna do not efficiently cross the aperture of the antenna to either escape into the atmosphere or be received by the system.

The region of propagation of electromagnetic waves around an antenna is divided up into fields that have different characteristics. Each antenna has a far-field and a near-field. The far-field is the region in which wave propagation is fairly consistent and wave-lines become approximately straight lines. By convention, the far-field is considered to be the at a distance of

$$d_{\text{far-field}} > \frac{2D^2}{\lambda} \tag{4}$$

where D is the length of the aperture of the antenna. The near-field is subdivided into the radiating near-field and the reactive near-field. The radiating near-field is characterized by mostly normal antenna propagation and complex interactions between waves due to the difference in direction and distance of different points of the antenna and target. The reactive near-field is the least understood field due to the fact that it is rarely a region of normal operation; in the reactive near-field, interaction between the antenna and target actually changes the propagation characteristics of the antenna itself. This field is commonly considered to be the region within

$$d_{\text{reactive near-field}} < \frac{\lambda}{2\pi}. \tag{5}$$

A microwave turbine blade sensor operates well within the reactive near-field, introducing difficulty and uncertainty into the theoretical basis of wave propagation and reflection at these distances.

For an in-depth analysis, the author suggests (Johnson, 1993) as a thorough reference for all issues related to antennas; however, even in this reference, the reactive near-field is only a topic of mention and not of exhaustive investigation.

Short range Radar sensors

Rarely and only recently has radar been a method used for short range detection and measurement. Operation in the reactive near-field is even less common. Nonetheless, a few such examples are mentioned below for note and comparison.

Giubbolini applies a microwave sensor to the detection of objects within a few meters of a vehicle. The sensor system uses multiple FMCW microwave transceivers in the 13.4 to 14 GHz range in conjunction with a triangulation algorithm to accurately locate obstacles to within 1 cm (0.4 in.) accuracy. The algorithm uses knowledge of the PSF of each antenna to compute the radial distance and echo intensity of each obstacle, and combines the information from multiple sensors to determine the exact location. The near-field of the antennas of this system is the region within about 0.5 m (20 in.), and the reactive near-field is the region within 5 cm (2 in.). This sensor does not operate nominally in the reactive near-field of the antennas (Giubbolini, 2000).

In 2001, Mazzucato recommended the use of microwave reflectometry for the measurement of plasma turbulence in nuclear experimentation. The presence of plasmas directly modulates a microwave field, and this modulation can be measured as a phase change in microwaves reflected off of the plasma. Although this had been considered for

use earlier, Mazzucato enhanced it by developing a method of spatially measuring this turbulence using an array of small microwave receivers. The end-result is an image of this fluctuation pattern in the experimental plasmas (Mazzucato, 2001).

As described above, in 1995, Holmes applied for and received a patent for the idea of using a miniaturized radar for the purpose of monitoring displacement in mechanical devices. A miniature radar built on a circuit board transmits and receives radar waves; a target modulates the signal, and this modulation is related to displacement (Holmes, 1998).

Soon after, in 1996, Grzybowski, et al reported on the development of a simple microwave sensor for measuring real-time turbine blade tip clearances to high accuracy in harsh environments. The sensor uses a dielectric-filled waveguide to set up a resonant cavity for microwaves. A passing blade tip forms another resonant cavity at a slightly differing frequency, and the difference of these frequencies is related to clearance; similarly to other tip gauges, a calibration curve is used to determine the actual distance. The probe is designed to operate well under harsh conditions and even with blade rub against the probe tip (Grzybowski et al, 1996).

Closest to the system used for this research, Wagner et al presented a method of microwave sensing in 1998. The system mixes a signal reflected off of turbine blades with a reference signal to obtain the phase difference between the two. It can be shown that by adjusting the outgoing frequency, this response peaks. This peak is used to measure time-of-arrival. Wagner's system uses a closed-loop control system to vary the frequency in order to obtain these peaks. Wagner et al mention that this system could perhaps be used to measure tip clearances, and they also postulate that the shape of the

received signal could give qualitative information about the condition of the blade being measured; however, they do not explore these possibilities (Wagner et al, 1998).

The Microwave system Used in This Research

A new sensor, developed and patented at The Georgia Institute of Technology (Geisheimer et al, 2002), represents a significant advance from the previously mentioned microwave blade-tip sensors. A comprehensive explanation of the workings of this sensor can be found in (Chuckpaiwong, 2003), but a brief description follows. Like Wagner et al, mentioned above, the sensor involves a radiating microwave source reflecting off of a target. The reflected microwaves are mixed with a reference signal to obtain two different channels (Inphase and Quadrature channels), which determine the phase difference between the reflected and reference signal. The major difference between this system and the system of Wagner et al is the addition of the second channel, which adds much more information. In short, it allows decoupling of the amount of reflected energy (dependent on radar cross-section) from phase change (dependent on distance to target). Practically, this means that with one channel it is not possible to differentiate between a change in reflective quality and a change in distance to the target, whereas two channels make this feasible.

The output of the microwave portion of the sensor may be represented by a vector, where the x-axis is referred to as the Inphase (I) channel and the y-axis is referred to as the Quadrature (Q) channel. The target vector, T, may then be divided into radial and phase components. The phase component is the phase difference, θ, between the reference and reflected signals; the radial component, referred to as radar cross-section (RCS), indicates the amount of reflected energy from the target. Figure 1 illustrates this.

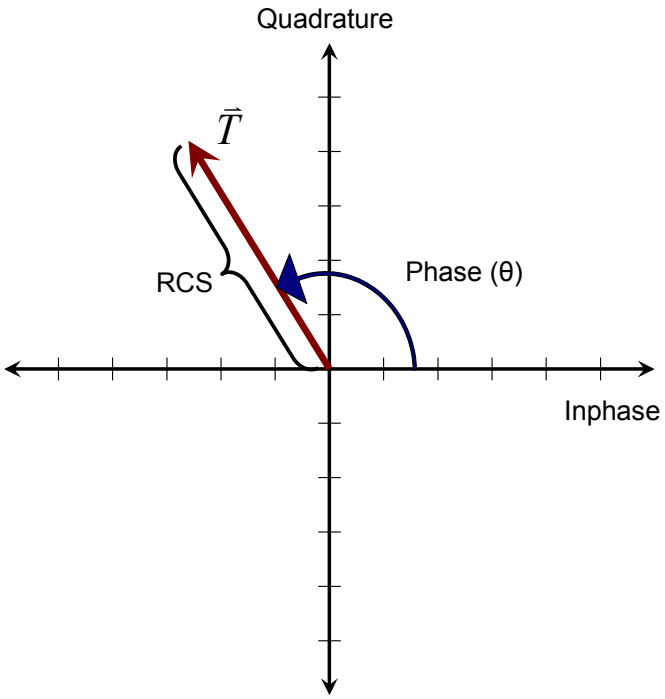

Figure 1. Inphase and Quadrature channels plotted in the complex plane; the vector, T, represents the relative phase and magnitude of the microwaves reflected back to the antenna from the target.

The phase of T is determined by the distance traveled by the reflected signal relative to the distance traveled by the reference signal at the point of mixing. The phase difference in radians between the reflected signal and the reference signal is calculated by Equation (6).

$$\theta_{\text{relative}} = \theta_0 + \text{mod}\left(\frac{2d_{\text{absolute}}}{\lambda_{\text{air}}}\right)\cdot 2\pi \tag{6}$$

d_{absolute} is the total distance traveled by the signal (twice the distance to the target), λ_{air} is the wavelength of the microwave source in air, and θ_0 is a constant internal system phase

difference unique to each individual sensor. This relative phase corresponds to a relative distance calculated in Equation (7).

$$d_{\text{relative}} = \frac{\lambda_{\text{air}}}{2\pi}\frac{\theta_{\text{relative}}}{2} \tag{7}$$

The absolute phase may only be determined if the number of full wavelengths traveled and the initial system phase lag, θ_0, are known. Then the absolute distance from the antenna to the target is calculated as follows:

$$d_{\text{absolute}} = \frac{\frac{\left(\theta_0 + \theta_{\text{relative}}\right)}{2\pi}\lambda_{\text{air}} + n\lambda_{\text{air}}}{2}. \tag{8}$$

As a target moves, a number of things happen resulting in the final measurement. First, as the target moves, the distance between the sensor and the target changes; this effects a change in the relative phase of the vector representing the target. Figure 2 depicts this.

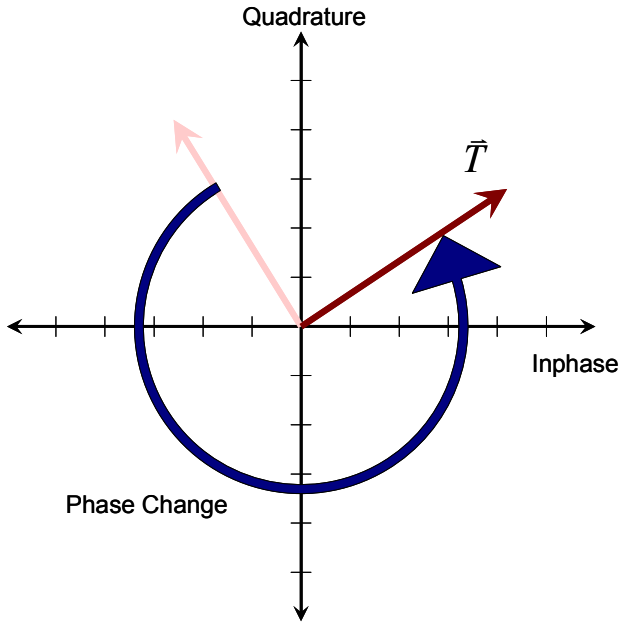

Figure 2. As the target moves, the phase of the vector, T, changes according to the amount moved and the wavelength of the microwaves.

Next, the amount of energy received back at the target is relative to the distance between the sensor and the target because of the attenuation of microwaves in air; so, as the target gets farther from the sensor, less energy is received, and RCS decreases; this causes the measurement to spiral in towards the center. Figure 3 shows this.

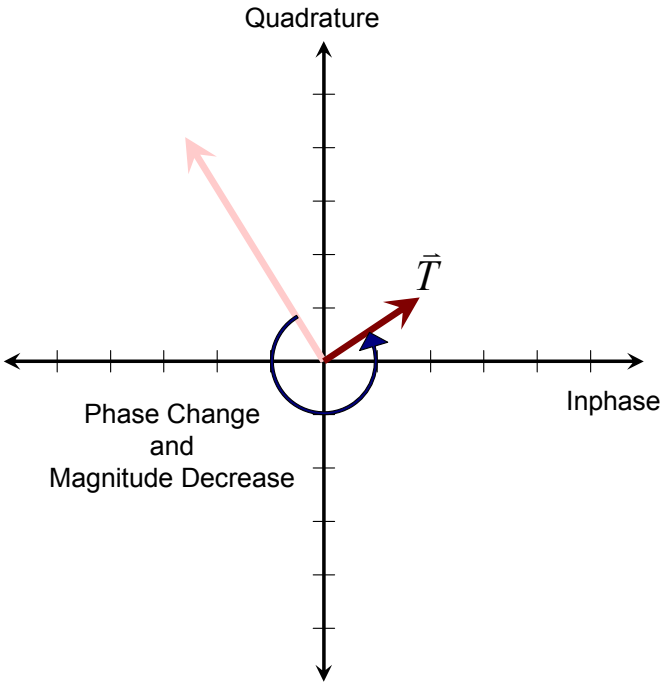

Figure 3. As the target moves away, the phase changes and the magnitude of the vector decreases.

Finally, as the target moves, the geometry of the measurement situation often changes and this can cause the amount of energy reflected back (RCS) to the sensor to change.

Additionally, all measurements include a DC component caused by reflections off of stationary elements in the measurement situation such as the antenna joints, internal antenna elements, and stationary external objects such as walls—or in the case of a turbine, the turbine casing and bladed disk. This DC component shifts all measurements within the complex plane. All motion appears to rotate around this DC component, termed the DC center. Figure 4 illustrates the DC component adding to the measurement in Figure 3.

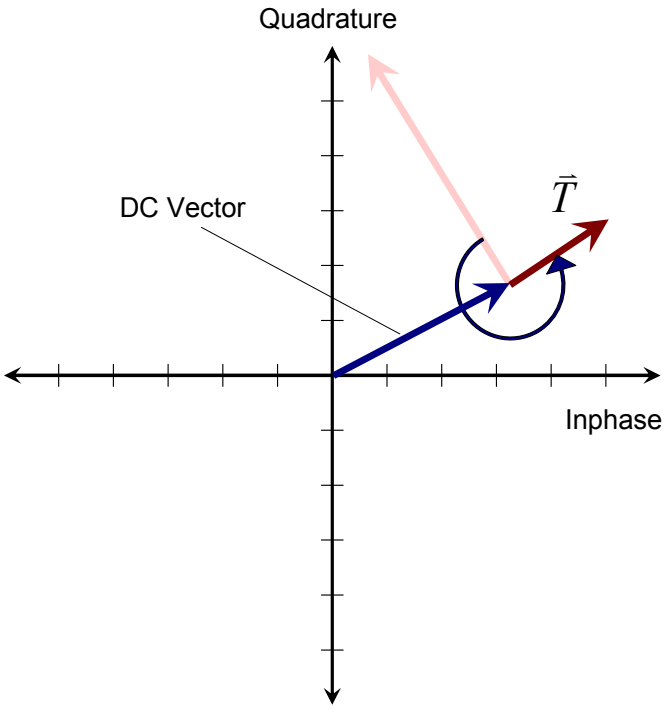

Figure 4. A constant DC vector made up of reflections from stationary objects and internal microwave reflections is the point around which the vector of a moving target rotates.

Since this sensor has two channels, Inphase and Quadrature, the phase is decoupled from the RCS of the measurement. This phase is used by the above calculation method to derive the distance between the sensor and target. This is the main distinction of this sensor from other microwave sensors described. This technique represents a significant improvement over other methods because of this decoupling of phase and RCS. Without this decoupling, any change in RCS cannot be distinguished from a change in phase, possibly resulting in measurement errors.

CHAPTER 4 SPATIAL FILTERING BACKGROUND

Introduction to Spatial Filtering

Spatial filtering is a term typically used in the context of image processing to describe the concept of modifying an image based on its spatial properties; it is the analog of traditional filtering in the field of signal processing. Common filters used in signal processing act on one dimensional input signals, but spatial filters are two and three dimensional. An example of this is a circular optical filter used to smooth the intensity profile of a laser. The laser intensity profile is two dimensional, and the intensity profile is smoothed in a similar manner to the way a low pass filter smoothes an electrical signal.

Spatial filtering takes another form in many dimensional measurement systems that often treat a measurement taken over an area as a single point measurement. An ideal dimensional point measurement is one taken with an infinitely thin probe tip in order that the point-of-contact would be infinitesimal; however, this is only theoretical and not practical. Realistically, all probes used in measurement have some finite size, introducing a level of uncertainty into the resulting measurements.

Spatial filtering occurs with mechanical probes since the exact probe-tip is not always the point-of-contact. Errors are introduced when measurements are taken anywhere but the exact tip. Figure 5 illustrates this loss of accuracy. In this example, the probe tip is a sphere, and the point-of-contact changes significantly as the probe moves across the surface. The resulting measurement is shown as the dotted line. Any convex angles in the surface are curved by the spherical probe, and the measurements along any

surfaces at an angle relative to the probe tip lose accuracy because the point-of-contact changes.

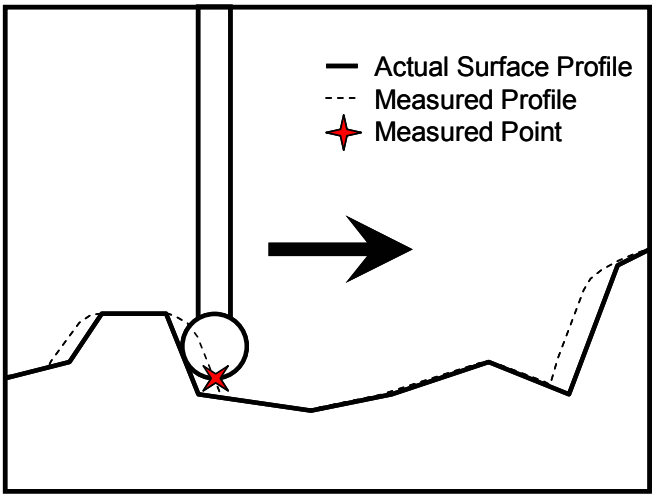

Figure 5. Illustration of spatial filtering with a mechanical measurement probe.

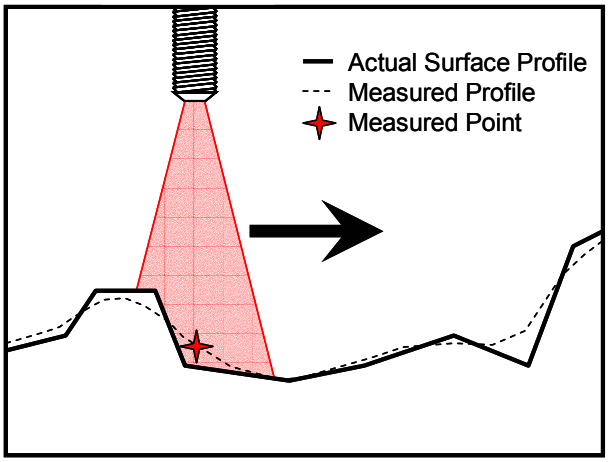

Figure 6. Illustration of spatial filtering with a non-contact measurement probe

Figure 6 illustrates the spatial filtering phenomenon for non-contact measurements. In non-contact measurements, the problem of spatial filtering is slightly different. Measurements are treated as though they were point measurements, but the

measurement is actually a weighted average of measurements over an area or volume, based upon the reflectivity of points within the beam. In the case of a measurement probe in the form of a beam (the laser light of an interferometer, electromagnetic field of an eddy current probe, or microwaves from a radar), the projection onto an object of interest does not converge to a single point. Instead, the area that the sensor detects is generally circular. Some portion of the waves at all of the locations across the area are reflected back towards the antenna; these reflected waves vectorally combine to form the final signal that is detected and used in measurement calculations. As a result, the final measurement is a weighted integration of the measurements over the surface within the field-of-view (FOV).

Spatial Filtering with A phase-based microwave Sensor

For a phase-based microwave sensor, this weighted integration is the sum of all the signals reflected back to the antenna from the surface of the target. All of the reflected signals are microwaves of approximately the same frequency of the transmitted signals, but they are different in two important ways: 1) the phase shift of each signal depends on the distance the particular wave travels, and 2) the amplitude of the signal (strength of reflection) determines its relative weight in the average of the aggregate.

Phase shift is easily determined since the wave travels twice the distance from the antenna to the object. At each point along a surface, this point-to-sensor distance is different. Even when measuring a perfectly flat plate, only the point directly along the central axis of the antenna is at the ideal distance from the sensor; all other points are slightly farther from the antenna, and the addition of all of these reflected waves shifts the phase of the aggregate farther away than this ideal point measurement. With an uneven

surface, the phase shifts of all of the points combine into a single phase shift that is somewhere in the middle.

The amplitude of the reflected signal is a great deal more complicated since it depends on more variables than just the distance to the target. A reflected wave's amplitude is the measurement of the power received back at the antenna; it is a function of attenuation, angle of incidence, material and surface qualities, and angle off of the central axis.

Attenuation is the amount of power dissipation as the wave travels through space. With microwaves, just as with light waves, attenuation is a function of distance. The radar equation, Equation (3) above, contains this relation. It is rearranged here for convenience.

$$P_r = \left(\frac{P_t G^2 \lambda^2 \sigma}{(4\pi)^3} \right) \frac{1}{d^4}, \tag{9}$$

In this equation, *d* is the distance from the antenna to the measured point on the surface. This value is also dependent on other factors such as the atmospheric conditions through which the wave travels.

The angle of the surface relative to the line of travel is also a factor affecting the reflection amplitude, since little electromagnetic energy is reflected back to the antenna off a surface that is angled away from the sensor—most energy reflects into space in another direction. The amount of energy reflected back at the sensor is a combination of specular and diffuse reflections. These phenomena are discussed in more detail in Chapter 6. Next, microwaves interact with different materials in different ways, much

like light. Just as light can pass through transparent materials, some materials are transparent to microwave sources, such as dielectrics that are used to make antennas. Metals are usually very reflective and suitable for measurement with a microwave sensor. The reflection also depends the surface quality of the material. Rough surfaces cause scattering of the electromagnetic waves while smooth finishes reflect energy with less scattering. Hence, when viewed at an angle, a rough surface causes more energy to be scattered back towards the antenna, while a smooth surface reflects almost nothing back.

Finally, the amplitude of the reflected signal is affected by the angle off the central axis of the antenna. This is caused by the non-uniform antenna pattern of the sensor. The antenna pattern relates the angle off the central axis to the amount of energy released in that direction. Since the amount of energy transmitted straight away from the sensor is generally greater than that which is transmitted off at an angle, the reflections from the center of the FOV have more effect on the overall measurement. For most microwave applications, the antenna pattern is a fairly complicated sinc function caused by the constructive and destructive interference of the waves and the internal reflective properties of the antenna. However, for this application where the antenna is operating in the near-field, the small antenna aperture widens the beam and reduces the side lobes.

Individual distance measurements taken by a short-range microwave sensor nominally depend only on the phase change between the internal reference signal and the reflected signal; thus, it is decoupled from the amplitude of the waves, which makes calculations simpler. However, when spatial filtering is considered, the amplitude of the signal becomes important because of the combination of measurements over an area.

Sensors with Spatial Filtering

Various sensors experience spatial filtering in different ways. Typically, calibration is used to compensate for the errors introduced by spatial filtering. The following is a brief review of sensors with spatial filtering issues and the methods used to overcome the errors introduced.

Touch probes

As described previously, errors from spatial filtering show up in touch probes when measurements are taken at points other than at the very tip of the probe. The most common method of compensation for errors introduced into mechanical touch probe measurements is an error map of the probe tip. The direction of contact is associated with some certain error based on the particular probe tip being used. To counter the difficulty of measuring geometrically complex objects with commercial CMMs, many have articulating probe tips so that measurements can be made from the same point on the probe tip; however this may make error compensation more complex because of the positioning of the probe. Pahk et al describe one such technique of real-time compensation using a systematic calibration procedure along with separate machine and probe-tip coordinate systems (Pahk et al, 1996).

Pretravel refers to a method of enhancing compensation for spatial filtering errors using the forces measured at the base of the stylus to more precisely calculate the direction from which the probe first touched the target. Using this information along with the knowledge of the probe tip geometry, errors in the measurement can be

mitigated. One method of calculation of pretravel is described by Shen and Springer (Shen and Springer, 1998).

Ultrasound Probes

Spatial filtering in ultrasound measurements is similar to that of other non-contact methods; ultrasound propagation from the source does not converge on a single point; thus, the measurement taken is the convolution of the point spread function (the function describing the intensity of propagation of sound waves from the sensor) with the shape of the object being measured. The literature contains three main methods of countering the spatial filtering problem in ultrasound measurements.

The first method is by differentiating measurements by the time-of-arrival of measurements back at the sensor. Mehrdadi et al developed a method for removing the influence of unwanted reflections by generating a somewhat random burst signal, which is directed at different angles from the sensor; these signals are recombined and analyzed by a cross correlator, which is designed to remove unwanted signals. Signals of different reflections are differentiated by the TOA back at the receiver, and the cross correlator picks out the signal with sufficient reflection power to be denoted as a direct reflection from the point being measured. By pointing the beam in different directions, irregular surfaces can be measured since there is almost always at least one angle at which the surface provides a sufficient direct bounce to differentiate it as the desired measurement. The rest of the measurements are thrown out (Mehrdadi et al, 1981).

Secondly, a method taking into account the second harmonics of ultrasound waveforms may be used. Kourtiche et al demonstrated that using the second harmonic in ultrasound reflection tomography adds valuable information and increases accuracy. To

do this, an ultrasound transducer is modified to collect both the fundamental and second harmonics of a reflected ultrasound, and both are used in the measurement calculations. They show by simulation that the side lobes of the second harmonic's PSF are much smaller than those of the fundamental signal; thus, more energy at the second harmonic level is directed towards the target. Using both harmonics is more complex, but it provides more information about the target (Kourtiche et al, 2003).

Deconvolution is the last method of removing spatial filtering effects from ultrasound measurements. Karpur et al report on the use of a Wiener filter based on the direct deconvolution of the PSF and the profile of the target. The Wiener filter successfully sharpens images taken by ultrasound, but is limited in its application. It may sometimes introduce ripple into an image because of noise in the system, and it requires prior knowledge of the PSF (Karpur et al, 1990).

Photo-acoustic (PA) imaging is a technique using lasers to induce ultrasound emissions in objects, that are measured by acoustic transducers. The advantage over normal ultrasound is that a laser is used to induce emission at a single point on the target as opposed to normal ultrasound imaging that measures the reflections of an ultrasound beam that is sent through an object. The laser is much more precise than the ultrasound beam. Wang et al developed a method for increasing resolution even further for PA imaging by deconvolving the acoustic response of the specimen and the laser energy absorbed by the specimen. The method estimates the surface of the object as a set of acoustic point sources excited by the laser. Wang et al report increases in spatial resolution to 0.3 mm (0.01 in.) (Wang et al, 2004).

Scanning Electron Microscopy

Scanning electron microscopy (SEM) measurements are generally accepted as extremely high quality, but spatial filtering does indeed still have the effect of reducing lateral resolution on the measurements. Lateral resolution is not often a problem in SEM; however, it has been noted that at the lower extreme of the measurement range (measuring samples with feature widths of only a few nanometers), errors are reported. The details are blurred and appear wider than they are in reality. Cazaux pursues the hypothesis that this limitation in lateral resolution is due to the beam width of the SEM and presents a simulation to demonstrate this phenomenon. The SEM beam energy distribution is modeled by a Gaussian function, and this is the point spread function applied to simulated features of widths both larger and smaller than this function. It was found that features smaller than the beam width appear to be widened or blurred just as they are by experimentation. Cazaux suggests two possibilities as solutions. First, the ideal solution is a deconvolution algorithm based on the PSF of the SEM to solve for the actual image; second, a calibration may be performed on known samples to arrive at an accurate model for each specific SEM setup. He suggests that the first solution is not reasonable except in limited cases where the measurement situation is nearly ideal, so the second solution must suffice in the absence of better instrumentation such as a transmission electron microscope (Cazaux, 2004).

Laser Probes

As in SEM measurements, the effects of spatial filtering are not usually considered in laser measurements since the laser beam is carefully focused on the target

so the effects of spatial filtering are negligible. However, at the lower extreme of the measurement capabilities, there is a noticeable effect. Ennos and Virdee present a method of increasing the quality of surface measurement by adding a surface form measurement taken by autocollimating laser light and measuring the angle at which the light is reflected using a position-sensitive sensor (Ennos and Virdee, 1986).

Eddy Current Probes

Eddy current probes are directly dependent on the actual measurement geometry. Eddy current probes generate electromagnetic eddy currents in conductive objects within the magnetic field of the probe; the strength of these eddy currents depends on the location and geometry of the object. Technically, this is an example of volumetric spatial filtering, since the magnetic field does not merely affect the surface of the target. Because of the complex electromagnetic interactions of eddy current probes, attempts are not commonly made to specifically understand the interaction. Rather, probes are calibrated to the measurement of specific geometries.

With his eddy current probe described earlier for measuring turbocharger blades, Rickman notes that the typical spacing of blades in a turbocharger is such that one blade does not fully leave the magnetic field before the next one enters. This blurring—spatial filtering—is seen as an advantage in this case since the output is nearly sinusoidal at the frequency of the blade passages, and hence the speed is easily detected. The voltages are calibrated for each sensor, and the electronics can accurately track the speed of blades; however, the purpose is not, in this case, to measure clearance, so the effect of spatial filtering is not considered further (Rickman, 1982).

Capacitance Probes

Capacitance probes measure the capacitance between two conductive plates; in doing this, the actual capacitance measurement is directly dependent on the geometry of the measurement situation. The capacitance is related by Equation (1). However, this formulation does not address more complex shapes or measurement geometries. For example, Gill et al studied capacitance probe measurements of turbine blades with a raised "fence" around the edge of the tip. The majority of the tip plane was lower. This was the largest recorded source of error in measurements. Their solution to this spatial filtering problem is to recalibrate for each blade/casing/probe-tip geometry so that accuracy is retained; even so, variation in the manufacturing precision of these blades was noted to produce up to 3.3% error in measurements (Gill et al, 1997).

Another method of compensating for this effect in capacitance probes is to change the measurement geometry of the probe in order to minimize spatial filtering. A smaller probe has finer resolution since the common shared area between the electrodes is smaller, and hence less vulnerable to macro-scale geometries of the blade tip. In effect, the probe senses less of the blade tip at a time, so measurements are less blurred. However, with this reduction in shared area comes a reduction in overall capacitance and therefore a smaller range. Since the measured capacitance is already very low, any reduction is difficult to accommodate from a signal processing standpoint. Sheard et al took advantage of this idea by placing a capacitance electrode on the end of an electromechanical probe that inserts the capacitance probe into the turbine, closer to the passing blade tips (Sheard et al, 1994).

Also as described previously, Drumm and Haase implement another method of reducing the effect of spatial filtering by changing the geometry of the sensor to better suit interaction with blade passages and to use a number of sensors stacked together to increase lateral resolution of time-of-arrival measurements. The sensor geometry they use is a series of capacitance probes that are rectangular in shape—close to parallel to the blade tips passing by. Drumm and Haase report less than 1 μm (0.00001 in.) resolution on blade tip clearance measurements and between 3 and 40 μm (0.0001 and 0.002 in.) lateral TOA resolution (Drumm and Haase, 2000).

Microwave Probes

In the sensor developed for detection of objects near a vehicle by Giubbolini, spatial filtering occurs with each of the sensors since each can take only one measurement at a time. To overcome this, an algorithm uses the point spread function of each antenna to compute the radial distance and echo intensity of each obstacle. A processing unit combines the information from multiple sensors to determine the final location. In this case, only the presence and location of a target is important—not any qualities such as geometry, so blurring of the targets due to spatial filtering is not a cause of concern (Giubbolini, 2000).

In Mazzucato's sensor for the measurement of plasma turbulence in nuclear experimentation, spatial filtering reduces the fluctuation of the plasma area to a one dimensional measurement, but Mazzucato developed a method of spatially measuring this turbulence using an array of small microwave receivers. Blurring still occur sinces the microwaves are not a perfect beam—though in measurements at this range, it is a more reasonable approximation (Mazzucato, 2002).

CHAPTER 5 EXPERIMENTAL SETUP

The experimental setup is designed to represent the measurement geometry of a turbine blade passing by the microwave sensor. Instead of using a whole disk of blades, only one blade is used since only one blade enters the antenna pattern at once. The blade is mounted on a precision motion stage in front of a microwave senor antenna. The experimental setup consists of three subsystems: 1) the microwave sensor, 2) the blade and sensor positioning apparatus, and 3) the desktop PC with National Instruments Data Acquisition (NI DAQ) interface, see Figure 7. Each of the three is described below.

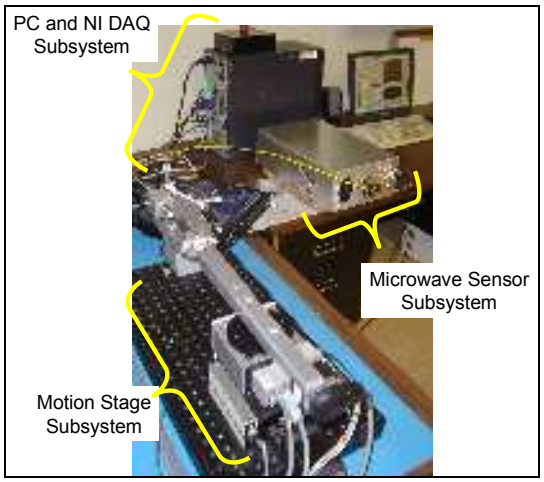

Figure 7. The overall experimental setup showing the microwave sensor, motion stage apparatus, and PC with NI DAQ interface.

Microwave sensor

The theoretical operation of the microwave sensor is discussed in Chapter 3. In this section, the practical components and design are described. The sensor subsystem may further be divided into three major components: 1) the Radio Frequency (RF) PC

board (PCB), where microwave signals are generated, received, and mixed; 2) the signal processing PCB, which controls the sensor and handles the digital processing of RF signals; and 3) the antenna and microwave cables, which carry microwaves to the measurement location and back. The sensor subsystem is controlled and monitored by a National Instruments data acquisition and control platform described later.

The microwave sensor used for this research operates at 5.8 GHz—an unlicensed band where cordless phones, some cell phones, and 802.11a wireless technology operate. The wavelength of microwaves at this frequency is approximately 50 mm (2 in.) in free space. One full revolution of the I and Q channels correlates with about 25 mm (1 in.) of target motion since the waves must travel to the target and back as well.

RF PC Board

The RF board is a PCB with microstrip transmission lines used for the microwave signals; Figure 8 shows the RF board with important components annotated. Microwaves originate at the voltage-controlled oscillator (VCO); the frequency of the RF signal may be adjusted by changing the input voltage to the VCO. The VCO has a range of 5.8 to 6.8 GHz. Microwaves travel from the VCO through a circulator and on to the antenna. Returning signals go back into the circulator but are directed around the circulator to the mixers. Out of the circulator, the microwaves pass through a 3dB split next—half is phase-shifted—and they are mixed with a reference signal directly from the VCO to obtain the Inphase and Quadrature channels used for measurements. These signals are transmitted to the signal processing board as well as the NI DAQ setup for analysis.

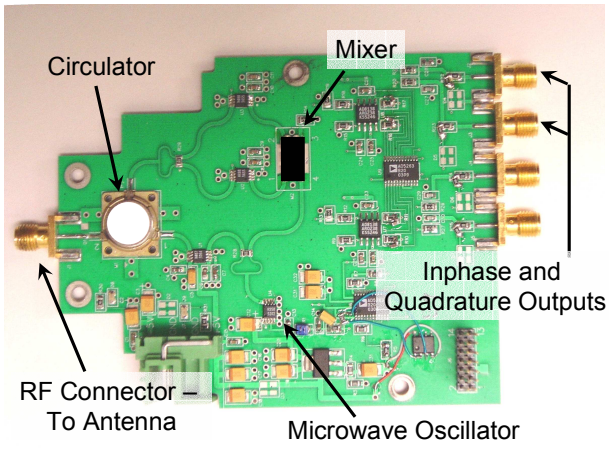

Figure 8. A picture of the RF PCB. Microwaves originate at the oscillator, travel around the circulator, and out to the target. Returning to the sensor, they once again travel around the circulator before they are mixed with the reference signal to create the Inphase and Quadrature channels.

Signal Processing Board

The signal processing PCB, shown in

Figure 9, is the second component of the microwave sensor. It is mounted to the RF board via a rigid 10-pin connector that is used for communication between the boards. The first function of the signal processing board is interfacing with the desktop PC; communication occurs between the sensor and PC through an RS-232 serial connector; commands are sent to the sensor and diagnostics and data are taken from the sensor. In addition, the signal processing board controls the RF board components (VCO, signal gains, power amplifiers, etc.) in accordance with commands from the PC. Lastly, the signal processing board receives and analyzes the Inphase and Quadrature channels from the RF board to calculate displacement. Displacement is output through a BNC connector on the front of the signal processing board.

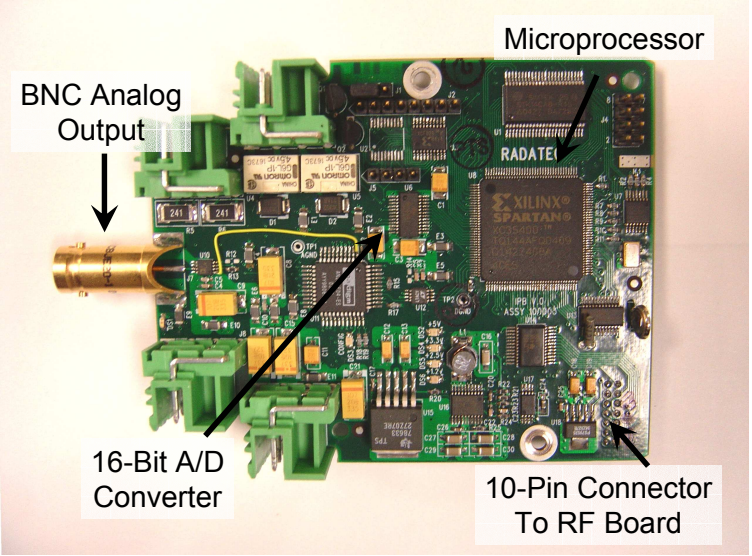

Figure 9. The signal processing PCB is where microwave signals are sampled and processed to calculate displacement measurements.

Microwave Antenna and Cables

The final parts of the microwave sensor are the antenna and cables. Microwaves travel through low-loss microwave cables, shown in Figure 10, between the sensor and the antenna. Because of the physics of electromagnetic waves, microwaves cannot travel through all types of electrical cables. Just as light needs a certain quality of cable—namely fiber optic cables—for transmission, so microwaves require special cables, which allow transmission in this portion of the electromagnetic spectrum.

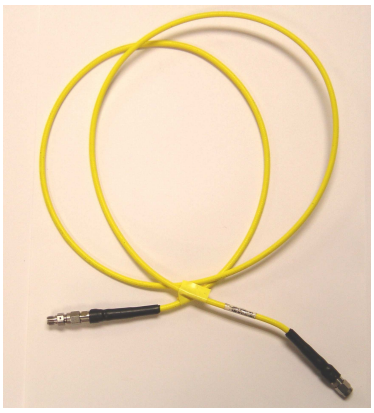

Figure 10. Microwave cable for transmission between sensor and antenna.

A microwave patch antenna is used for transmitting and receiving microwaves at the measurement location. This patch takes the form of a small, dielectric, ceramic puck with a platinum-palladium-silver (Pt-Pl-Ag) conductive film deposited on it; Figure 11 shows the antenna. Microwaves travel through the microwave cable segment and resonate the conductive film in such a way that it radiates microwaves into the surrounding atmosphere. Ordinarily, an aluminum casing houses the puck and connection for protection and mounting; however, the casing is not shown.

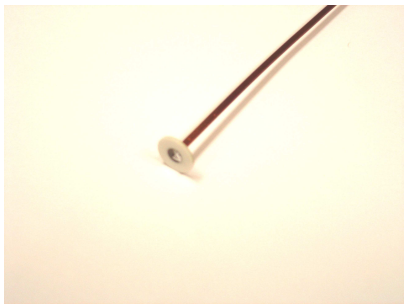

Figure 11. Microwave puck antenna with casing removed. Microwaves resonate the conductive, metallic surface on the puck and are transmitted into the atmosphere.

Blade and Sensor Positioning Apparatus

As will be shown later, measurement geometry is the factor that influences spatial filtering most directly. In experimentation, it is vital that this parameter is controlled precisely. In this experimental setup, the sensor is held fixed while the blade passes in front of it—just as in an actual turbine. The blade is held on an arm extending away from two motion stages that pass the blade in front of the sensor. The sensor is held on a five-axis precision stage. This allows the sensor to be positioned precisely relative to the blade. The sensor is positioned and then held fixed as the blade passes before it. All of these elements except for the blade and sensor are covered with microwave absorber to remove their influence from the measurements. Each of these components is described in better detail in the following paragraphs.

Experimental Blades and Blade Holding Apparatus

Two motion stages are combined to move sample "blades" in front of the sensor, simulating a real turbine situation. The setup is designed to be somewhat idealized in order to remove some of the uncertainty and complexities found in an actual turbine. The experimental blades are solid rectangular steel blocks of varying widths— 12.7 mm, 6.35 mm, and 2.54 mm (0.500 in., 0.250 in., and 0.100 in.). Figure 12 shows these blades.

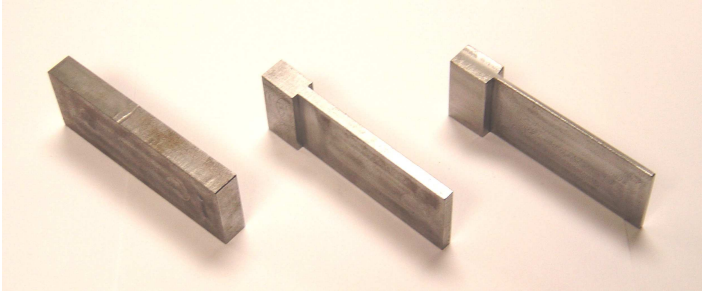

Figure 12. Test "Blades" used for experiments. The widths of these blades are 2.54, 6.35, and 12.7 mm (0.100, 0.250, and 0.500 in.).

These blades fit into a blade holder designed to allow free rotation of the blades for measurement in different configurations. This blade holder is on an approximately 25.4 cm (10.0 in.) arm attached to the two stages. Figure 13 shows this apparatus. The purpose of this apparatus is twofold. First, a typical military aviation turbine ranges from 20 to 40 cm (8 to 15 in.) in radius. The arm serves to extend the blades from the rotary stage so that the radius of curvature is in this range. Next, the arm serves to isolate the blade from other sources of reflection that might unduly influence the measurement.

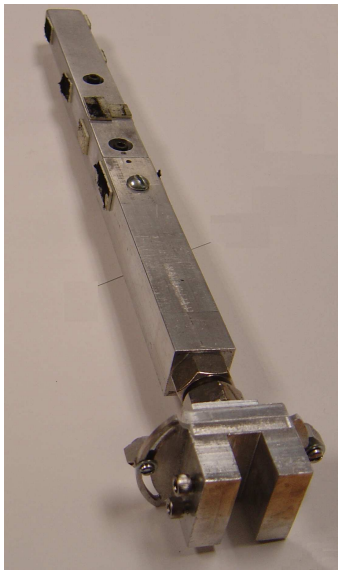

Figure 13. The blade holding apparatus and rotating arm holds the blades away from the rotary stage at a typical turbine disk radius.

Rotary Precision Stage

One stage is a rotary stage, shown in Figure 14, for swinging the blades in front of the sensor as they do in a turbine. This stage uses a stepper motor for control and has a rotary encoder connected for fine position measurement. The encoder is a US Digital E6D optical rotary encoder with 2048 counts.

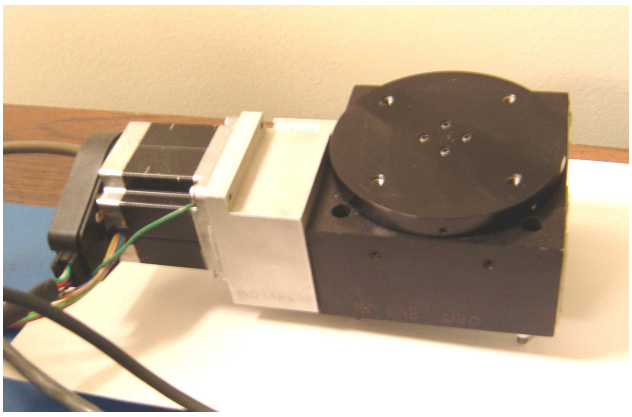

Figure 14. The precision rotary stage is used to rotate the blade past the sensor. A rotary encoder is mounted to the bottom of the stage (not shown) on the shaft that turns the circular plate seen above.

Linear Precision Stage

The rotary stage is mounted on top of a linear encoder, the axis of which is in line with the sensor. The linear stage is used for making fine and precise changes in blade clearance by moving the blade relative to the sensor. Linear motions are measured using a linear glass scale encoder. The encoder is an RSF linear glass scale encoder with a resolution of 1 μm. These components are shown in Figure 15

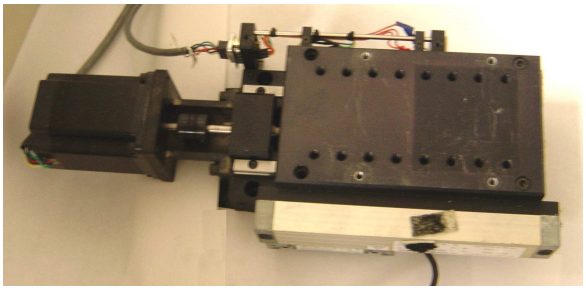

Figure 15. A linear motion stage controls the exact clearance between the blade and the sensor's antenna. A linear glass scale encoder (bottom of picture) is mounted to the stage for absolute measurements.

National Instruments Motion Control Device

For control of the two motion stages, a National Instruments Motion Control Board, MID 7604 shown in Figure 16, is used. This board translates commands from a LabVIEW PC interface into individual stepper motor commands, accounting for acceleration, velocity, and positional location. The motion board also translates signals from both the linear and rotary encoders into meaningful information in the LabVIEW interface. Lastly, the motion control board handles the low-level operation of the limit switches and stop buttons attached to the stage motions.

Figure 16. An NI MID 7604 motion control board is used for control of the motion stages.

Precision Antenna Positioning Stage

A five-axis precision positioning stage is used for fine positioning of the microwave antenna. A three-axis translation stage is mounted on top of a two axis rotation stage. The purpose is to position the antenna precisely relative to the passing blade for different measurement configurations. The two axis rotation stage is a Newport

Model 36 stage and is shown in Figure 17. The three axis translation stage is a Line Tool Co., ALH stage with resolution of 25 μm (0.00010 in.) and is shown in Figure 18.

Figure 17. A Newport Model 36 two-axis rotational stage controls tilt and rotation of the antenna relative to the passing blades.

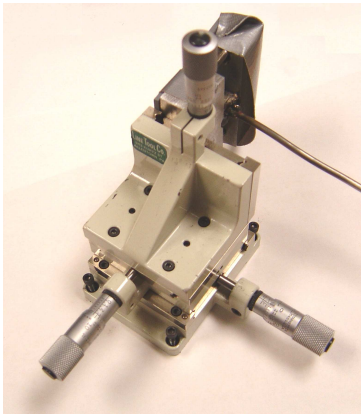

Figure 18. A Line Tool Co. three-axis translation stage is used for fine linear positioning of the antenna relative to the passing blades. In this picture, the cable of the antenna is also visible.

Desktop PC

A 2.53 GHz Pentium 4 desktop computer with 512 Mb of RAM is used for the overall control of the experimental setup. LabVIEW is used for computer-instrument

interface. A LabVIEW program coordinates motions, measurement from the sensor, signal and data processing, and sensor control.

Data Acquisition Device

The PC interfaces through a NI DAQ card, an M-series PCI-6221, to a DAQ control box, a BNC 2120, shown in Figure 19. The card has a 16-bit A/D converter for acquisition of analog inputs. Four channels are dedicated to reading encoder channels (two apiece for two encoders), and two channels are used for measuring the Inphase and Quadrature channels from the microwave sensor.

Figure 19. The NI BNC 2120 control box with BNC connectors for data acquisition.

LabVIEW Control Program

A LabVIEW control program coordinates the motions of the stage and manages sensor functionality. The program moves the stage in response to human commands or it can run set patterns for experimental automation. As the stage moves, data from the sensor Inphase and Quadrature channels is acquired at each encoder step; this allows precise measurements to be made and compared to actual stage motions. The control

program then deciphers the data and runs calculations to determine sensor displacement measurements, which may be logged and saved for later processing.

The control program also commands the sensor operation. This includes changing sensor settings, running calibrations, and monitoring sensor accuracy. Sensor settings that can be adjusted are RF power level, Inphase and Quadrature channel gains, and VCO setting. In addition, certain signal processing variables for the on-board data processing can be changed; however, these parameters are not used in this experiment since all data processing is done with the desktop PC. Calibrations must be run in order to determine optimal operating conditions for the sensor and antenna. As stated above, each antenna has a certain range of transmission frequencies. The frequency at which the greatest amount of microwaves is transmitted out of the antenna is referred to as the center frequency. The control program in conjunction with an RF spectrum analyzer can be used to determine and set the sensor at this frequency for measurement. Also the Inphase and Quadrature channel gains must be calibrated to maximize the amplitude level of the received signals without saturating, causing distortion and inaccuracy. Last, the RF DC offset is another variable that must be calibrated for each experimental setup. The DC offset is added into the I and Q channels before amplification to insure they amplify within the desired range.

CHAPTER 6 COMPUTATIONAL MODEL DEVELOPMENT

Introduction

Spatial filtering in metrology is a result of measurement geometry. In the case of the microwave sensor presented, blades are blurred due to the large spot-size of the sensor relative to the size of the blades. A computational model of the sensor provides valuable insight into the interaction between the sensor and target; it is a platform for comparing the theoretical knowledge of sensor operation with reality. Deviations between the model and reality are the result of: 1) a deficient understanding of the governing theoretical background or 2) the influence of factors for which the model does not account.

The computational model isolates certain factors of measurement geometry and wave interaction that are the main causes of spatial filtering in turbine blade measurements. The model is purposefully idealized and simplified from reality to determine the influence of these factors. In the model, a simplified blade is swept past a simulated sensor and simulated measurements are generated by mathematical calculation based on the sensor-target geometry.

Novak and Miks delineate two general concepts that most non-contact measurement systems operate based upon. The first is the ray method; in this method, the target is treated essentially as a mirror that reflects differently based on the geometry of the situation. The second method is the interferometric method; interferometric measurements are based on the interaction of a target with an electromagnetic wave-field (Novak and Miks, 2002). This microwave sensor does not fit cleanly into either

category, so elements of both are considered in the calculation of a geometric model. The sensor measures the reflected energy off of the target as described by the ray method; however, since the target is in the near-field of the antenna, the interference of transmitted and reflected waves is significant. The model combines both of these methods to calculate a vector for each individual measurement that contains both its intensity and phase. These vectors are summed to arrive at the final simulated measurement. The first step is to generate a geometric model, and then the electromagnetic calculations are performed on this model.

Geometric Model Generation

The geometric model has two parts: the blade and the sensor. The blade is generated to model the idealized blades used in experimentation. All of the surfaces of the blade (including the corners) that can reflect microwaves back to the sensor are modeled. For the sensor, only the aperture of the antenna need be modeled since it is the only point where microwaves are transmitted and received. The blade and sensor aperture are modeled as three-dimensional finite-element objects, replacing a continuous area with a set of discrete points. The following paragraphs provide a detailed description of these two elements.

Blade Simulation

The blade in the model is simulated by a three dimensional point-mesh covering the important surfaces. The simplest way to do this would be to set points evenly along the blade, spaced by some constant length. However, the mesh must be sufficiently dense so that the model adequately approximates the actual surface. The simulation is

run with clearances between the sensor and blade of only tens of μm (a few thousandths of an in.), so the density of the mesh needs to be on this order or smaller. A modeled blade with a full mesh dense enough to meet these requirements would be well over 10,000 points, and calculations would be enormous—many hours per simulated blade pass on a 3 GHz Pentium IV PC. To solve this difficulty, a method of variable density meshing was developed; the density of the mesh is greater in places close to the sensor and is less in places far from the sensor. The number of points in the mesh is greatly reduced with minimal loss of precision in the model. Figure 20 shows a comparison between a fully dense mesh and a variable density mesh. Note that in this figure, the blades have approximately the same number of points, but the variable density mesh provides a much denser mesh near the sensor.

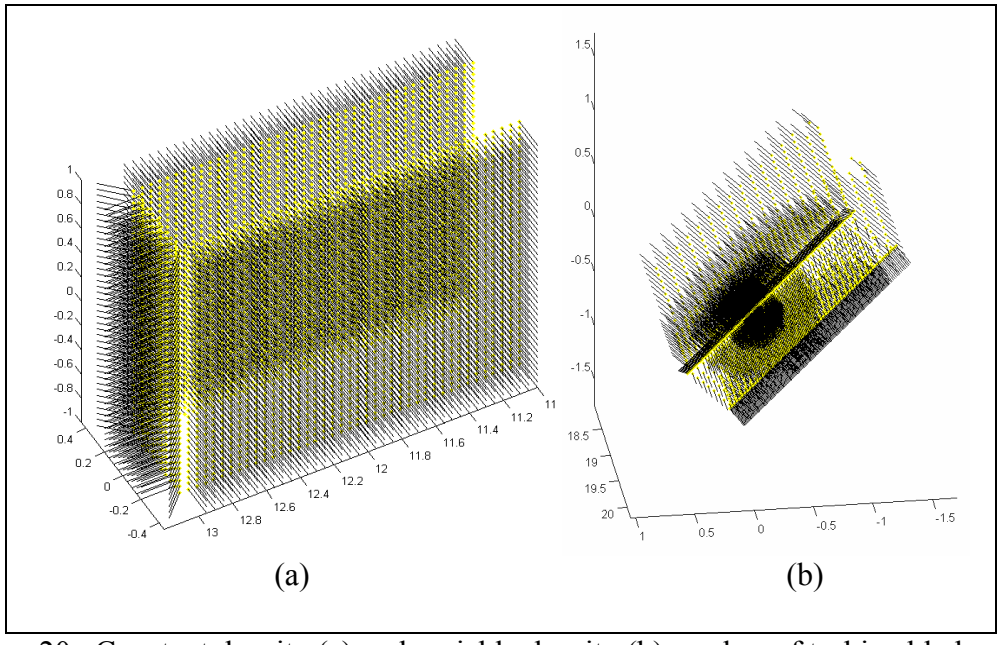

Figure 20. Constant density (a) and variable density (b) meshes of turbine blades with surface normals extending.

When performing simulation calculations on each element, two geometric values for the blade elements are important, which are calculated and associated with each point. First is the area that each point represents, and second, the direction in which each small area points. The model assumes perfectly flat sides and tip to the blade, and normal vectors that are perpendicular to those surfaces. The normal vectors at the corners are calculated to be the average of the normal vectors of the two surfaces that they adjoin. Though this blade model is greatly simplified from an actual turbine blade, it very closely models the experimental blades used in this research.

Sensor Simulation

The sensor's antenna can be modeled in two different ways. The first, and most simple, is to model it as a point source, and the second is to model it as an area filled with point sources. The first is the simpler computationally, but it does not take into account one important aspect of spatial filtering. That is, it does not account for the fact that the points along the antenna aperture may have a very different perspective of the blade, depending on the size of the aperture relative to the size of the blade. The averaging of these different perspectives is one cause of the blurring that occurs due to spatial filtering.

Each point along the antenna aperture also has a normal vector associated with it that is used in computation of the position of the blade points within its field of view, as well as a power distribution pattern. The normal vector associated with each antenna element is in the direction perpendicular to the antenna aperture. The sensor's antenna does not either emit or receive signals equally in all directions, so the normal vector determines the direction of the signal field around the antenna aperture. Figure 21 shows

the radiation distribution of each antenna element modeled according to Equation (10) (Johnson, 1993).

$$P_r = P_t \cos(\beta_{ij})^{1.5} \tag{10}$$

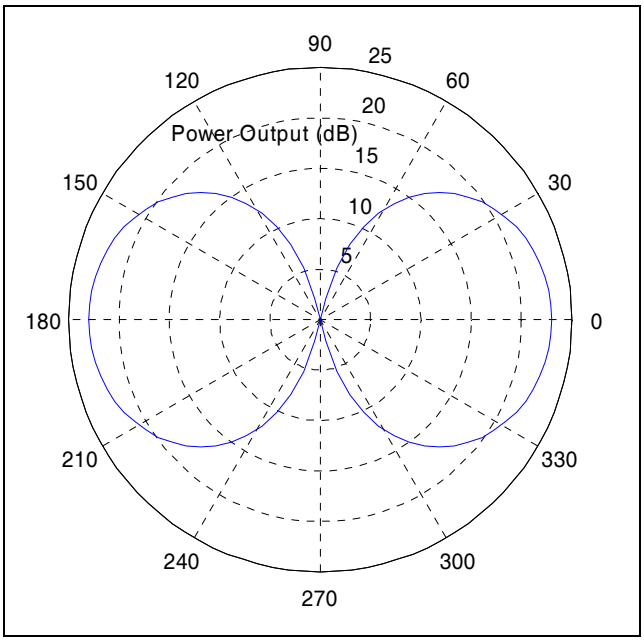

Figure 21. The electromagnetic radiation pattern from a single antenna element. The radiation from many elements such as this one add constructively and destructively to form the full antenna radiation pattern.

All of the sensor elements combine to form the overall antenna pattern. However, the microwaves radiated from each antenna element have not only a magnitude (or power of radiation) associated with them, but they also have a phase related to the distance traveled by the wave. The phase of a microwave at a certain distance is calculated by (6) above, repeated here for convenience.

$$\theta_{\text{relative}} = \theta_0 + \text{mod}\left(\frac{2d_{\text{absolute}}}{\lambda_{\text{air}}}\right) \cdot 2\pi$$

Microwaves with differing phases interfere constructively and destructively to form the antenna pattern. Typical radars have apertures that are much larger than the wavelength of the signal, and the antenna pattern in the most commonly used range (the far-field) is fairly complex. It generally follows the form of a sinc function with one central main lobe and smaller side lobes. The model results are consistent with this general form. Figure 22 shows the three-dimensional antenna pattern for the situation where the wavelength is much smaller than the aperture size. In this simulation, the antenna pattern is shown for a distance in the far-field region of the operational range of the sensor. Note the central lobe and smaller side lobes, which is consistent with microwave antenna theory.

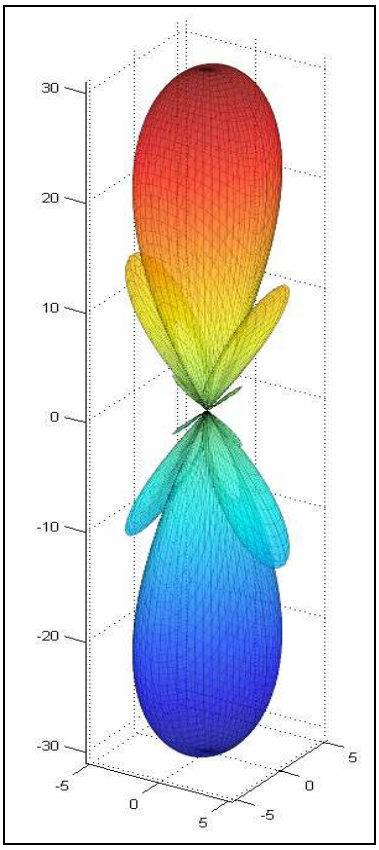

Figure 22. The antenna pattern calculated by the model for the situation in which the wavelength of microwave much shorter than the antenna aperture.

For the case of the sensor used in experimentation, the aperture of the antenna is significantly smaller than the length of waves used. Figure 23 shows the three-dimensional antenna pattern for this case. Note that there are no noticeable side lobes, and the central lobe is much more evenly distributed directionally.

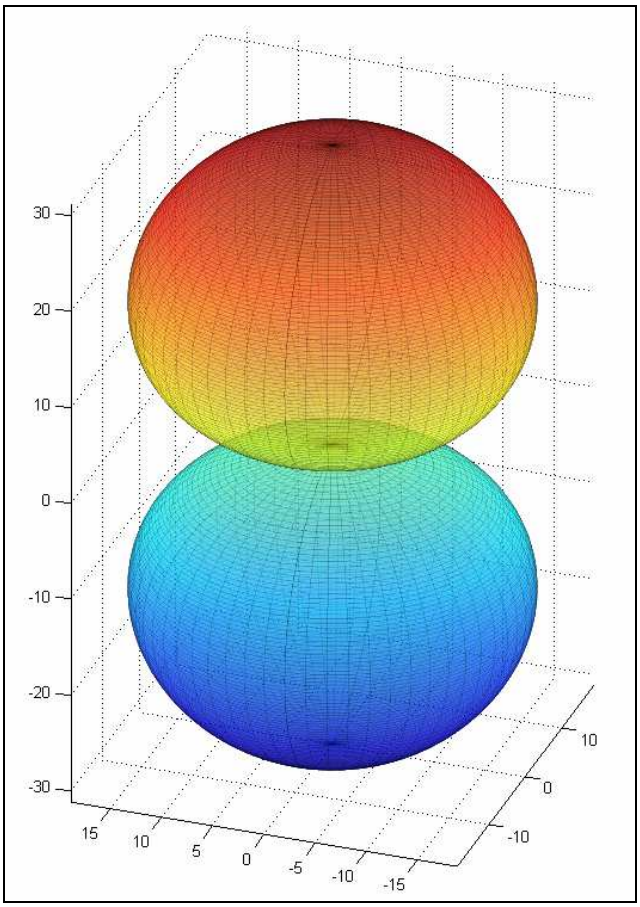

Figure 23. The antenna pattern calculated by the model for the case in which the wavelength is longer than the antenna aperture diameter.

Neither of the antenna patterns shown above (Figure 22 and Figure 23) is radially symmetric. This is because of the power distribution of the sensor. When leaving the sensor aperture, waves are polarized—aligned directionally with each other. Since the waves are polarized in a certain direction, they have greater amplitude along the center of the aperture in the direction of the polarization. Figure 24 illustrates the normalized power distribution due to polarization across the sensor.

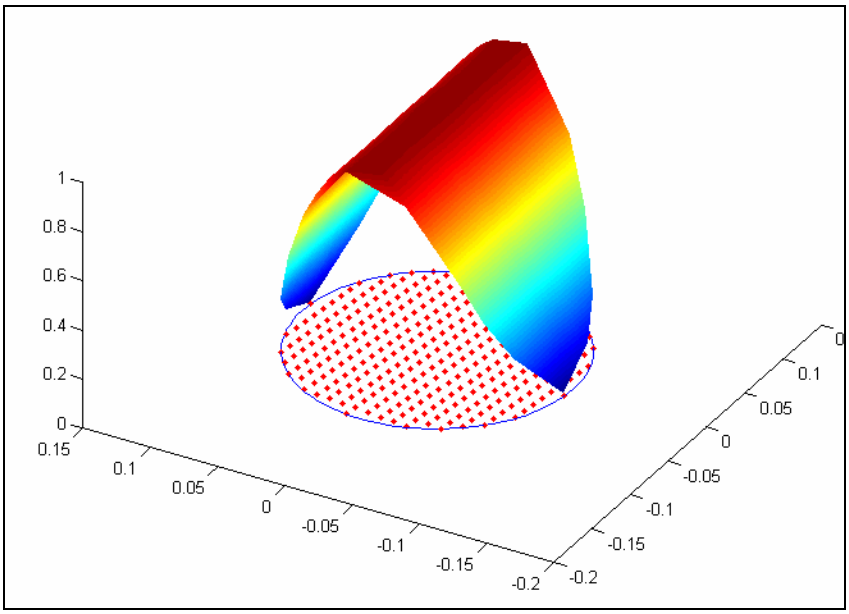

Figure 24. The normalized power distribution due to polarization across the sensor aperture.

The following equation describes this polarization

$$S_j = \cos\left(\frac{x_j}{r_{\text{sensor}}} \cdot \pi\right) \tag{11}$$

where S_j is a scale factor between 0 and 1 which scales output power between 0 and peak power according to the x-location, x_j, of a particular point within the sensor aperture.

The antenna pattern also changes according to the distance from the antenna. As introduced in Chapter 3, there are three major regions for each antenna: the reactive near-field, the radiative near-field, and the far-field. The far-field is the simplest since the antenna pattern changes little as distance increases or objects come in front of the antenna. The radiative near-field is the region from about 3λ from the antenna up to the far-field region. Within this region, the antenna pattern is much less stable with respect

to distance; this is because of greater interactions between microwaves since the size of the aperture is significant relative to the distance from the aperture. The reactive near-field, is the region within 3λ from the antenna, and it is the most complicated of the regions, since interactions between the antenna and objects in front of the antenna can drastically change the radiation pattern of the antenna itself. Figure 25 shows the antenna pattern throughout the different regions.

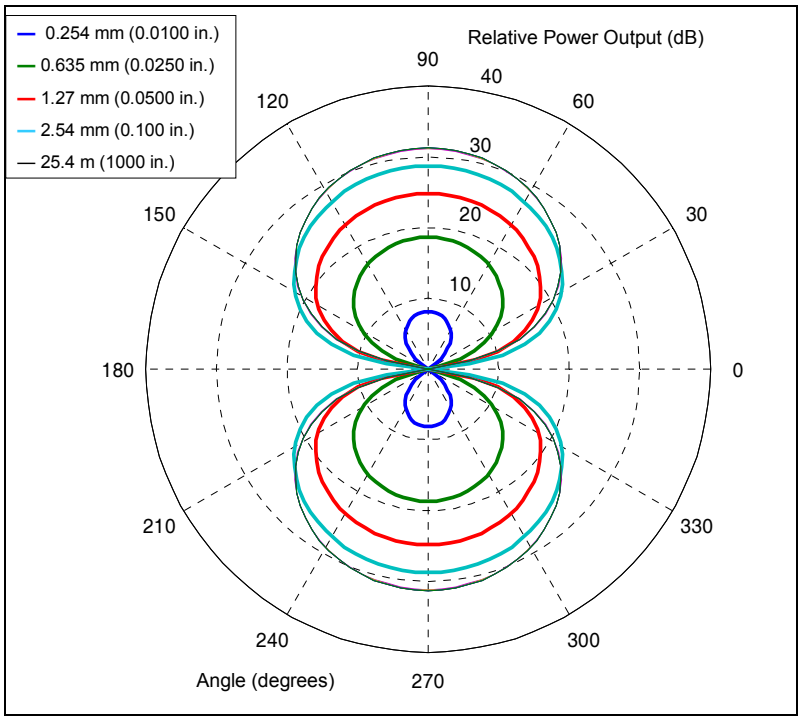

Figure 25. The antenna pattern of a sensor with an aperture size, d = 5.13 mm (0.202 in.), and wavelength, λ = 51.71 mm (2.036 in.), over a range of distances through the fields of the antenna.

Determination of Radar Cross-Section

Radar cross-section (RCS) is a metric of the amount of energy reflected by a target. The RCS is the magnitude of the measurement vector. Modern computer

graphics calculate illumination of scene using the ray-tracing techniques applied here. For reference, the author suggests (Bret, 1992). For the model, microwaves are assumed to behave in the same manner as light waves. The RCS of a target is analogous to the intensity of reflected light in computer graphics renderings.

There are three major factors associated with the blade geometry and two major factors associated with the sensor geometry that affect the RCS of a single point measurement in the model. First, the angle of incidence determines the diffuse and specular reflection of microwaves off of the target. Computer graphics models use Equation (12) to describe the diffuse reflection of an electromagnetic ray.

$$I_r = I_s k_d (N \bullet L) \tag{12}$$

I_r is the reflected intensity, I_s is the intensity of the source, k_d is a diffusion constant that varies according to surface quality, N is the vector normal to the surface, and L is the vector in the direction of the ray source. The angle of incidence is the angle between N and L, and follows Equation (13).

$$\cos(\theta_i) = N \bullet L \tag{13}$$

Along with the diffuse reflection, a specular reflection component is present. This specular component accounts for the shininess of the surface. A perfectly smooth and reflective surface, like a mirror, reflects incoming light away from the source, but other surfaces do not reflect this light so purely and some is sent off in every direction. The

same is true of microwaves. From computer graphics, a specular reflection is computed using the following equation:

$$I_{\mathrm{r}} = k_{\mathrm{s}} I_{\mathrm{s}} (H \bullet N)^{m}, \tag{14}$$

where k_{s} is a specularity factor, H is the vector bisecting the direction of reflection and the angle of incidence, and m is a shininess factor of the electromagnetic source.

The second factor based on blade geometry is the distance between each point and the sensor. Microwaves, like other electromagnetic waves attenuate with distance; this factor is approximately quartic according to Equation (15).

$$I_r = \frac{I_s}{d^4}, \tag{15}$$

where d is the distance between the point sensor and the point on the target. However, in the reactive near-field attenuation may follow a non-linear pattern causing less attenuation over distance.

Last, the area that each point represents determines the amount of energy reflected back to the sensor. The amount of energy is directly proportional to the area of reflection and the intensity of the source as described by Equation (16).

$$I_{\mathrm{r}} = I_{\mathrm{s}} A \tag{16}$$

With respect to the sensor, the first factor in RCS calculation is the angle off the central axis of the sensor. Each antenna has a specific antenna pattern associated that describes the amount of energy released from the antenna at different angles off the central axis. The current sensor has a center lobe that is largest and has been seen to diverge at approximately 45° from the end of the sensor. Equation (10) above describes this pattern in relation to the angle off the central axis of the antenna.

The second factor is the position within the sensor aperture; this is the effect of microwave polarization in the antenna. Figure 24 shows the power distribution across the sensor aperture. More power is transmitted and received along the polar axis than away from it.

Vector Sums and Final Measurement Calculations

All of the factors described above contribute to the calculation of the RCS of each model element from each sensor element; this is the magnitude of a vector representing each individual element-to-element measurement. The phase of each vector is calculated from the distance traveled to the blade and back to the sensor. For each sensor element, then, all of the measurement vectors to the blade elements are added together to solve for the sensor element measurement. All of these measurements are scaled according to the position within the sensor aperture and then are added to determine the final sensor measurement for a given measurement geometry. This is a simple vector sum, and the final result is a vector of some magnitude and phase corresponding to the overall strength of the received signal back at the sensor and the phase of the aggregate measurement taken by the sensor.

The phase between a given sensor element and blade area element is calculated as follows:

$$\theta_{ij} = \mathrm{mod}\left(\frac{2d_{ij}}{\lambda}\right)\cdot 2\pi \tag{17}$$

The RCS is then calculated by

$$R_{ij} = \left(P_{\mathrm{t}}\cdot\cos\left(\beta_{ij}\right)^{1.5}\cdot\cos\left(\frac{x_j}{r_{\mathrm{sensor}}}\cdot\pi\right)\right)\cdot\frac{k_{\mathrm{d}}\left(N_{ij}\bullet L_{ij}\right)+k_{\mathrm{s}}\left(H_{ij}\bullet L_{ij}\right)^{m}}{d_{ij}^{4}}\cdot A_i \tag{18}$$

The ray-tracing constants, k_{d}, k_{s}, and m are chosen based on typical values for computational graphics applications and based on the theory behind the model. The surface of steel is relatively very reflective of microwaves. Thus, the surface is modeled as essentially a microwave mirror. k_{d} and k_{s} are both set to one, and the shininess factor, m, is set to 3, based on the typical value of a mirror-like surface in computer graphics. Under these assumptions, the modeled blade reflects much more energy when a surface is perpendicular to the sensor aperture, and there is only a small diffuse reflection component. The influence of these factors is consistent over all of the experiments. As the model parameters change, the influence of these model constants changes continuously. Hence, the trends shown by the model are still consistent, though me magnitude of those changes may not absolutely accurately model reality.

Finally, the vectors formed by the phase and RCS calculations are added together resulting in the final measurement

$$R_{\text{total}}\angle\theta_{\text{total}} = \sum_{j}\sum_{i} R_{ij}\angle\theta_{ij} \tag{19}$$

Simulation Measurements

This model is designed to simulate blades spinning past a sensor in a turbine; it is simplified to measure only one blade at a time, and the blade is not fixed to anything. MATLAB is used to implement the model. The MATLAB script calculates a blade mesh from the measurement orientation and a set of experimental parameters describing the geometry of the blade and sensor. The model then steps through a blade pass, incrementing the angle of the blade and performing all measurement calculations at each step. The result is the magnitude and phase at each step through the blade pass. The model is sufficiently general to update all of experimental parameters based on user input. Note that the mesh generation and measurement calculations are independent functions. This means that the model could potentially be used in the future to load in more advanced three dimensional models of actual turbine blades, and measurement calculations could be run without further development of the simulation. The mesh currently models only the experimental blades used in this thesis, and is optimized for speed of computation.

CHAPTER 7 FULL-FACTORIAL DESIGN OF EXPERIMENTS

Introduction to Designs of Experiments

Designs of experiments (DOEs) are intended to qualitatively and quantitatively characterize a complex system's responses to individual input factors. This is accomplished by systematically varying inputs and measuring the responses thereto. Statistical analysis then determines the probability of relationships between individual inputs and responses. In general, this statistical analysis tests only for linear relationships, though more-involved, non-linear trends are sometimes of interest. DOEs are primarily used for discovering and broadly describing trends rather than characterizing them in full detail, so linear trends are usually a sufficient analysis tool.

A factorial DOE is one that varies input parameters in experimentation to represent the full spectrum of possible combinations. Many input factors vary continuously (e.g. an infinite number of temperature settings over a range); others are discrete (e.g. the number of targets in front of a sensor). In designs of experiments, each input factor, whether continuous or discrete, is represented by specified discrete values over a certain range. A full-factorial DOE contains every possible combination of the discrete input parameters, while a partial-factorial design only selects a certain percentage of the exhaustive design. A full-factorial design is the most thorough investigation of the parameters' relationships, but the number of experiments grows exponentially as more and more input parameters are considered or as the number of discrete steps for each parameter is increased. Therefore, there is a trade-off between the detailed characterization of individual factors and the breadth of the overall design. A design with

few factors can afford to contain more discrete steps for each of its parameters; however, this style of design cannot consider all of the input factors possible to a complex system.

A Design of Experiments for Spatial Filtering of Turbine Blades

Spatial filtering is a complex phenomenon affected mostly by geometric factors of the measurement situation. In measuring turbine blades in-process with a microwave sensor, many geometric factors may vary. First, the shape of the blade itself may vary greatly from turbine to turbine—even from stage to stage in the same turbine. Blade shape factors include blade width and blade twist angle. Next, the geometry of the blade relative to a sensor at the casing may change from blade to blade. This factor may even change within a single stage—not to mention from stage to stage or turbine to turbine. The relative geometry factors that vary are the clearance between the blade tip and the turbine casing and the orientation of the blade relative to the sensor. Orientation is further divided into the three rotational angles of the blade—twist, tilt, and approach angle. The DOE in this research is a full-factorial design including all five factors. Each of these factors is explained, analyzed, and illustrated in a later section of this chapter.

The DOE tests for the influence of each of the five geometric factors mentioned above in two or three discrete levels. Both blade width and tip clearance each have three levels and the three angle factors each have two levels. Table 1 shows each of these factors and their respective levels.

Table 1. Design of Experiments input factors and their respective levels.

Experimental Factors	Low Level	Medium Level	High Level
Blade Clearance	1.27 mm (0.0500 in.)	2.54 mm (0.100 in.)	7.62 mm (0.300 in.)
Blade Width	2.54 mm (0.100 in.)	6.35 mm (0.250 in.)	12.7 mm (0.500 in.)
Blade Twist	0°	N/A	45°
Blade Tilt	0°	N/A	3°
Approach Angle	0°	N/A	3°

The full-factorial design exhausts all combinations of these factors and levels, giving 72 different experiments. Each of these experiments is run three separate times, totaling 216 individual experimental runs. A run consists of four consecutive blade passes with the five factors held constant at their respective levels. The order of the experiments is random, and the experimental setup is reset between each experiment; this is to ensure randomization of errors. Random errors will not affect the overall trends as much as the confidence and quantitative accuracy of the DOE.

The use of a developmental microwave sensor introduces other factors that affect spatial filtering. These include sensor performance factors such as the microwave power level and wavelength. Also, there are cable and antenna factors such as cable loss, connector reflectivity, and antenna pattern. The purpose of this research, however, is more toward understanding the measurement of turbine blade tips than developing the sensor itself. Thus, these factors are held at a constant nominal configuration during all experimentation. A single sensor setup is used for all experiments, but it is representative of actual microwave sensor setups used for turbine blade measurements. In the end, fine measurement characteristics may vary slightly from sensor to sensor and antenna to antenna, but broader trends will be similar. Overall trends in the relationships between the factors are the most important result, rather than specific quantitative associations.

The trends lend themselves to understanding the causes of and variation in spatial filtering due to the geometric input factors.

The trends relate the input factors to certain defined responses. For each blade pass, the inphase and quadrature signals are stored. This data is processed in order to derive the desired responses. The responses are the meaningful part of the data that change in response to the input. In this case, the responses are the point of maximum phase (the tip of the blade), the maximum strength of the returned signal, and the apparent width of the blade. These responses give well-defined, simple numeric data points for each blade pass that are easily used for analysis in the DOE. Changes in these responses indicate the influence of spatial filtering. The next section discusses each response in detail. Following that, the experimental input factors are discussed along with their theoretical influence on each response.

Data Processing and Design of Experiments Responses

In these experiments, the data taken are the voltages of the inphase and quadrature channels of the microwave sensor. As described in Chapter 3, these channels are along the axes of the complex plane, and the displacement measurement is the phase of the recorded value relative to the DC center. Figure 26 shows a typical blade pass Inphase/Quadrature plot. Each point along the plot represents a measurement with some phase and RCS related to the distance to the reflection point and the strength of the reflection.

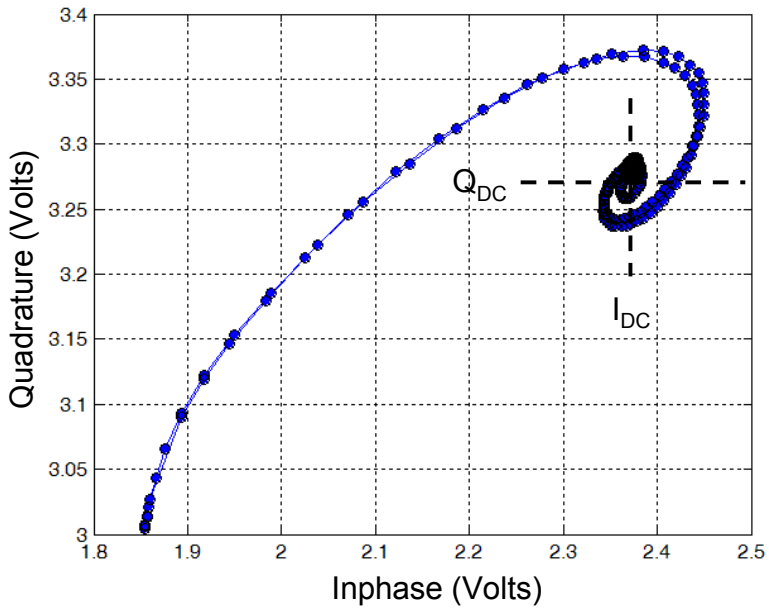

Figure 26. The Inphase vs. Quadrature plot of measurements taken throughout a single blade pass.

From this data, the phase and RCS are calculated relative to the DC center. Figure 27 shows the phase plot of the same blade pass; Figure 28 shows the RCS plot. The position of the blade is known from the rotary encoder that is monitored by the National Instruments DAQ system.

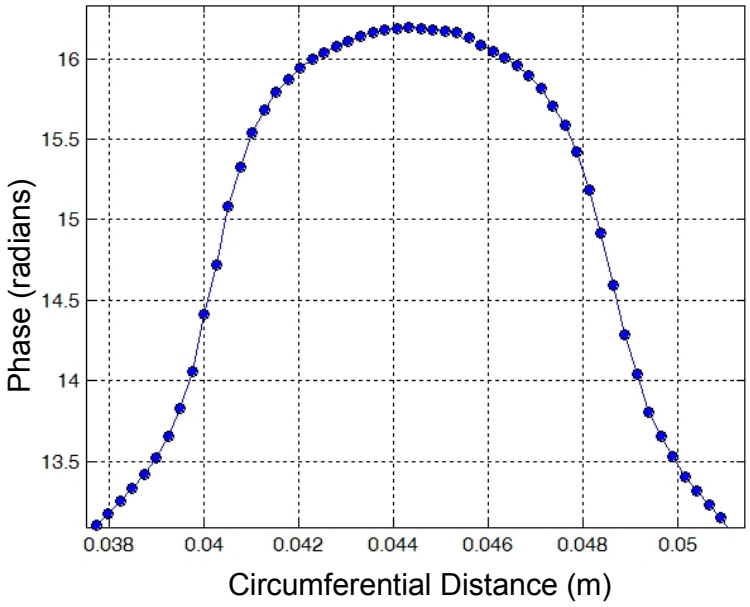

Figure 27. The phase plot of the blade pass; the tip is rounded because of spatial filtering.

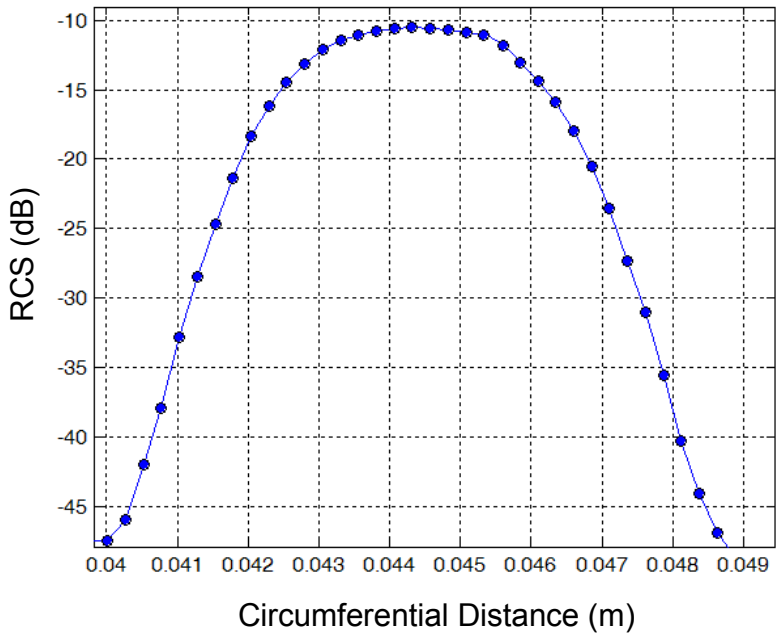

Figure 28. The RCS plot of the blade pass; the RCS of a blade pass is very similar in shape to the phase of a blade pass.

The DOE responses are derived from these two plots—the phase and RCS of the blade passes. Blade tip phase and apparent width are derived from the first plot, and maximum RCS is taken from the second. These three responses are discussed below.

Response 1: Blade Tip Phase

Blade tip phase is the point of maximum phase throughout the blade pass. Displacement measurements by this microwave sensor are directly related to the phase of measurement. As stated before, the displacement is calculated from phase by Equation (7). This response should exactly correlate to the clearance; in other words, blade tip phase should change if and only if the clearance of the blade tip changes, and the change should be exactly proportional relative to the wavelength. However, spatial filtering causes discrepancy between these two. The blade tip phase responds also to other

geometric factors of the measurement situation—such as the actual width of the blade and the angle of the blade relative to the sensor.

Response 2: Apparent Blade Tip Width

As seen in Figure 27, microwave measurements do not capture the ideal shape of a blade. The ideal shape of a blade rotating by a perfect sensor looks like the simulated measurement in Figure 29.

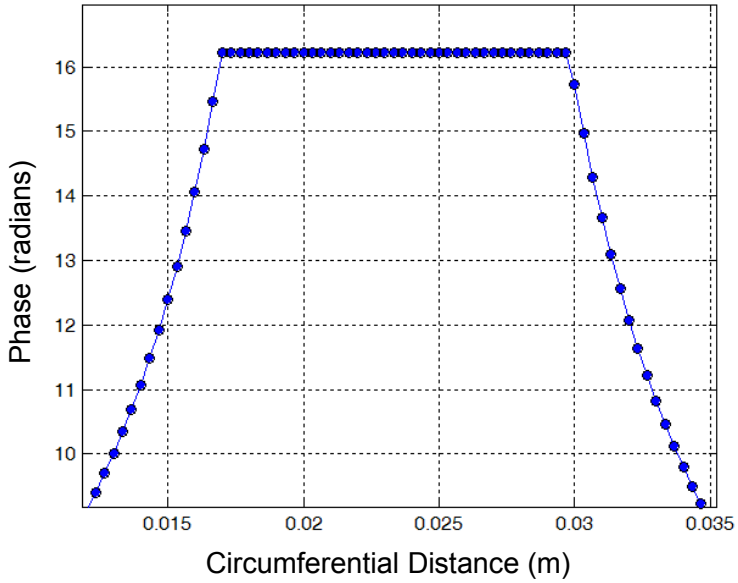

Figure 29. The ideal phase plot of a test blade like those used in experimentation. The actual phase plot is much rounder at the tip, so blade width is not well-defined.

Spatial filtering causes the blade to have a more rounded shape at the tip. Spatial filtering has essentially the same effect on the blade waveform as a low-pass filter has on a signal in classical signal processing. As a result, tip width is not obvious since the corners are obscured. Thus, for the purposes of this research, apparent tip width is

defined as the width of the blade at predetermined phase intervals from the point of maximum phase. Figure 30 illustrates this apparent width.

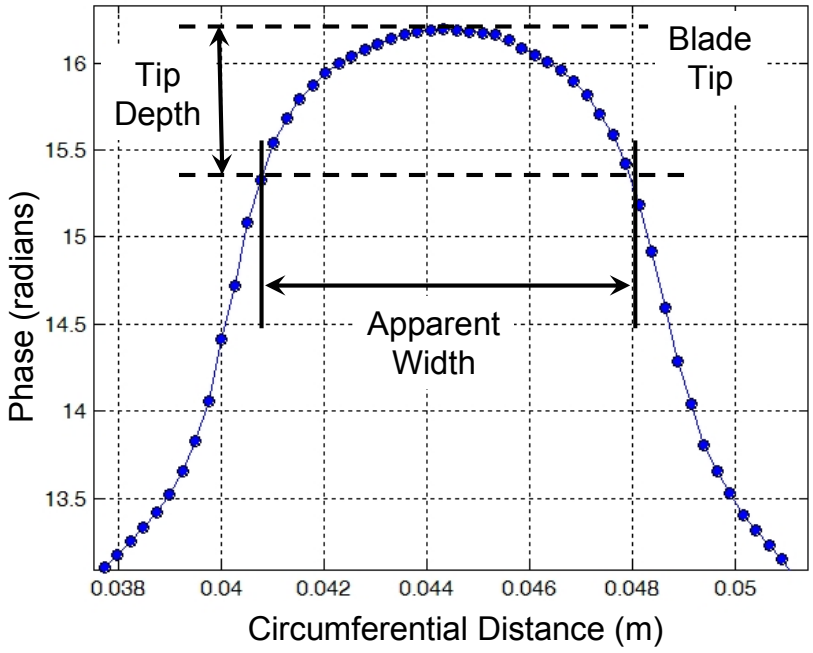

Figure 30. Apparent tip width is defined as the width of the blade pass profile at a certain phase depth below the peak.

Since this response is less clearly defined, three values are used for comparison. The apparent width is measured at 1.27, 2.54, and 5.08 mm (0.0500, 0.100, and 0.200 in.) down from the tip; with a frequency of 5.8 GHz, this corresponds to a phase change of 0.154, 0.309, and 0.617 radians.

Response 3: Maximum Radar Cross-Section

In the case of these blade passes, the RCS plot (Figure 28) of the measurements resembles the phase plot (Figure 27) in shape very nearly. This is because more and

more reflected energy reaches the antenna aperture as the blade approaches, and it generally peaks as the blade passes directly in front. Just like the phase, the RCS is spatially filtered so that it is smooth—without the corners of the blade visible. Small geometric discrepancies change the reflections significantly, affecting overall RCS. The greatest single influence on the amount of energy reflected back to the antenna is the clearance between the blade tip and the sensor.

Design of Experiments Input factors and Hypothetical Results

As stated above, spatial filtering in measurements made by the microwave sensor is affected by the blade geometry and the geometry of the measurement situation. With regard to blade geometry, the two most fundamental factors affecting spatial filtering are the width of the blade at the tip and the twist of the blade. These two factors differ between turbines. The geometry of the measurement situation is defined by the clearance between the blade tip and casing and the orientation of the blade relative to the sensor. Orientation is defined by the three angles of the blade relative to the sensor. Each of the five factors is an input to the design of experiments. In the following paragraphs, they are described in detail and their theoretical influence on sensor measurements is presented.

Blade clearance

Blade clearance is the perpendicular distance from the sensor to the tip of the blade at its closest position. The linear stage is used to vary this and since only relative measurements are made by the sensor, a Starrett feeler gauge serves to measure the initial absolute clearance for each run. In theory, three things happen as the tip clearance

increases: First, the RCS of the reflected signal is reduced. This is because microwaves attenuate more as the distance traveled increases. Second, the sensor sees more of the blade at a time since the size of the field-of-view (spot-size) increases as distance increases—one of the main causes of spatial filtering. Third, the phase of the entire measurement shifts according to the change in clearance. Sensor operation is based on this principle.

In aviation turbine engines, the clearance between the case and the blade tips is typically in the range of 1.3-2.5 mm (0.050-0.10 in.), and this never changes more than 1.3-1.9 mm (0.050-0.075 in.) during normal operation. However, in larger, power-generation turbines, the clearance can be up to 12.7 mm (0.500 in.), with variation of as much as 5.08 mm (0.200 in.). Hence, the experiments cover a range of 1.27-7.62 mm (0.0500-0.300 in.) in accordance with these typical ranges.

Within about 7.62 mm (0.300 in.) of the antenna, at 5.8 GHz, one enters the reactive near-field of the antenna as discussed in Chapter 3 above. Especially for small antennas, the range and effect of this field is unsure; this is the reason there are three levels for this variable—to provide more information to accurately characterize it. The value of 2.54 mm (0.100 in.) is chosen based on qualitative preliminary experimentation suggesting that below 2.54 mm (0.100 in.), waveforms and RCS may not change consistently and measurements may be inaccurate.

Blade Width

The length of time that the blade is in front of the sensor, how much of the blade is within the FOV of the sensor at a time, and how much closer the corners come to the sensor than the center of the blade are all determined by blade width. The relative size of

the blade with respect to the sensor aperture is the most important factor in determining the effect of spatial filtering between different blade widths. This is because the blade-width-to-sensor-aperture ratio determines how much of the blade the sensor can "see" at a given time. For example, if the blade is wider than the sensor, both sides of the blade never come into view at the same time; however, if the blade is thinner than the sensor, both sides of the blade are visible from different points along the sensor aperture. Figure 31 illustrates this phenomenon.

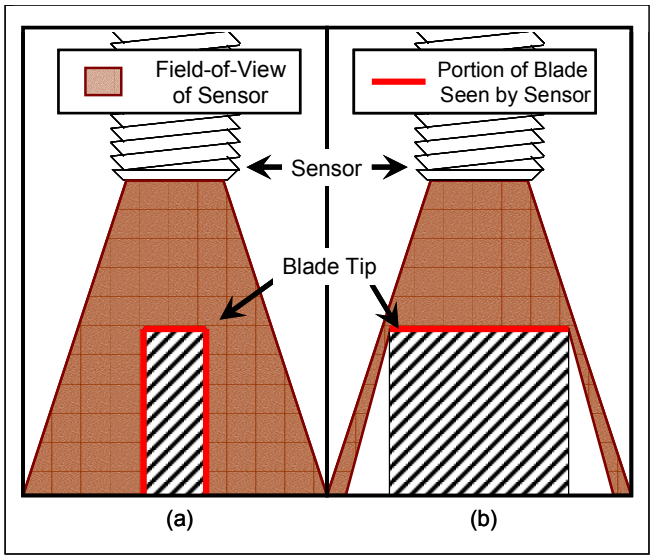

Figure 31. In the case in which blade width is less than the aperture of the sensor (a), there is a point at which the sensor sees both sides of the blade, but if the blade is wider than the sensor aperture (b), the sensor never sees both sides at once.

Since spatial filtering is caused by averaging measurements over the field of view, the portion of the blade in view is significant in changing the measurement from the ideal. If the blade is sufficiently large compared to the portion within the field of view, the effect of spatial filtering tends towards nothing as the blade gets larger. This is

because the measurement is closer to being a point measurement relative to the size of the blade. As blade width is reduced relative to the size of the sensor, the effect of spatial filtering increases since the portion of the blade in the FOV increases as the blade gets smaller and the sensor can see more of it at the same time. Also, as the width is reduced, the ratio of the visible area of the sides to the visible area of the tip increases. These differing measurements are averaged together, and the net effect is blurring from the ideal measurement. Thus, the blade appears rounder and less defined.

Turbine engine blade widths typically are within the range of 1.3 to 19.1 mm (0.050 to 0.750 in.). The sensor aperture in these experiments is 10.2 mm (0.402 in.) in diameter, so the experimental range of blades includes widths larger and smaller than the sensor aperture. Experiments are run using blade widths of 2.54, 6.35, and 12.7 mm (0.100, 0.250, and 0.500 in.).

Another consideration in relation to blade widths is the effect of the blade on the antenna pattern of the microwave sensor. According to electromagnetic theory, a larger blade affects the antenna radiation pattern more than a smaller blade because it blocks more of the microwave propagation and has a greater effect on the electromagnetic fields around the antenna. This may result in unusual measurement characteristics and inaccurate tip measurements.

One advantage in turbine monitoring is that blade widths do not significantly vary within a given stage of the engine, so the effect is similar across all measurements in the stage. Thermal expansion may cause some variation in width during normal operation but this change is less than 2% of the width for typical turbine blade materials. Testing this input factor defines the sensor's capability to measure all different widths of turbine

blades in different installations consistently without calibrating to individual blade geometries.

Blade Twist

The twist of the blade is defined to be the angle along the blade tip relative to the axis of the turbine. Figure 32 illustrates this parameter.

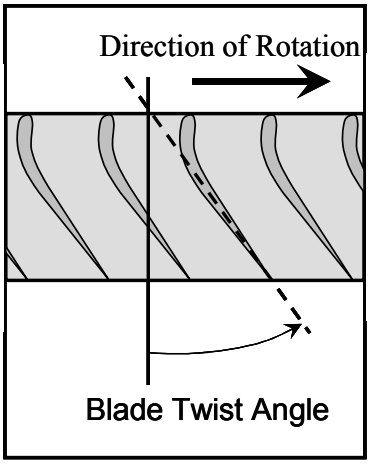

Figure 32. A side-view of a single stage of a turbine illustrates the blade twist factor. Blade twist is the angle of the tip relative to the turbine's main axis.

The blade twist greatly affects the geometry of the measurement situation, although in normal operation, it is a relatively stable variable. In an actual turbine, vibrations can cause twist in the blade, but it is not likely that twist on this level is detectable, since it is probably much less that one degree. However, different blade geometries have significantly differing natural blade twists, so it is helpful to understand the effect of this parameter; two levels of 0° and 45° give a qualitative understanding of this.

Blade twist affects sensor measurements mainly by changing the length of time during which the blade is in front of the sensor. Thus, a twisted blade appears wider than a non-twisted blade. This is because the line that the sensor traces across the blade is longer when diagonal than straight. Figure 33 shows both a non-twisted and twisted blade passing by the sensor aperture. The twisted blade is in the sensor's FOV for a longer period of time.

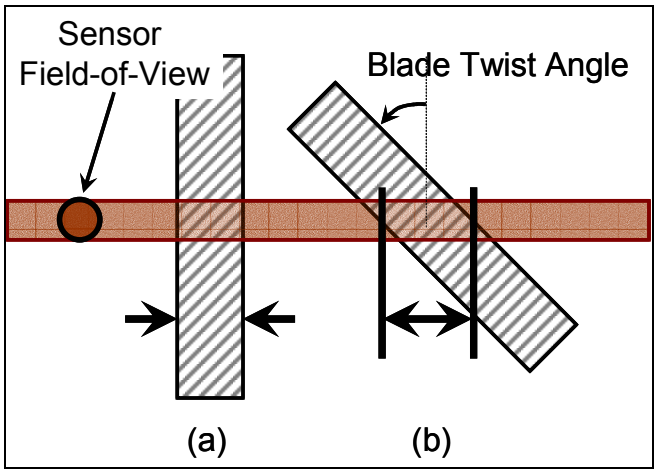

Figure 33. The sensor traces a longer line across the blade when the blade is twisted (b) than otherwise (a).

Blade Tilt

Blade tilt is the angle of the radial axis of the blade relative to a perfect radial of the disk along the main axis of the turbine. Figure 34 illustrates blade tilt. Blade tilt changes in a turbine when the blade begins to rotate in the axial plane, coming out of its seating in the disk. To this point in turbine development and monitoring, almost no analysis has been done on this type of vibrations in turbine. It is assumed to be a

miniscule effect, but it is important to vary this parameter in order to have a complete understanding of turbine operation.

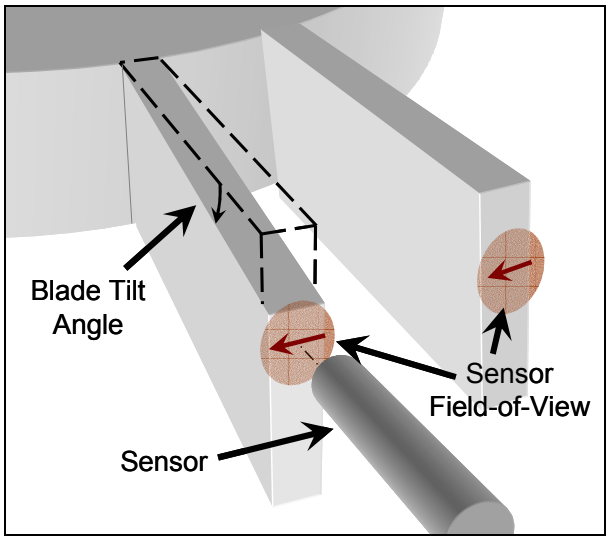

Figure 34. Illustration of blade tilt angle. The sensor measures a cross-section of the tilted blade (left) much closer to the top edge than that of the straight blade (right)—near the middle of the blade.

Tilt causes three changes in the measurement geometry: First, depending on where the axis of rotation is about which the blade is tilting, the cross-section of the blade may be closer or farther from the sensor; this is seen as a change in clearance in the blade measurement. Second, tilt may cause a slightly different cross-section of the blade to be scanned by the sensor as the blade turns past; a different cross-section may have a different shape. Third, the tilt causes a change in the angle of incidence of the microwaves with the surface. As the angle of incidence increases away from perpendicular, less of the microwave energy is reflected back to the antenna, and the overall blade tip RCS is reduced. Figure 34 illustrates microwave measurements with and without blade tilt.

Blade tilt cannot occur to a high degree in a turbine during normal operation. Most likely, only during rapid speed-cycling of the turbine, when centrifugal forces vary quickly and significantly does any tilt occur. Blade tilt may also occur when a disk begins to crack and the seating of a blade begins to open. A tilt of 3° or less would cause the blade tip to rub against the casing in most turbines; any higher angle of tilt would cause failure. This is why 0° and 3° are used for this experiment.

Approach Angle

The term approach angle or sweep angle is given to the parameter illustrated in Figure 35. Nominally, when a blade passes by the sensor, it is perfectly perpendicular to the sensor; however, vibrations bend the blade back and forth in the direction of travel causing a change in the sweep angle. This is called the approach angle, since it describes the angle of the blade as it approaches the sensor. In some turbine disks, blades are purposefully given a positive approach angle for aerodynamic and structural reasons.

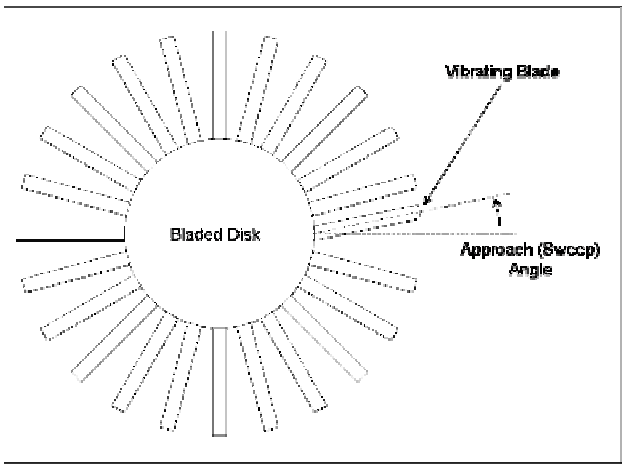

Figure 35. The approach (sweep) angle is the angle of the blades relative to a perfect radial; vibrations may cause this variation or some turbine disks are designed with blades purposefully swept.

The approach angle is closely tied to time-of-arrival measurements since the blades bending in this fashion is the source of deviation from perfectly spaced blades. The affect of this angle on the measurement with the microwave sensor is that the approaching and the retreating surfaces are viewed differently. Also, the angle of incidence of the microwaves reflected off the tip of the blade changes. The difference between the approaching blade and retreating blade may be noted as a difference in the measured rising and falling profiles. The changed angle of incidence causes a reduction in the RCS of the blade peak. Blade tip RCS is normally highest when the approach angle is 0°—directly along the sensor axis. This angle does not change much in normal turbine operation, depending on the length and material properties of the blades; hence, the angles of 0° and 3° are used for experimentation to note whether or not small angle changes have significant influence on measurements.

CHAPTER 8 DESIGN OF EXPERIMENTS RESULTS AND DISCUSSION

As described in Chapter 7, a five-factor, full-factorial design of experiments was performed to analyze the influence of factors on the turbine blade measurement using the microwave sensor. The DOE consisted of 216 experiments with four repetitions of each. An experiment consisted of a full setup of the experimental variables, after which the blade was passed in front of the sensor and data were taken in synchronization with the encoder counts of the rotary encoder. Thus, the relative motion of the blade was known exactly.

A LabVIEW data analysis interface was developed to extract the important information from each blade pass. The program was written to read Inphase and Quadrature data from the two channels on the DAQ control box, calculate the DC center of each waveform, calculate the relative phase at each encoder step, and process the displacement waveform. These data are calculated as discussed earlier in Chapter 7.

The data collected from the 864 blade passes was then used in a DOE analysis, focusing on the use of a general linear model ANOVA approach, and specifically the F-Test as a decision rule for certainty of a linear relationship between the factors of the DOE and the response data collected. The object was to determine if spatial filtering, while present and noticeable, invalidates the value of the measurements taken by the sensor.

General Linear Model ANOVA Approach and the F Test for Significance

Mathematical Background and Important Statistical Results

The general linear model used is the normal error regression model:

$$Y_i = \beta_0 + \beta_1 X_i + \varepsilon_i , \tag{20}$$

where X_i are the known inputs to the system, Y_i are the responses, and β_0 and β_1 are parameters relating the two linearly. The ε_i's are the error for each response to the system; these errors are called residuals. The system comes from the linear Equation (21):

$$y = m \cdot x + b . \tag{21}$$

Equation (20) is designed to test for a linear association between Y and X. If the system were perfectly linear, the error would follow very nearly a normal distribution across the regression line described by the parameters β_0 and β_1. A decision rule is used to test the hypothesis

$$\begin{aligned} H_0 &: \beta_1 = 0 \\ H_a &: \beta_1 \neq 0 . \end{aligned} \tag{22}$$

The null hypothesis describes the case where there is no linear association between Y and X and thus the system is best accounted for if the linear parameter β_1 is not used in the system. The alternate hypothesis being true would indicate that there is a value of β_1 for which the system fits well with the linear model and the error is close to normally distributed across the regression.

The analysis of variance (ANOVA) approach to testing the model describes the variance of the system in response to input variables. Using this approach, experiments

with like factors are grouped and the variance from the model is quantified with respect to each factor. The total variance is the aggregate of the variances due to the individual factors. To test the significance of each factor in the DOE upon each response variable, the F* statistic is used. The F* statistic follows the F probability distribution, and is calculated in the ANOVA analysis by (23).

$$F^* = \frac{\text{MSR}}{\text{MSE}}, \tag{23}$$

where MSR is the regression mean square, and MSE is the mean squared error from the model. The F distribution is used for the variance of a system with a certain number of degrees of freedom. Each factor has two or three degrees of freedom depending on the number of levels in the DOE, and the response variables have some number below but close to the total number of data points (864 individual blade passes). The F* statistic is used as a decision rule in the following way: if

$$F^* \le F\left(1-\alpha; df_{\text{factor}}, df_{\text{data}}\right), \tag{24}$$

where df_{factor} and df_{data} are the degrees of freedom of the input factor and response data respectively, H_0 is conclusive by the significance level, 1-α. This means that $\beta_1 = 0$ best describes the system, and hence there is no significant linear relationship between the two factors in question. On the other hand, if

$$F^* \ge F\left(1-\alpha; df_{\text{factor}}, df_{\text{data}}\right), \tag{25}$$

then H_a is concluded and there is a significant linear relationship between the factor and the response. The value α is the probability value for the opposite conclusion being true. The F* statistic for each factor is not directly comparable since the F* statistic is based on the degrees of freedom of each individual input factor, and not all of the input factors

have the same number of degrees of freedom (i.e. they have different numbers of response levels). For direct comparison, the F* statistic translates into a confidence in the linear relationship based on the degrees of freedom. The confidence is given by Equation (26):

$$C_i = (1-\alpha)\cdot 100\% \quad (26)$$

Another statistic that is noteworthy in this analysis is the r-squared value. This value is known as the coefficient of determination. It is a value between zero and one quantifying the percent reduction of the variation if some factor, X, is considered. A value of $r^2=1$ says that the variation in a system response is completely determined by the factor being analyzed; the correlation is perfect. In the case of this DOE, the five input factors are not the only variables in the actual system setup, so the r-squared value is lower than one. However, it is still an indication of the ability of the theoretical model to adequately describe reality.

Important Resulting Plots from the ANOVA Approach

There are two important plots that come from the ANOVA approach in this DOE. The first plot graphically presents the effects of each input factor on a given response and the second shows the the characteristics of the residual errors—the quality of the ANOVA. The first plot is called a main effects plot. An example main effects plot is shown in Figure 36.

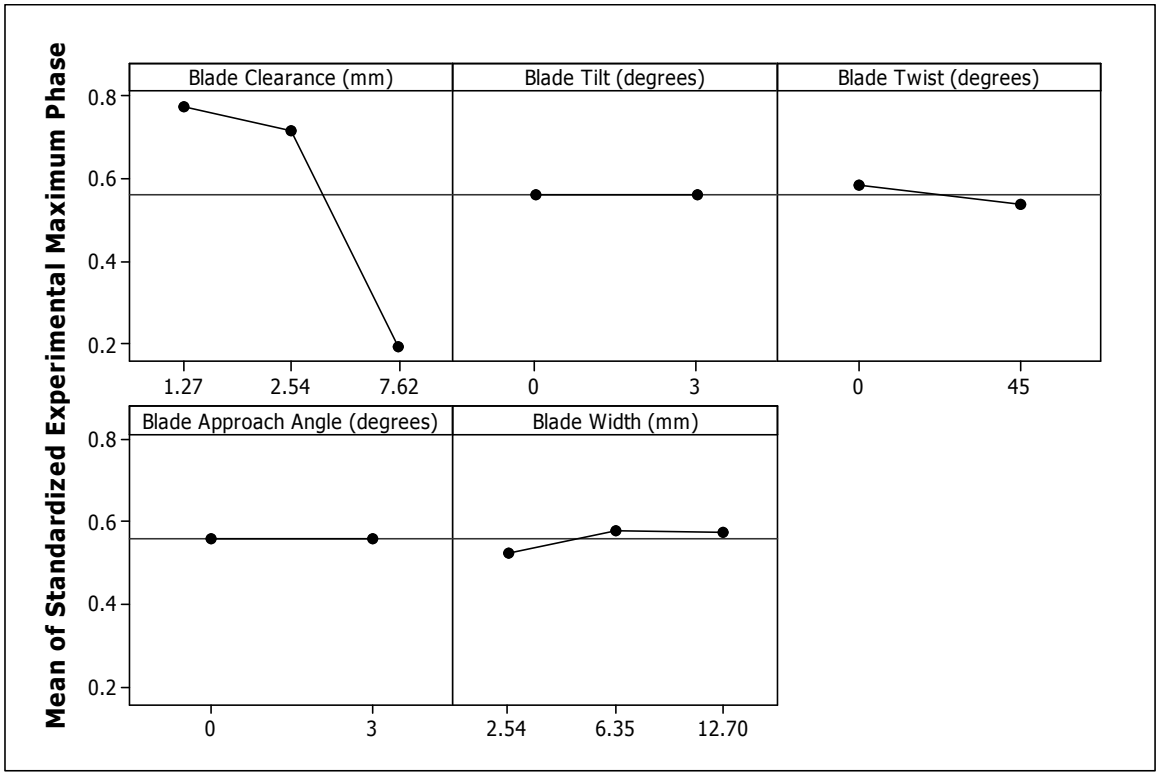

Figure 36. A sample main effects plot.

The main effects plot graphically shows the influence of each of the individual input factors on a single response. The main effects plot in Figure 36 shows the influence of each of the DOE input factors on maximum experimental phase response. This plot shows the averages of the data sets at each level of the input factor. For each separate graph, the mean response at each input factor level is plotted so trends may be easily seen. In this example, it is easy to see in the first graph that as clearance increases, the maximum phase response decreases. The main effects plot graphically shows the relative strength of the influence of each of the factors because the response scale is the same for each graph. In this example, influence of approach angle and tilt is unnoticeable relative to the influence of clearance.

The second important graphic is a series of graphs showing the distribution of residuals in the data. These residuals are the differences between the actual data and the means that are plotted on the main effects plots. Figure 37 shows a sample of this type of graphic.

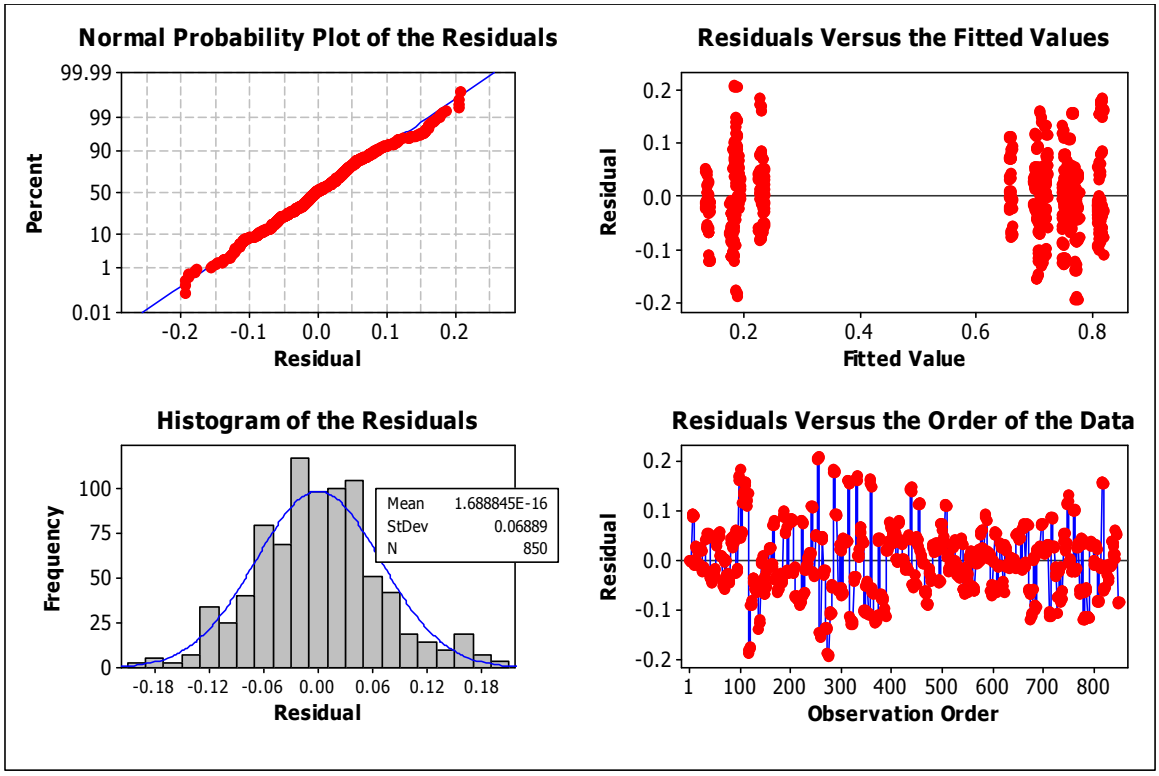

Figure 37. A sample of the residuals plots.

The two graphs to the left describe the distribution of the residuals. In most systems, the residuals ideally are normally distributed about the mean. If the residuals are normally distributed, the residual error is essentially random about the mean: there is little or no systematic error. Systematic error is seen in a system when the theoretical model is not adequate to describe the actual occurrence. If the residuals are normally

distributed, the top-left graph will show a straight line along the diagonal reference line. It says that 50% of the residuals are below the mean of the overall data set, and the residuals are then equally distributed on either side. The bottom-left graph is a histogram of the residuals. The reference line on this graph is a normal distribution that is fit to the residuals—the mean and standard distribution of the normal distribution is inlaid along with the number of residuals, N, in the data set.

The graph in the upper-right tells of the distribution of the residuals as a function of the fitted values resulting from the ANOVA method. A set of data that is well-described by the ANOVA fits will not show any clear trend in relation to the fitted values. The data in the example shows such a case.

The last graph is also useful for detecting systematic error in the test setup. This plot shows the residuals as a function of the order of experiments. The example data is fairly consistent about the mean as a function of the order of experiments. Any clear trends in this graph may indicate a change in the test setup since the DOE experimental order is randomized. If the experimental order were not randomized, trends would be expected to appear in this graph as certain aspects of the test setup change one at a time in a systematic way.

Data Analysis and Discussion

Experimentally, the three main responses from the DOE show significant results: phase response, radar cross-section, and apparent blade width. Each of these is described in detail below. For ease of reporting, only the most significant results are emphasized here. A full set of the ANOVA results may be found in Appendix A for reference.

Phase Response

For the purposes of this analysis, the phase response of the system is the point of maximum phase of a blade pass. Refer to Chapter 7 for a full description of this datum including the expected result. The first important result of the DOE is seen in the residuals graphic of the phase response ANOVA. The four plots of residuals are shown in Figure 38.

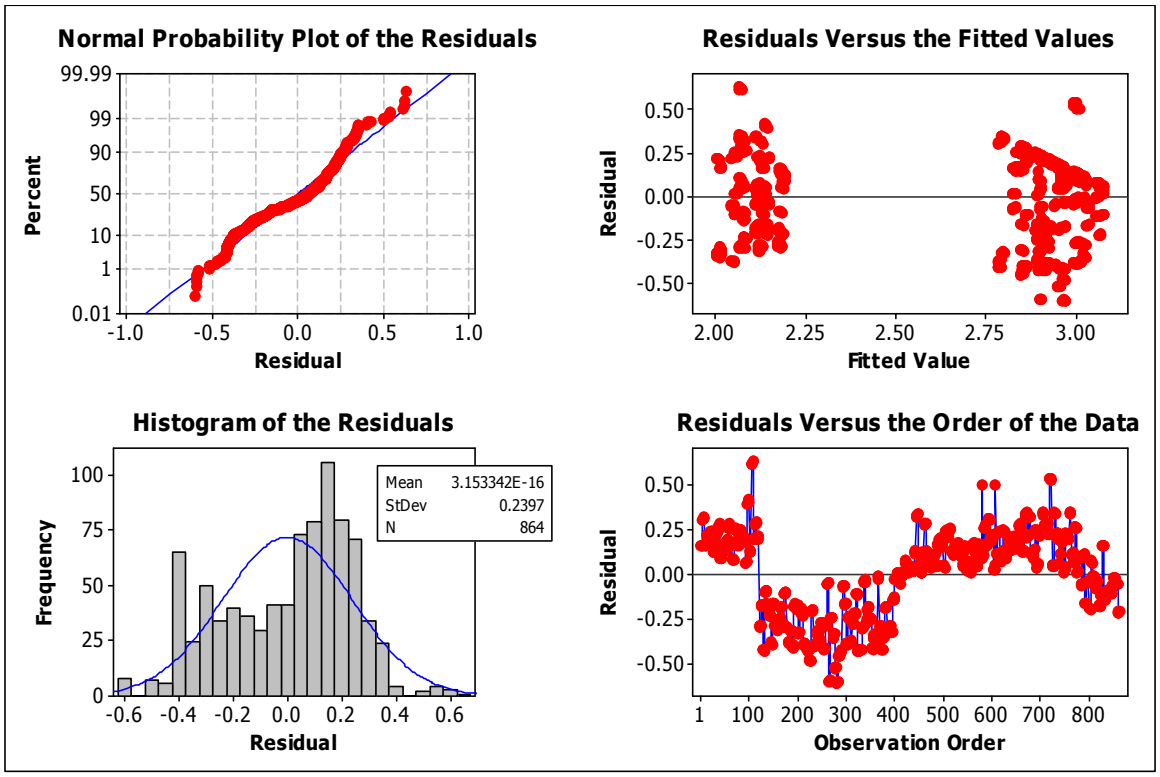

Figure 38. Four plots of the residuals of the DOE phase responses show trends in the errors—especially clear in the residuals vs. observation (experimentation) order.

It is instructive to note the trend clearly visible in the residuals of phase versus observation order plot. This plot shows the residuals oscillating about the mean throughout the experiment; also, there are discrete jumps in the data near observation 120

and 396. These happen to coincide with time breaks in the experimentation by the author. Further, the continuous trend coincides closely with the temperature in the lab during measurements—the temperature rises a number of degrees during the night when the building air-conditioning is suspended. The experimentation was performed as follows (refer to Figure 39): The first 120 experiments were performed late at night, and then the author took a break until the next morning. Experiments were run through to that afternoon until a run 396 at about 1:30PM; later that day, the air-conditioning was turned off and the temperature began to rise. The experiments were continued at about 9PM and were run through the night and into the morning when the air was again turned on and the temperature of the room returned to the day-time setting. Comparing this time data to the residuals above reveals a remarkable correlation.

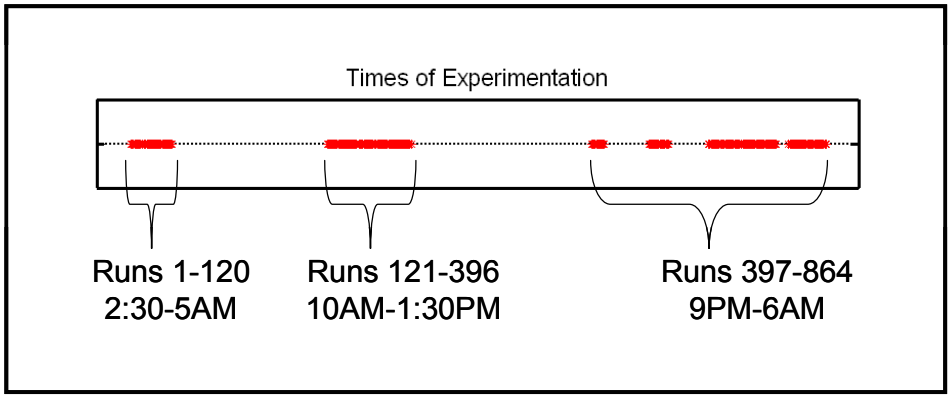

Figure 39. The experiments were run over a two-day period, and a trend in the data closely follows the time of day because of the automatic building air-conditioning.

The effect of this trend, though important, is not altogether detrimental to the DOE. Temperature affects many things in the system, but most notably the length of the microwave cable and the frequency of the VCO (voltage-controlled oscillator). The

microwave cable changing length even a few micrometers affects the overall distance traveled by the microwaves and thus the phase response of the system. The VCO also fluctuates with temperature, changing the frequency of emitted microwaves, and thus making the wavelength different; since distance measurements are directly dependent on the transmit wavelength, this change alters the measurement if it is not accounted for. For the purpose of the DOE, however, this data is still valid since the fluctuation is slow and the order of experiments is randomized by the experimental factors. Hence, the phase change affects all different factors relatively equally and the running average reflects the influence of the temperature trend. It affects the residuals, as can be seen, spreading them out from the normal distribution and causing the linear fits of factors to be less certain; therefore, the r^2 value decreases.

For the sake of processing this data more accurately, the temperature drift is removed by subtracting out the phase of this slow trend from each data point; this is similar to a high-pass filter in traditional signal processing. A trend-line was created for the data by taking a simple running average and the amount of the trend-line for each experiment was then removed from the original data as shown in Figure 40.

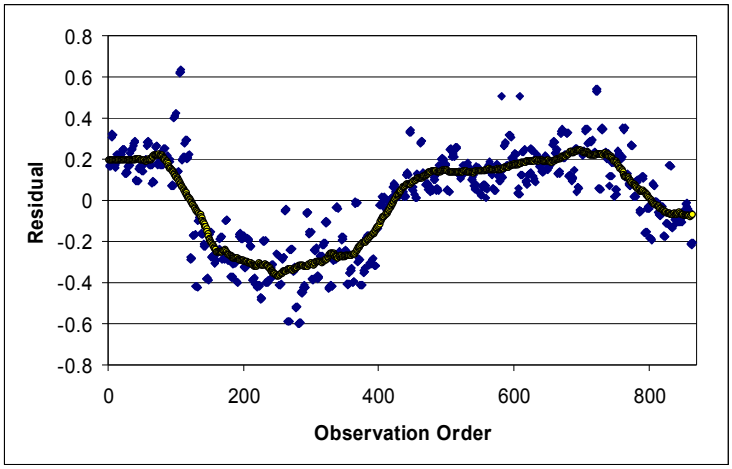

Figure 40. A trend-line was calculated from the residuals of the phase response ANOVA. This trend, reflecting the influence of temperature, was removed for analysis.

The resulting residuals graphic is shown in Figure 41. Note that the residual histogram is much closer to a normal distribution and the observation order plot no longer shows any of the temperature oscillation. Now, the data is fit very well by the ANOVA calculations and the main effects plot is more useful for describing the actual trends in the data.

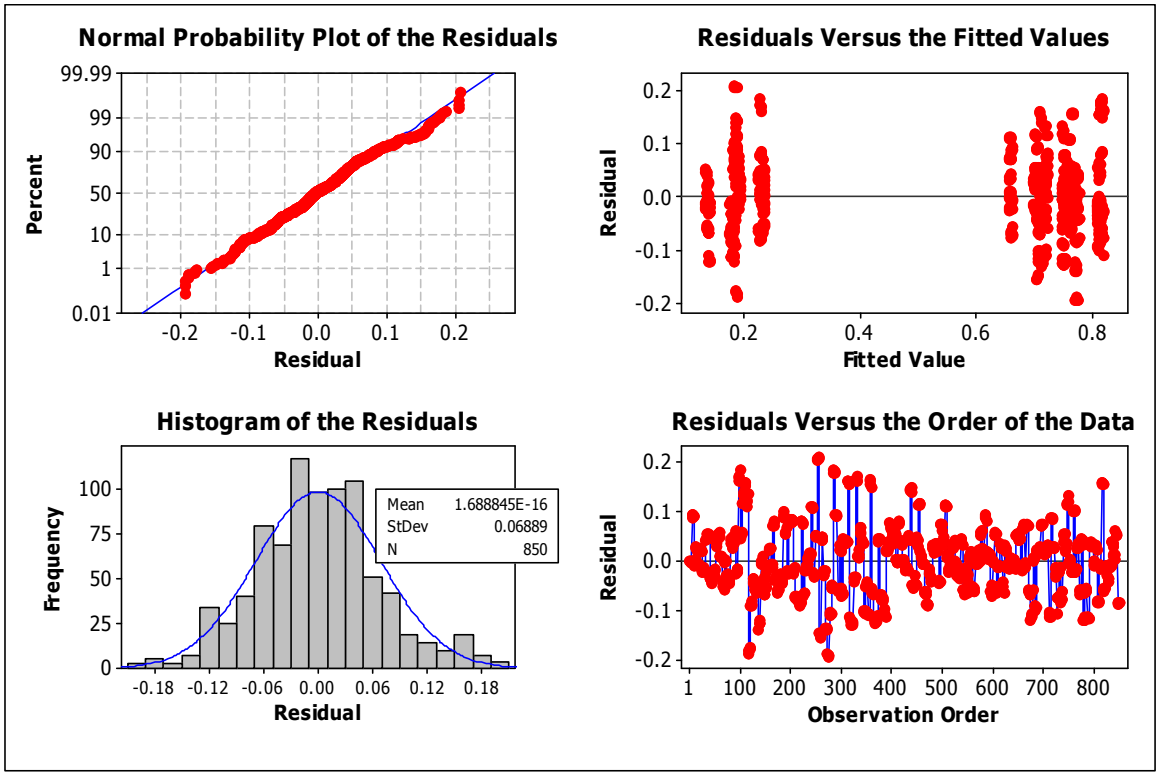

Figure 41. The residual plots of the phase response in the DOE with the temperature drift removed.

The main effects plot for maximum phase response to the given input factors is shown in Figure 42. This figure plots the mean maximum phase value over all of the experiments in the DOE for each level of the factorial design. Thus, the first graph shows the mean value of phase for all of the experiments run at 1.27 mm (0.0500 in.) clearance, then at 2.54 mm (0.100 in.) clearance, and finally at 7.62 mm (0.300 in.) clearance.

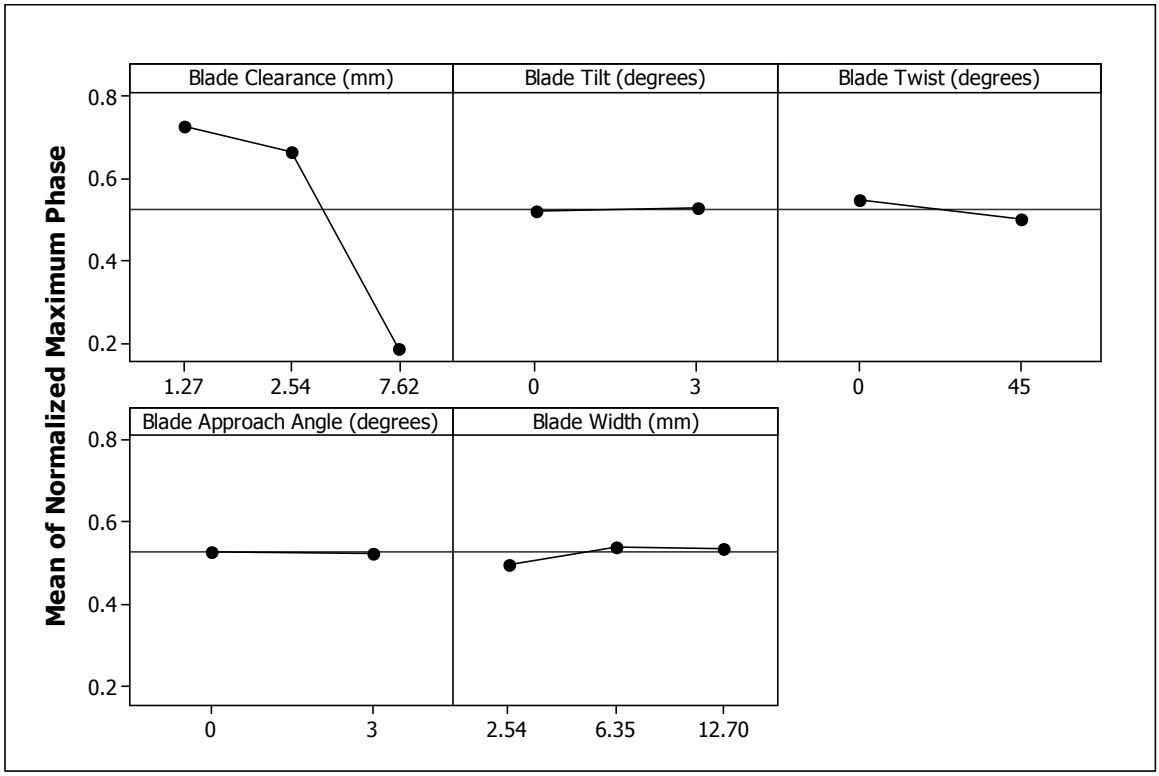

Figure 42. The main effects plot for the phase response of the system to each of the five input factors in the DOE.

Clearly, the main influencer of phase response is the clearance of the blade relative to the sensor, as is expected. The phase of the sensor measurement should directly and linearly correlate with the clearance proportionally to the wavelength of the transmitted electromagnetic wave used. Refer to Equation (6) for this calculation. Note that the x-scale of the plot is the three levels of the DOE and not linear clearance; thus the slope does not appear linear as it actually is.

Ideally, none of the other factors will affect the phase response of the sensor. However, that is not precisely the case. Of the other factors, twist and blade width both have some noticeable effect on the phase measurement; both influence the phase response

by 7% and 9% of the influence of clearance respectively. Figure 43 shows the percent change caused by each factor.

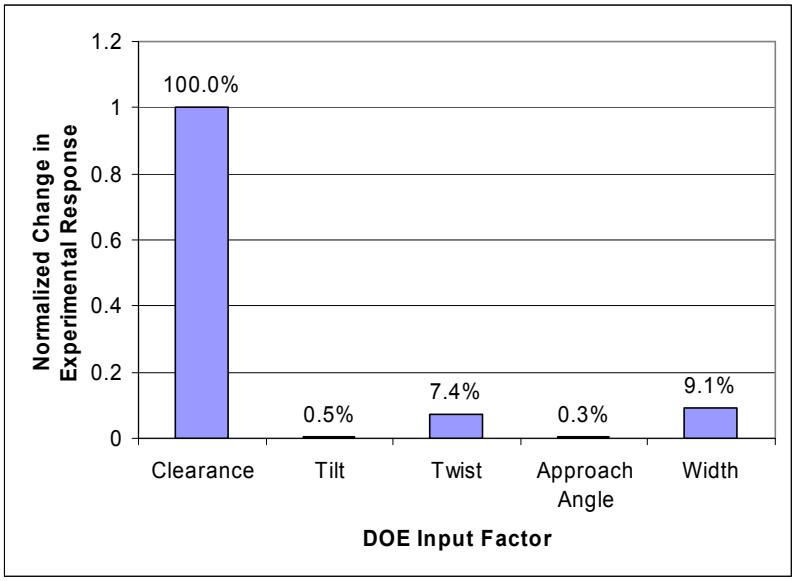

Figure 43. A plot of the percent change in phase response induced by each of the varying input factors.

The F* statistic quantifies the significance of these factors. Table 2 holds the F statistics and p-values for the linear regression analysis of phase response with respect to the five factors of the DOE with the temperature drift removed. Given here as an example, since the F* statistic is not directly comparable, it is omitted for the rest of the results. However, the full ANOVA table for each factor is reported in Appendix A for reference.

Table 2. Important Factors from the ANOVA table of phase response to the factors of the DOE.

Factor	F* Statistic	C_i	r^2
Blade Clearance	6070.67	100.%	93.6%
Blade Tilt	0.26	39.1%	
Blade Twist	81.29	100.%	
Blade Approach Angle	0.16	31.1%	
Blade Width	50.40	100.%	

From this analysis, blade tilt and approach angle show no significant effect on phase of the measurement. Also, while the influence of clearance is much greater, it can be said with great confidence that twist and width also show some linear relationship with phase response. Over the range considered by the DOE, a 45° change in twist angle influenced maximum phase response 7.4% as much as the change in blade clearance of 6.35 mm (0.250 in.). Measurement geometry and spatial filtering cause this effect. As discussed earlier, the twist of the blade affects the measurement in a number of ways. Primarily, more of the blade tip is contained in the FOV of the sensor when there is a greater twist. It is expected that the spatial filtering causes less error as more of the tip is measured at the same moment, as in the case of the twisted blade. Also, as the blade is twisted, the ideal measurement changes because the profile of the twisted blade is wider than that of an untwisted blade. Both of these may explain the variation in phase response due to blade twist.

However, this factor as tested in the DOE is not a typical variation experienced in a turbine—there is no point at which the turbine blade twists a full 45° from its initial twist angle except during a failure. Rather, twist changes during operation are small—less than a few degrees. This factor is designed to measure the effect of different blade

geometries altogether; it answers the question: Is the response of the sensor consistent if installed in any turbine without a calibration of sorts? Based on these results, the answer is no. A certain phase offset may influence measurements for each blade geometry. However, the relative measurements within a single turbine stage are still accurate. Only further study will conclude whether or not small changes in twist are enough to affect the maximum phase of the measurement profile noticeably. This is important to consider in the future since blade untwist is a common phenomenon in turbine wear. Blade untwist occurs when a turbine blade begins to lose its natural twist because of the forces of operation. If the untwist is significant, it may have an influence on the blade tip measurement. From this analysis, assuming the affect of spatial filtering is linear between 0° and 45° twist, a 5° untwist changes the phase response by less than 1% of the change caused by blade clearance, so measurements are expected to be valid. For example, relative clearance measurements over a range of 7.62 mm (0.300 in.) of a certain blade geometry are accurate to within 76.2 μm (0.003 in.) even with a varying 0° to 5° blade untwist.

Blade width is the second significantly influential input factor on phase response. It is another factor that does not vary greatly during turbine operation. Only a different blade type is significantly different to cause a change in the phase response of the measurement. The change in width is 3.81 mm (0.150 in) for the first step and 6.35 mm (0.250 in.) for the second step up to the 12.7 mm (0.500 in.) blade. Even these large changes in blade width only result in 9.1% of the change that blade clearance causes. The actual variation from blade to blade in a single turbine disk is determined by the precision of the manufacturing process, which has tolerances such that these variations

are undetectable to this sensor. Hence measurements are expected to be robust to all of the blades on the same disk. Like blade twist, though, a different disk or turbine may be significantly different, so this needs to be considered as well. Further study may reveal whether or not this affect is linear with increasing widths. If so, measurements may be calibrated to each turbine stage by manually inputting a constant blade width and adjusting based on the linear characterization, similar to the offset caused by blade angle.

The other factors—blade tilt and approach angle—both indicate very small linear relationships with the phase response of the system. The F* statistic shows that these variations are much smaller than the noise in the data, so they should not be trusted as conclusive. Moreover, even if it were significant compared to noise, the change caused by a 3° change in blade tilt is only 0.5% the change caused by blade clearance, and the change caused by a 3° variation in approach angle is less than 0.3%. It is desirable to have such small influence since these two factors will certainly change due to vibrations in an operational turbine. The range tested reflects the greatest variation expected in actual turbine operation. Smaller variations have even less effect, so it may be concluded that the measurements are not significantly altered by spatial filtering changes caused by tilt or approach angle.

Blade Width Response

The response of blade width is the most direct measure of spatial filtering since it provides a quantity describing the blurring of the blade. Most blade pass measurements produce a phase profile resembling a parabola; spatial filtering causes this deviation from the ideal measurement of a blade. The intensity of the spatial filtering effect may be tied to the width of this parabola, since the more a target is blurred, the wider the parabola

becomes with respect to the actual blade width. The hypothesis is that the effect of spatial filtering increases with clearance, and this is confirmed by the DOE data. This response is tested at three depths, but only the response of blade width at 1.27 mm (0.0500 in.) below the peak is shown here. However, the trends of other responses are similar.

Blade width is the most difficult data to gather from the DOE data set. This is because the effect of spatial filtering is so great in some cases that there does not exist a point 5.08, 2.54, or 1.27 mm (0.200, 0.100, or 0.0500 in.) down from the peak. The peak may be only rise 1.0 mm (0.040 in.) out of the phase noise at the DC center. Thus the blade width measurements taken by the processing program come from the surrounding noise and do not accurately reflect the experimental data. These data points show up very clearly in the residual plots as outliers. For this reason the number of outliers increases as one progresses to the 2.54 and 5.08 mm (0.100 and 0.200 in.) depth blade width statistics. For the sake of accuracy, these outliers are removed. The residuals graphic of the 1.27 mm (0.0500 in.) depth blade width response is shown in Figure 44.

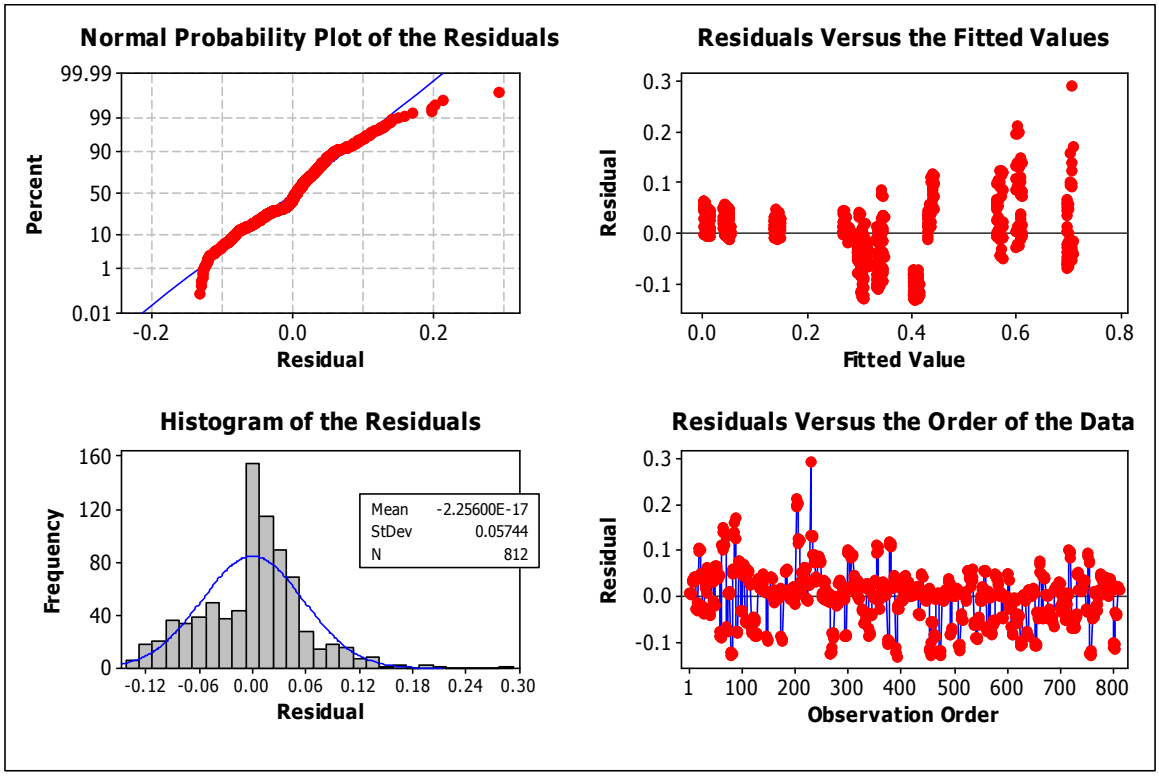

Figure 44. The residuals plots of the 1.27 mm (0.0500 in.) blade width response. Outliers have been removed for accuracy of data processing.

In this figure, the histogram of the residuals shows non-normal behavior. A large number of residuals are on the positive side of the mean, while few are on the negative side. This is likely because of the data processing. Rather than interpolating the width at some depth, the measurement of apparent width is made from the first data point below that depth. This means that all of the processed widths are rounded up to the next integer value of data points. Figure 45 illustrates this processing technique. This is the reason for the greater number of positive residuals than negative ones—especially near the mean where data is the most accurate.

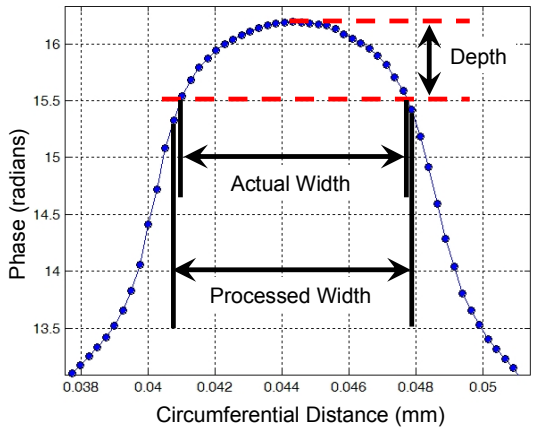

Figure 45. The processed width is likely to be slightly larger than the actual width at some depth since the data processor does not interpolate between points.

The main effects plot in Figure 46 shows that blade width clearly affects the measured width.

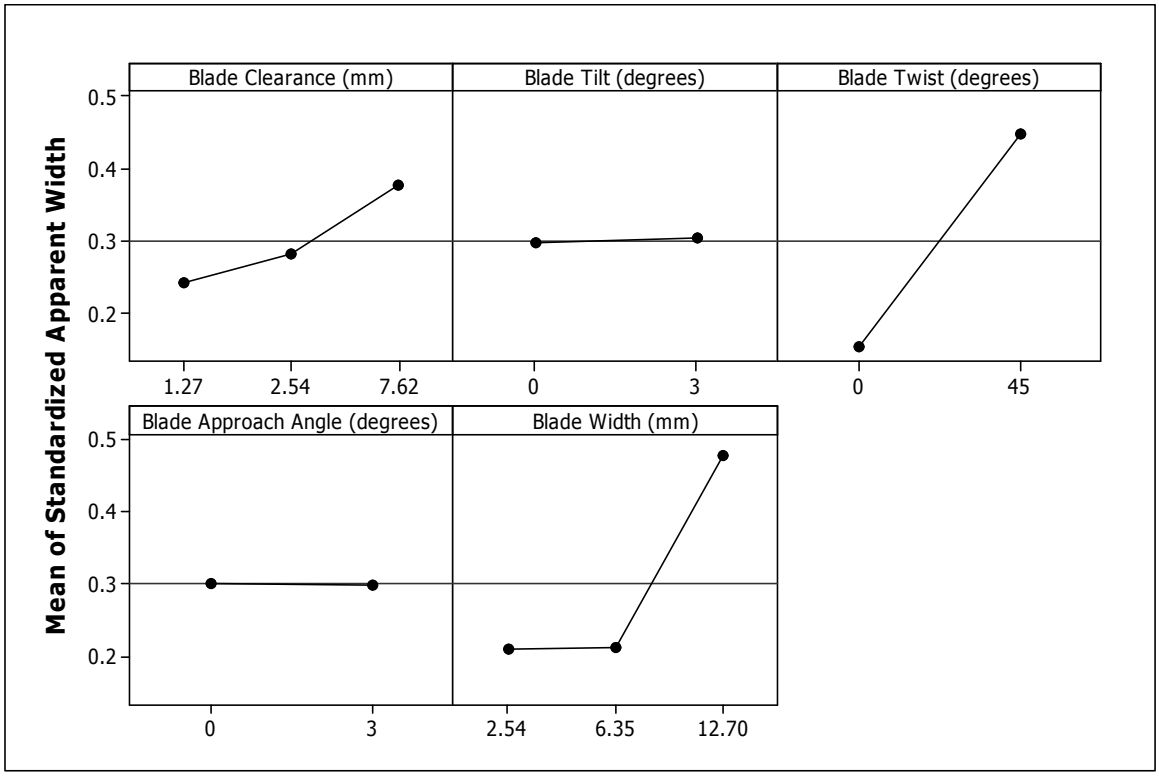

Figure 46. The main effects plot of the DOE factors influencing apparent blade width at 1.27 mm (0.0500 in.) depth.

Blade twist and width have the greatest influence on apparent width. It is intuitive that blade width has an affect on apparent width. However, the trend is not so intuitive. The main effects plot shows that there is very little increase in apparent width when the blade increases from 2.54 mm (0.100 in.) to 6.35 mm (0.25 in.). This effect is most likely caused by spatial filtering. There is a certain amount of blurring that is inherent in the sensor due to the size of the sensor aperture. As the blade gets thinner relative to the sensor, the influence of the sides on the final measurement increases. Eventually, the sides of the blade provide more of the aggregate RCS than the tip in certain measurement geometries, so the area of the side of the blade drives the measurement. This causes thin blades to appear to be the same width as slightly wider

blades. As the blade approaches the size of the sensor aperture, the sides have less influence when the blade is close in. This spatial filtering effect is seen only at the very tip of the blade. As the metric gets wider, the measurements becomes more linear and then actually reverses in trend. Figure 47 shows this.

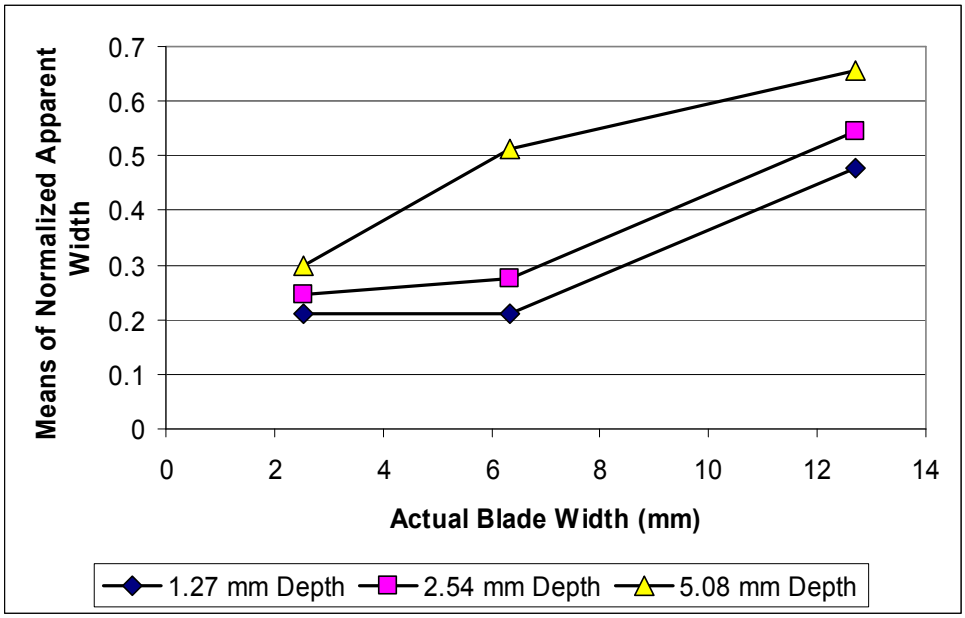

Figure 47. Apparent blade width measurements for each of the three measurement depths.

The blade width response is also influenced greatly by clearance; the reason for this is spatial filtering as well. As explained earlier, with increased clearance, the range of the blade surface within the sensor FOV increases. This causes the blade to be more blurred, and the width metrics confirm this trend.

Referring back to Figure 46 once again, the greatest single influence on apparent blade width is blade twist. However, this is not due to spatial filtering for the most part. Rather, the geometry of the measurement situation changes when the blade is twisted as

discussed in Chapter 4 above. The real profile is actually much wider for a blade that is twisted, and the data confirms this. The relative changes of apparent width are plotted for each measurement depth in Figure 48.

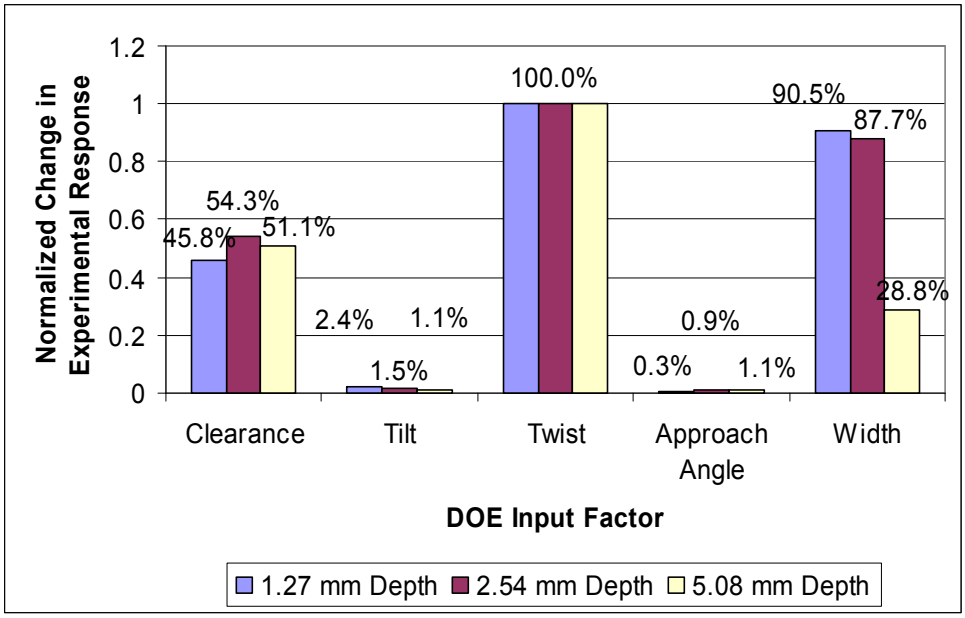

Figure 48. The relative percent changes in apparent blade width at three different depths due to the input factors of the DOE.

The large influence of blade twist on apparent blade width suggests a possible method for detecting changes in blade twist in turbine blade measurements. A large change in the measured apparent width of a blade without a large change in the measured phase response corresponds with a change in blade twist. This is the most significant result of the apparent width response.

The measurements taken here monitor a 45° change in twist, but real changes in-situ are much smaller. Further experimentation must be done to analyze this possibility, but it has the potential to provide vital information on the fatigue state of turbine blades

by providing in-process measurement of this factor. A turbine equipped with such a sensor system may accurately self-diagnose an unhealthy state of blade untwist and alert the crew of the problem.

The ANOVA statistics are shown in Table 3 for the 1.27 mm (0.0500 in.) blade width case.

Table 3. The ANOVA results of 1.27 mm (0.0500 in.) blade width response to the DOE variables.

Factor	C_i	r^2
Blade Clearance	100.%	92.6%
Blade Tilt	91.3%	
Blade Twist	100.%	
Blade Approach Angle	14.0%	
Blade Width	100.%	

All of the input factors, with the exception of approach angle, show a significant relationship with apparent blade width. However, just as in phase response, both tilt and approach angle influence apparent width very little—less than 3% for a 3° change. All of the other relationships discussed above are certainly significant. The ANOVA statistics for the other depths may be found in the appendix, but they are similar. In those cases, blade tilt is insignificant along with approach angle.

Radar Cross-Section Response

The ANOVA statistics for the response of maximum RCS are located in Table 4. These results suggest an intriguing possibility.

Table 4. The ANOVA results of maximum RCS response to the DOE variables shows that all of the factors have a certain linear relationship with RCS.

Factor	C_i	r^2
Blade Clearance	100.%	94.7%
Blade Tilt	100.%	
Blade Twist	100.%	
Blade Approach Angle	99.8%	
Blade Width	100.%	

Notably, all of the input factors have a significant influence on maximum RCS. Also, an r^2 value of 0.947 indicates that the linear fit of the ANOVA method is very good—the input factors explain most of the variation in the response in a linear fashion. Now, the main effects plot, shown in Figure 49, exhibits the level of influence of each factor relative to each other.

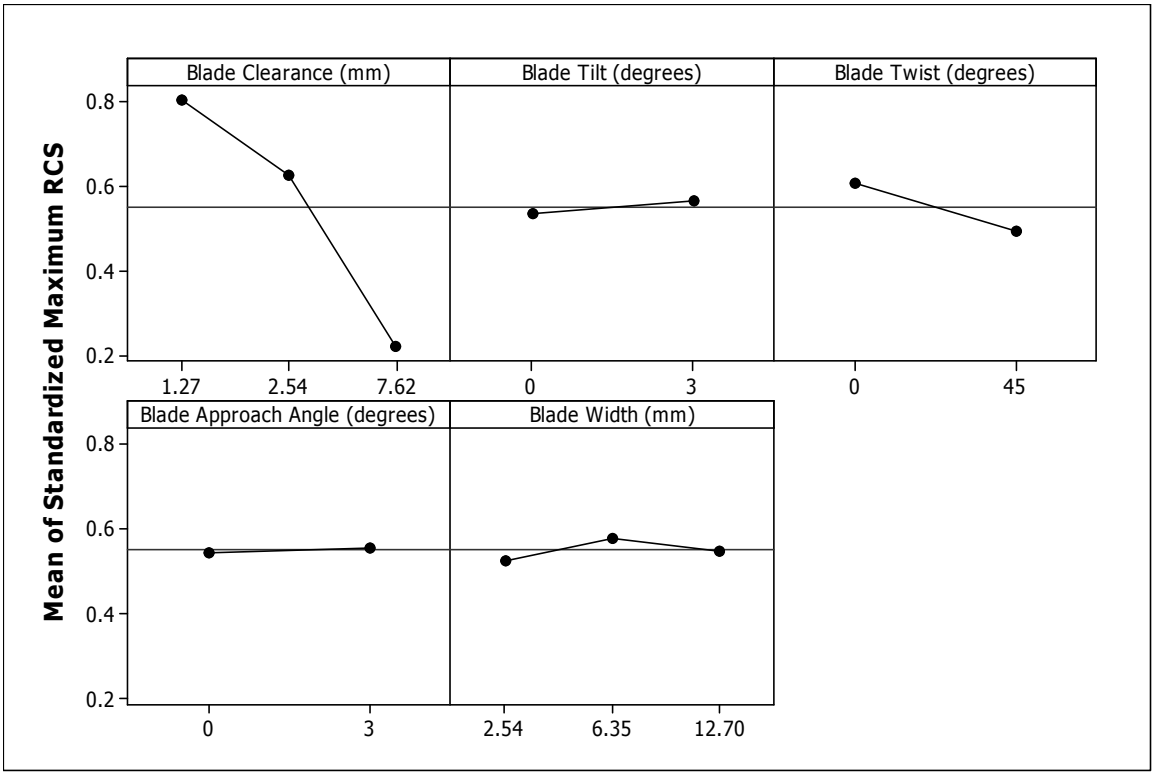

Figure 49. The main effects plot of DOE factors as they influence maximum RCS.

Again as expected, the greatest influence by a large margin over maximum RCS is blade clearance. This is caused by the attenuation of microwaves as they travel through free space to and from the blade. The F test gives approximately 100% confidence that some linear relationship exists between clearance and maximum RCS. This is inconsistent with the non-linear attenuation of microwaves as they travel through space.

The clear trend between RCS and clearance might suggest the possibility of using only the RCS of a measurement to determine clearance—especially since RCS is often easier to process than phase measurements. This method of measurement is similar to the method of measurement by capacitance and eddy current probes; both measure clearance indirectly by measuring the influence of blade passages on some other phenomenon—

electrical capacitance and the presence of eddy currents. But these data imply that a system using RCS as a blade clearance measurement would require careful calibration for each blade/casing geometry, as opposed to a phase measurement, which is based on the constant wavelength. Using a phase measurement allows one to put the sensor in any situation, obtain one calibration measurement to determine the absolute phase, and then all measurements are relative to that based on the known wavelength of microwaves. More importantly, the strong certainty of a linear relationship between RCS and the other factors of the DOE says that any changes in these other factors—blade width, twist, tilt, and approach angle—also affect the measurement of blade clearance derived from maximum RCS measurements. In a real turbine, all of these factors change slightly, so measurements are inaccurate in as much as they are influenced by these other input factors.

Twist and blade width have the next greatest effect on RCS measurement. Figure 50 shows the numerical value of these changes relative to clearance.

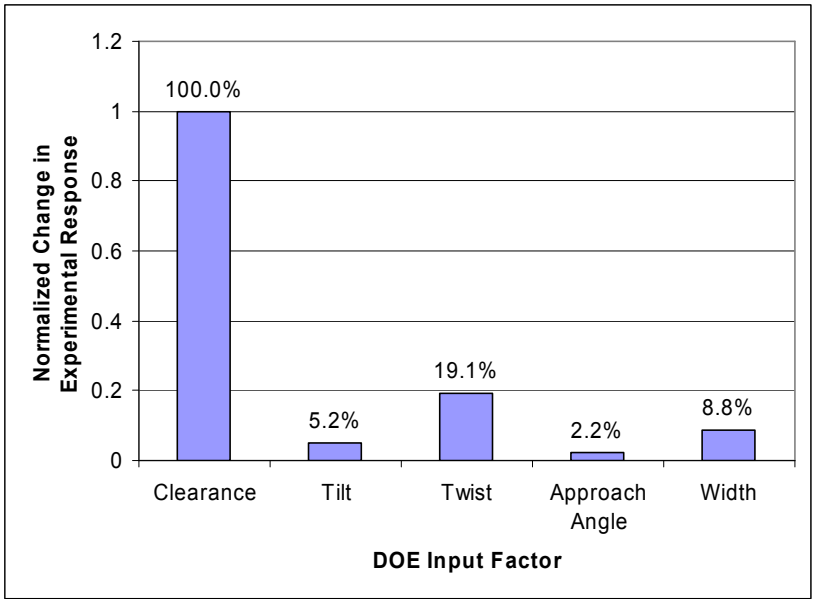

Figure 50. The relative influences of the DOE input factors on the maximum RCS measurement.

It may be seen that this effect is significant compared with the effect of clearance. However, as stated before, variations in twist and blade width never exist in these ranges in a turbine during operation. This means that these factors are not likely to affect the measurement of maximum RCS much. Scaling the relative change due to blade twist down to a value that is possible in actual turbines (less than 3°), a change of 1.3% of the change due to the clearance may be expected. The scaled change caused by variations in blade width is insignificant.

The tilt and approach angle factors both propose an interesting possibility for further study, since both affect the maximum RCS in a linear fashion with great confidence (almost 100% for both). Because neither of these factors produced a linear change in phase response but both do have some influence over RCS, the combination of these responses may be used to decouple changes in blade clearance from changes in tilt

and approach angle. For example, a reduction in maximum RCS without a change in peak phase measurement indicates that a blade has changed its tilt or approach angle while remaining at the same clearance. Spatial filtering causes all of the measurements to be blurred so that not much information can be obtained from the actual shape of the waveform, but the strength of the signal can be used to derive more information about in-process blade deformation and vibration than was previously available. It is likely that this change is only very slight and may require high signal quality and advanced signal processing to determine, but these results suggest the possibility strongly.

CHAPTER 9 COMPUTATIONAL MODEL RESULTS AND DISCUSSION

The same set of 216 experiments from the DOE was simulated with the computational model described in Chapter 6. Each experiment was run once, without repetition, since the only sources of noise in the computational model are calculation errors (rounding errors) and discretization errors (lack of density in the modeled meshes)—these are consistent over repetitions. The output of the model is a vector containing a magnitude and phase representing a reflection dependent on the measurement geometry; this is the same output as real sensor measurements. Therefore, data processing of the model measurements is the same as that of the physical experiments. The same three responses are analyzed for the effect of spatial filtering—the phase at the blade tip, the maximum RCS, and the apparent width of the blade.

Processing Model Data

Figure 51 shows a sample blade pass measurement set generated by the computational model next to an experimental blade pass. The model calculates measurements in polar coordinates (phase and magnitude), but for comparison to actual data, the set is displayed in Cartesian here.

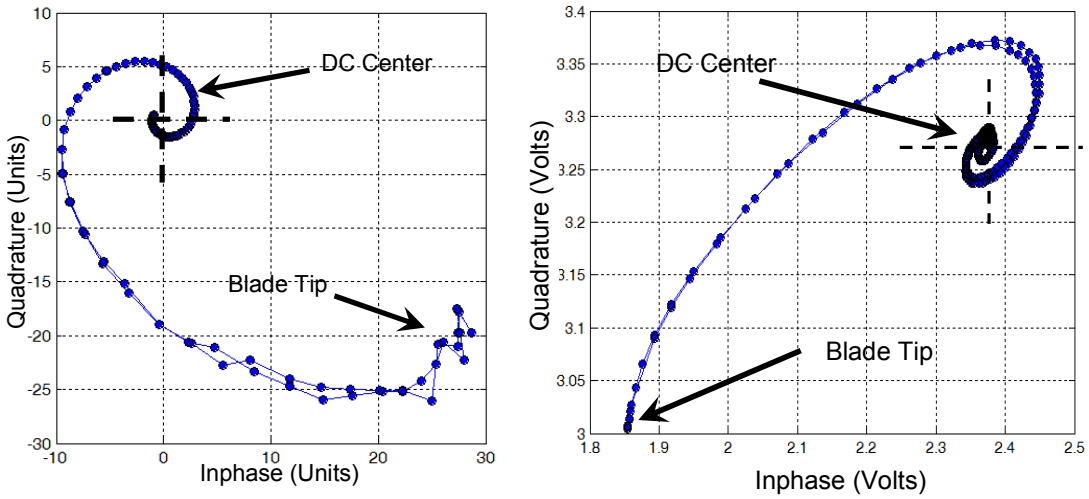

Figure 51. Inphase versus quadrature plots of blade passes as calculated by the computational model (left) and as recorded experimentally (right).

Model vector magnitudes are relative to each other and therefore have no units, but this is acceptable for analyzing data trends. Note that the shape generally follows a spiral just as actual data does. The model has no DC center to offset the origin of the spiral. This is because the model does not account for constant reflections off of any non-moving objects surrounding the sensor—such as the turbine casing or the non-moving parts of the test setup. Only the reflections off of the surface of the blade are included in overall calculations, and these do not contribute to a DC center. The clearest difference between the two data sets is the slight tilt that may be seen in the experimental data. This is caused by phase imbalance in the sensor. Phase imbalance is present in the sensor when the relative phase between the two channels is not exactly 90°--this causes the data to tilt in one direction or the other.

Figure 52 shows sample plots of each experimental blade along with the same blade as modeled.

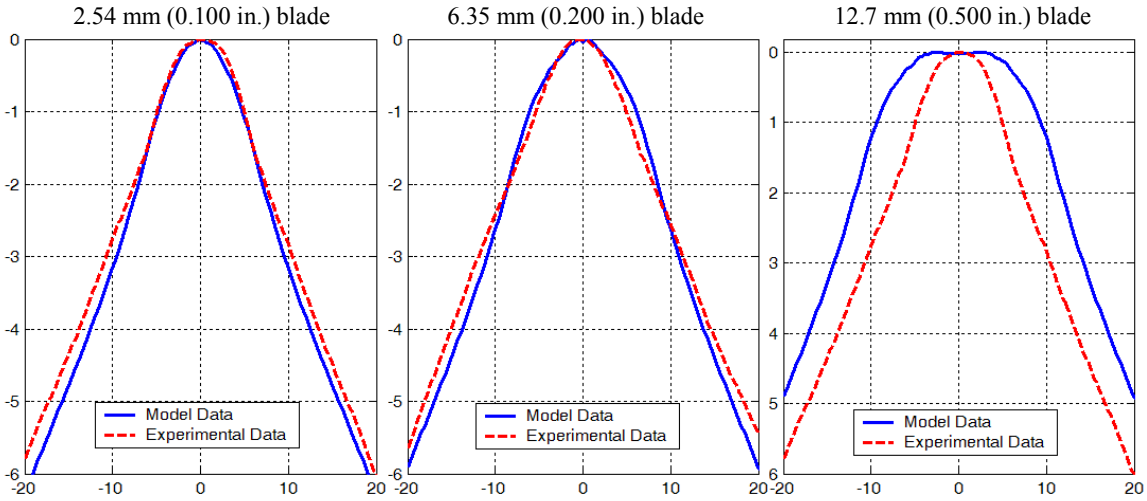

Figure 52. The phase plots of the modeled blade passes and the experimental blade passes are similar, but the wider blade causes problems.

The model accurately predicts that the phase measurements of the sensor are more rounded than the ideal measurement (refer back to Figure 29). For the blades that are thinner than the antenna aperture the modeled phase measurements are qualitatively similar to the experimental measurements; however, the model predicts a wider measurement for the 12.7 mm (0.500 in.) blade.

Figure 53 shows a comparison of the RCS plots from modeled blades and experimental blades. RCS units are relative to transmitted power; RCS results scale when transmit power is changed—though phase results remain the same. Therefore, model and experimental RCS units may not be directly compared. In this figure, experimental RCS has been scaled by a multiplier to match modeled RCS at the peak

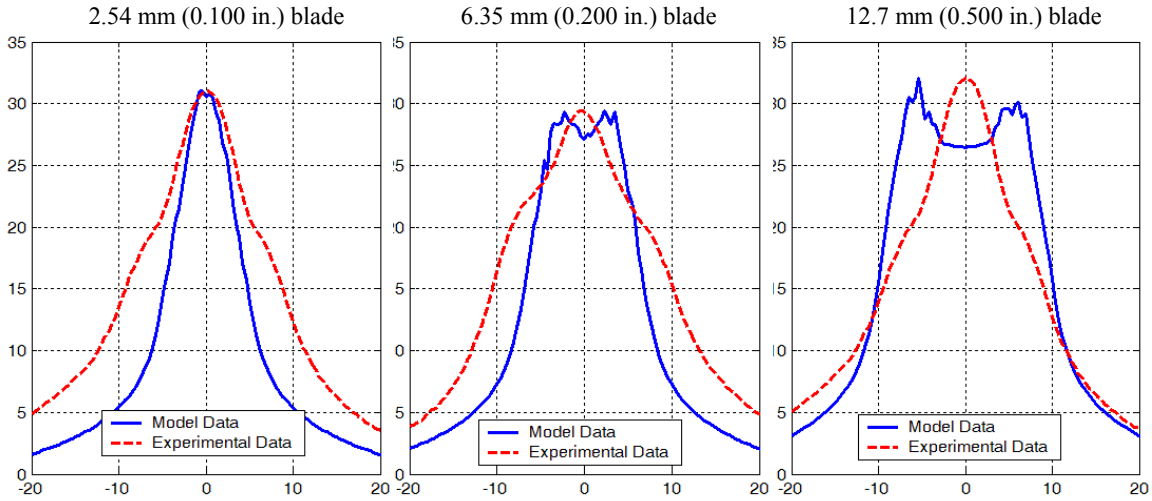

Figure 53. The RCS plot of modeled blade passes shows some noise when the blade passes directly in front of the sensor. The RCS of an experimental blade pass does not show the noise. Modeled RCS also shows a dip at the blade tip.

At the peak of the modeled RCS measurements, there is some noise. This is due to the coarseness of the blade and sensor meshes interacting at the tip. As the clearance between the blade tip and sensor decreases, the discretization of the mesh has more of an influence on the measurement. Measurements from individual points on the meshes constructively and destructively interfere with each other to add noise to the model's overall measurement. Adaptive meshing is helps to compensate for this, but mesh density is still a limiting factor because of computational intensity. This is further discussed later in the context of model results.

Also note that the modeled RCS measurements of larger blades show a dip when the blade is directly in front of the sensor. Experimental results do not show this. This is likely caused by an electromagnetic simplification in the model. The model does not account for diffraction—the microwave bending around corners. Therefore, the modeled sensor cannot detect anything that is not directly in line-of-sight. The actual sensor

receives some reflection from all of the blade since the microwaves bend around the corners. The model does not account for this energy received, so the RCS dips when the blade is directly in front, blocking out the view of the sides of the blade.

Model Data Analysis and Responses

From these data, the three responses to the DOE are derived in the same manner, as discussed previously with actual sensor data. The results of the three responses are analyzed in a similar fashion (main effects plots, residual plots, and ANOVA statistics) to spot trends and compare these trends with those of experimental data. For each response, the influence of the individual input factors on the model is seen graphically in the main effects plot. The residual analysis is seen in the residuals graphic, which shows variations from a normal distribution and variation by order. Finally, the ANOVA statistics specifically quantify the statistical significance of each input-response relationship. This presentation is the same as the main effects plotting of experimental data. The relative percent change from the main effects plots may be compared between experiments and model runs. This comparison gives an idea of how well the model predicts reality.

However, the ANOVA statistical approach has a slightly different meaning for model data. The ANOVA approach determines the influence of a certain factor as statistically significant if the correlation between the input and the response is stronger than the influence of noise in the system. The computational model gives the same types of output as experimental data, but the influence of noise is very different. In model data, a significant amount of noise is only found in the calculated RCS; the phase response shows little noise. Noise appears in RCS calculations when the discretization of the

model is not sufficiently small compared to the clearance between the sensor and the blade (i.e. when the modeled blade clearance is small relative to the size of the discretization steps of the sensor and blade meshes). If the simulated blade pass is at a higher clearance level, the noise is greatly decreased.

As described in Chapter 8, the F* statistic is used to determine the significance of a linear trend relative to the noise in the data. Because there is very little noise in modeled data, the F* statistic is generally higher for all input-response relationships in the model analysis and most trends are statistically significant. For some reason, though, the trends are never significant for the influence of blade tilt; speculation about this is included later. The confidence derived from this statistic does not directly compare to experimental data because of the different noise levels. However, the relative trends of the data, seen in the main effects plots, are the still meaningful for comparing the model to reality.

Phase Response

The model computes the phase response of certain measurement geometries by summing together all of the individual phase responses of the points that lie across the surfaces of the sensor aperture and blade. The relative magnitude of each individual response vector is the calculated strength of the returned signal. In essence, the final phase response is a weighted average of the phases to each of the points on the surface of the blade. The phase response is the most important sensor measurement because distance measurements are directly proportional to the phase of the returned signal.

Experimental data reveals that the most influential factors on the phase response of the system are blade clearance, twist, and width. Of these, blade clearance has a much

greater influence than the others. Model data gives similar results. Figure 54 shows the main effects plot of the maximum phase response of the modeled data.

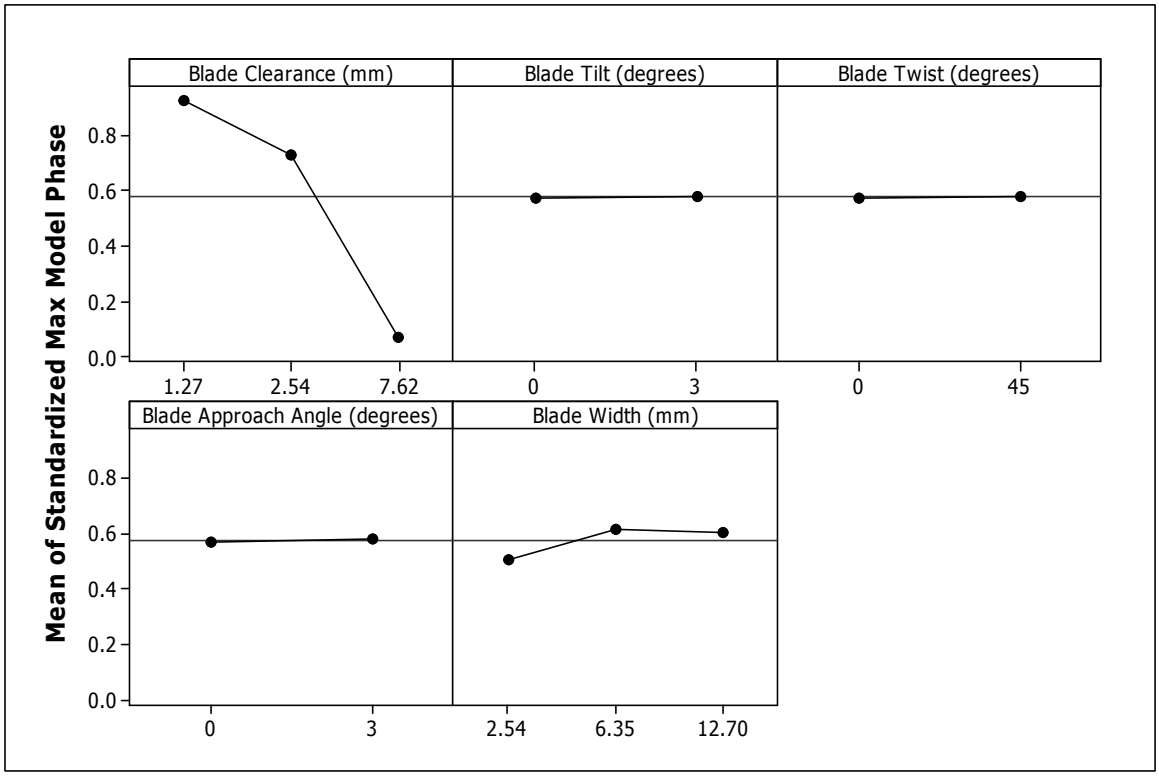

Figure 54. The main effects plot of peak phase for the model is similar in trends to that of the actual sensor.

As seen in Figure 54, blade clearance is the greatest influencer of phase response. This is the same as the result of experimental data. Comparing Figure 54 to Figure 42, the similarities in the responses may be seen.

In both experimental and model data, the other factors all influence phase response less than 15%. Figure 55 shows the relative changes for both model and experimental phase response.

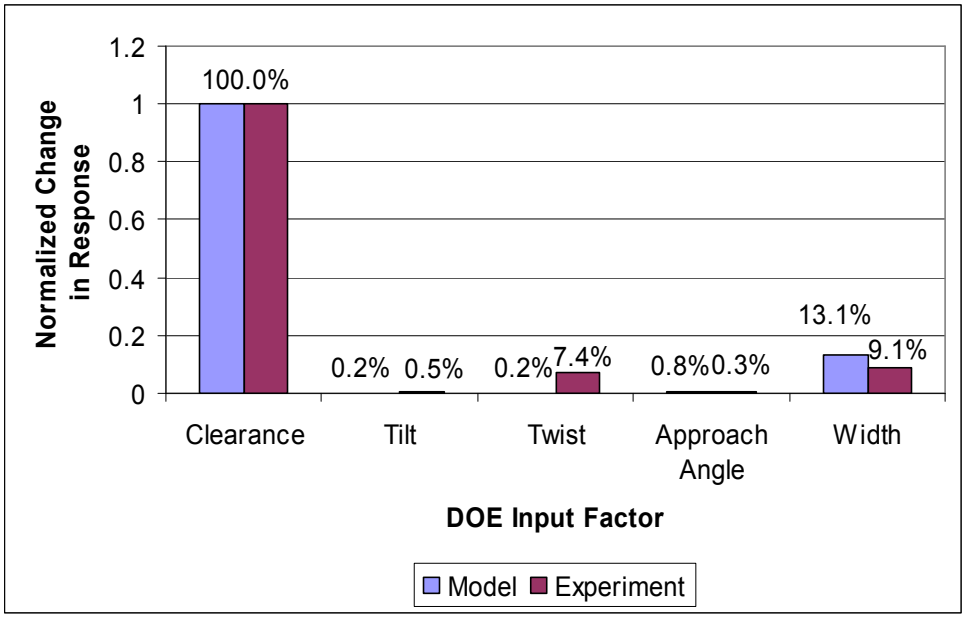

Figure 55. The relative changes in phase response of the model and experiments due to each of the DOE input factors.

The two factors that least influence phase response experimentally are tilt and approach angles. As described before, this validates the use of the sensor for tip clearance measurements since these are the two factors that may vary slightly in actual turbine performance. However, the blade twist and width do not vary greatly over the life of a single turbine (though they may vary greatly from engine to engine). During actual turbine operation, the only factor that significantly influences phase response of the sensor in experimental and model data is the clearance of the blade tip; therefore, the phase is a good indicator of relative clearance measurements.

The model varies from experimental data most in the response of the phase to blade twist. Here, the model predicts an increase of 0.2% of change due to clearance while an increase of 7.4% relative change is seen experimentally. The model predicts that the blade will appear to be closer to the sensor as the twist angle increases.

Experimental data shows that as the blade twists, it appears to move away from the sensor in its phase response. Also, the model predicts that this impact will be less than is found in experiment. The reason for these discrepancies likely involves the polarity of the microwaves relative to the direction of the blade. This polarity may cause microwave interactions that the model does not account for—especially diffraction.

As stated before, the noise in the phase response of the model data is small. The result of this is that all of the trends seen in the data are statistically significant, but the response to blade clearance changes is, by far, the greatest. Table 5 shows the ANOVA statistics for modeled phase response.

Table 5. The ANOVA statistics of the maximum phase response of the model data to the input factors of the DOE.

Factor	C_i	r^2
Blade Clearance	100.%	99.85%
Blade Tilt	91.8%	
Blade Twist	98.8%	
Blade Approach Angle	100.%	
Blade Width	100.%	

Blade tilt and twist influence phase response the least, according to model data. From the main effects plot, a tilt of 3° or a twist of 45° affects a change of 0.2% of the relative influence of clearance, on average. Because this value is small compared to the noise in the modeled phase data, the noise is noticeable in relation to it. This results in the confidence of a linear relationship of only 91.8% and 98.8%. Both of these values are still statistically significant.

Maximum Radar Cross-Section Response

Despite the influence of noise on some of the modeled RCS data, the responses are similar to those of experimental data. Figure 56 shows the main effects plot of the input factors of the DOE on the response of maximum RCS. The greatest influencer, again, is blade clearance. This is due to atmospheric attenuation of microwaves as they travel to and from the blade. Less reflected energy returns to the sensor as the clearance (and therefore attenuation) increases.

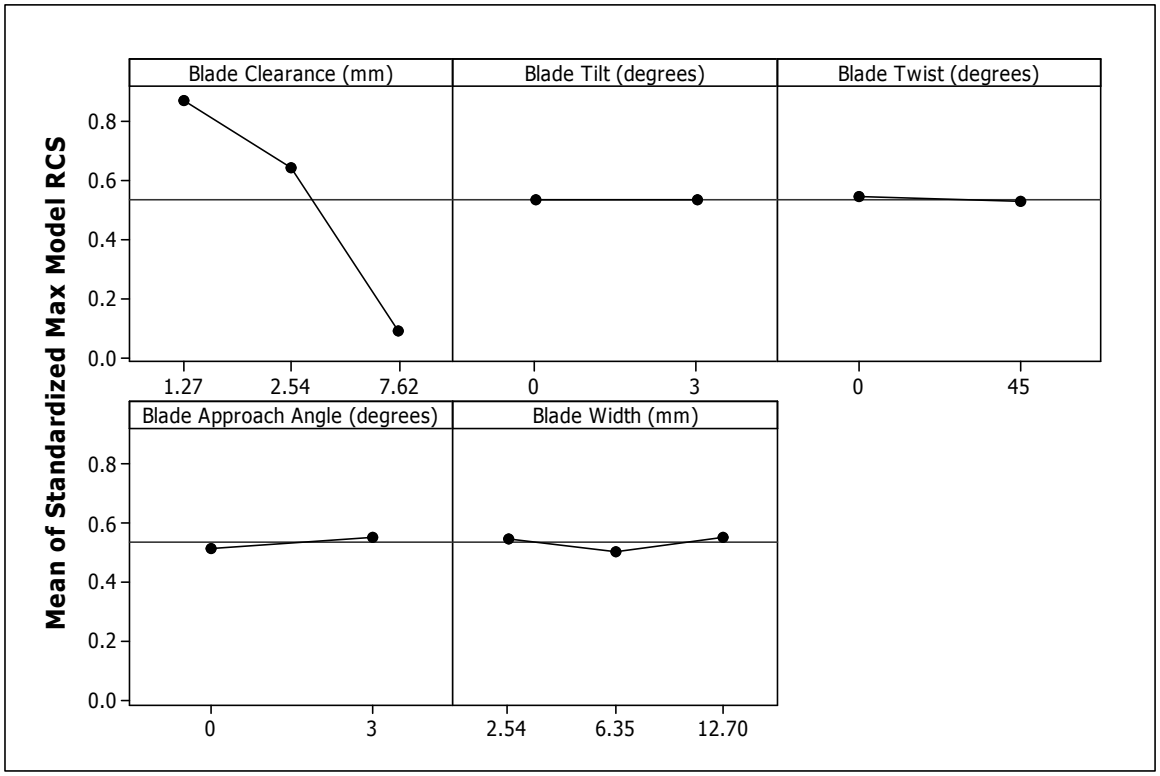

Figure 56. The main effects plot of modeled RCS shows that clearance is clearly the greatest influence on RCS.

Comparing modeled and experimental results (Figure 56 and Figure 49, respectively), the trends are consistent. Figure 57 plots these influences numerically.

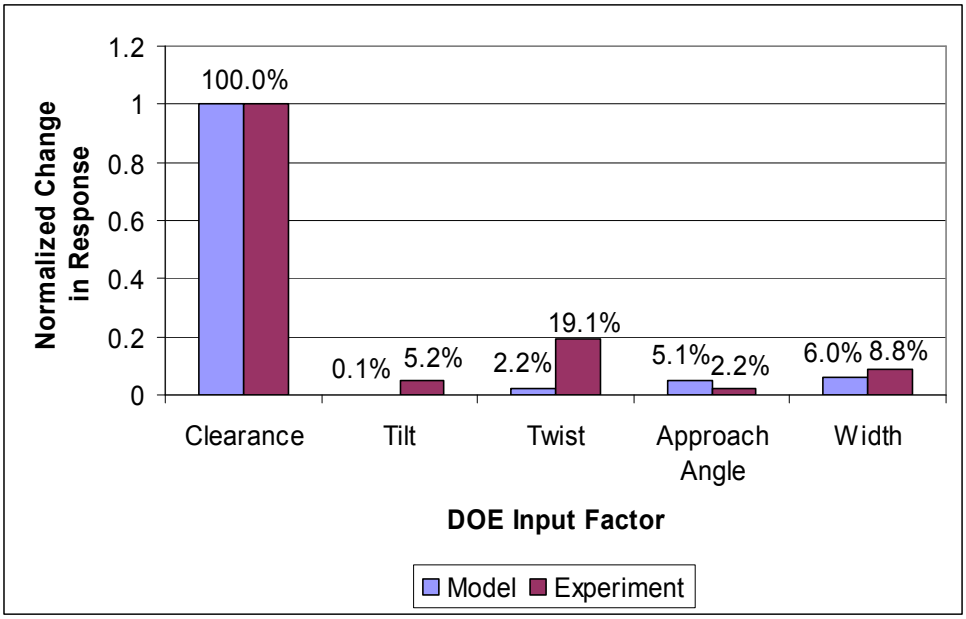

Figure 57. The relative changes in maximum RCS due to the input factors of the DOE.

RCS is the noisiest data calculated by the model. This is likely the explanation of the minor differences between the two. Experimental data shows that blade twist is the second most influential input factor. As in the modeled phase response results, twist has less of an influence on modeled RCS than experimental RCS. However, the trend of blade twist's effect on maximum RCS is similar between model and experiment in that the maximum RCS decreases as the blade twists from 0° to 45°. Blade tilt and approach angle also show similar trends between modeled and experimental data, though the effect of blade tilt on modeled RCS is negligible and statistically insignificant. The ANOVA statistics for the maximum RCS response of modeled data are shown in Table 6.

Table 6. The ANOVA statistics from the analysis of DOE input factors' influences on maximum modeled RCS response.

Factor	C_i	r^2
Blade Clearance	100.%	97.1%
Blade Tilt	28.7%	
Blade Twist	100.%	
Blade Approach Angle	100.%	
Blade Width	100.%	

Model data shows an opposite trend in the effect of blade width on maximum RCS response. In both model data and experimental data, this trend is statistically significant by the ANOVA statistics. This is interesting because both trends are non-linear, as may be seen in Figure 56 and Figure 49, but they are opposite. The cause for the difference between the trends in the maximum RCS response to blade width is uncertain. One possible cause is the same as is proposed for the discrepancy caused by blade twist: the model does not account for diffraction of microwaves around corners of blades. Therefore, the actual sensor receives reflections from the sides of the blade that are not visible to the sensor in the ray-tracing model. This may cause increased RCS measurements from wider blades in experimental data. The model assumes that only surfaces within line-of-sight affect sensor measurements.

Apparent Blade Width Response

The major trends of the modeled apparent blade width also match the trends in the experimental data. Figure 58 shows the main effects plot obtained from model data.

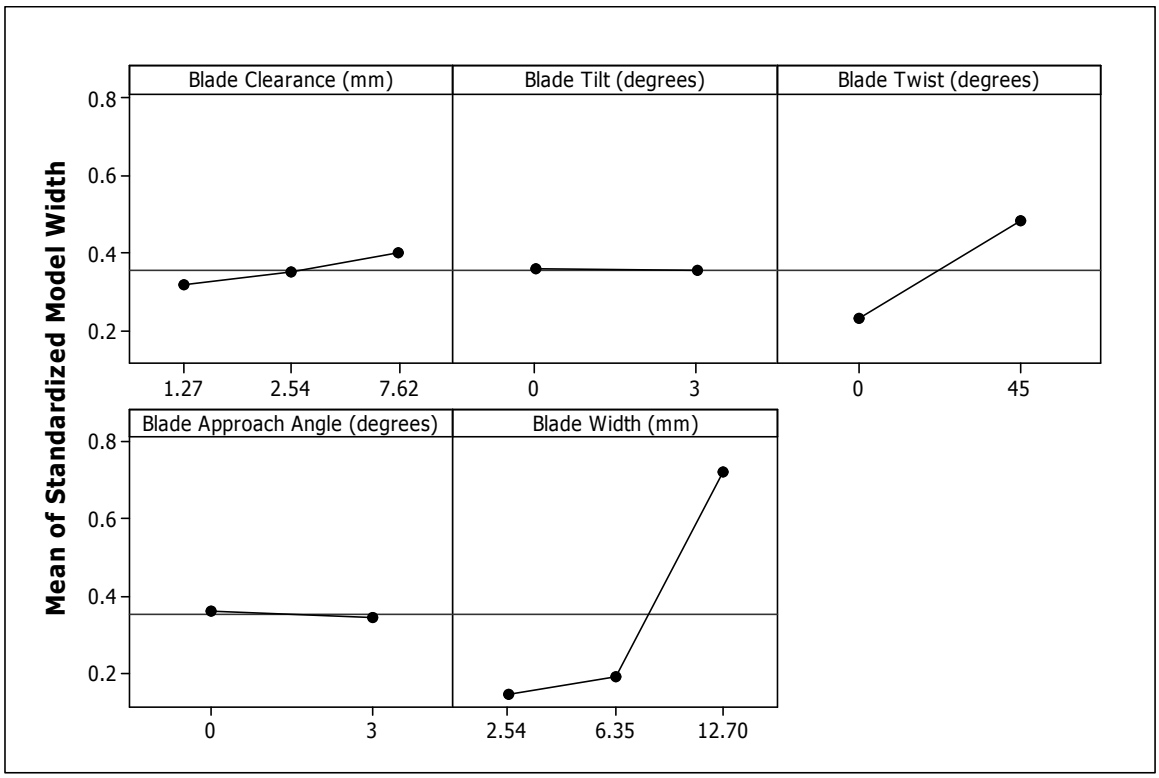

Figure 58. The main effects plot of apparent blade width at a depth of 1.27 mm (0.0500 in.) from the peak.

When compared to the experimental main effects plot in Figure 46, the plots show the similar trends directionally. The three factors that influence apparent width most in the model are clearance, twist angle, and actual width—this is the same as the experimental DOE result. In general, the model accurately predicts an upward trend in apparent width as these three factors are increased. However, within these three, the amount of influence varies somewhat from experimental trends. Figure 59 shows the relative influence of each input factor on the output response.

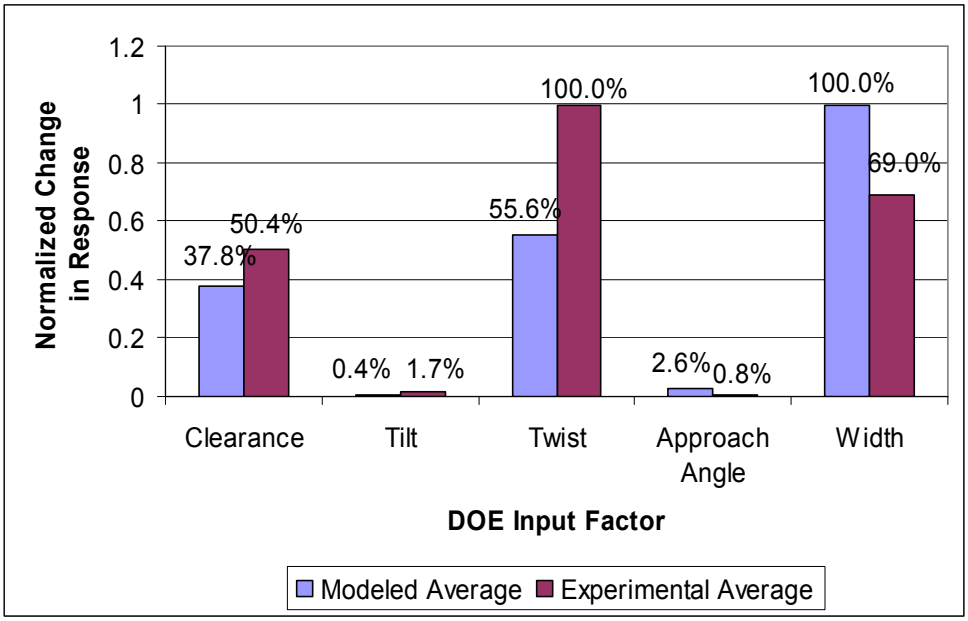

Figure 59. The relative influences of the DOE input factors on the apparent blade width response for experimental and model data. The data from the three depths are averaged together for each data set.

The model predicts that actual blade width affects apparent width most heavily, but experimental data shows that blade twist has the greatest influence. The model also predicts less change in apparent blade width from increased clearance than is present in experimental data.

For blade tilt and approach angles, the model predicts an opposite trend to that of the experimental DOE. However, for tilt, the modeled influence is not statistically significant relative to the noise in the system, so this trend is not necessarily valid. Table 7 shows these statistics.

Table 7. The ANOVA statistics of the modeled response of apparent blade with at a depth of 1.27 mm (0.0500 in.) to the input factors of the DOE.

Factor	C_i	r^2
Blade Clearance	100.%	95.7%
Blade Tilt	56.1%	
Blade Twist	100.%	
Blade Approach Angle	100.%	
Blade Width	100.%	

The confidence in the trend of blade tilt predicted by the model is 56.1%. So this trend is unsure. The confidence in the experimental trend is low also. No conclusion may be drawn from this data except that if blade tilt indeed has an influence on apparent blade width, it is not very large compared to any of the other inputs (if it were, it would certainly show up). The confidence in the trend of blade approach angle's influence on the modeled apparent blade width, on the other hand, is 100.%. While this trend is certain, the corresponding trend in experimental data (which is opposite), is not statistically significant. From Table 3, the confidence in the experimental trend is only 14.1%. Therefore, no conclusion may be drawn as to whether or not the model accurately predicts the influence of approach angle on apparent blade width.

Overall, the model accurately predicts the major trends of the relationships between the input factors of the DOE and the responses of maximum phase, maximum RCS, and apparent blade width. The model is most accurate in its predictions of maximum phase response. Just as in experimental data, blade clearance is the clear leader in affecting a change in the phase response. This validates the use of the sensor for clearance measurements since phase response is proportional to the displacement measurements that the sensor is designed to measure. The model fails to predict the

relative influences of each input factor accurately. It is often quantitatively off in this regard. Also, many of the minor trends are not predicted well by the model.

CHAPTER 10 CONCLUSION

As discussed in depth above, blade tip measurements are vital to the advancement of turbine operation because of their potential to monitor turbine performance and safety. Tip clearance information may provide for more efficient turbines and intelligent control systems. However, this task cannot be accomplished without the development of advanced sensors such as the microwave sensor presented in this thesis. Adequate implementation of this and other sensors represents a significant step in turbine enhancement. Sensors like this one will open the door to more direct control of turbines that will, in turn, lead to increased efficiency and overall system performance. As demand for energy and transportation continues to increase, efficiency and performance will become more important and lucrative.

The measurement of turbine blade tips is important, but it is not a simple task because the conditions of measurement are complex. Precise and accurate data must be taken at high rates, high temperatures, and in hostile noise conditions in order to accomplish this goal. For several reasons, microwaves present one of the best options for operating in the harsh conditions of a turbine. However, making these measurements with microwaves is a challenge. The relatively long wavelength and wide antenna pattern of microwave sensors make interactions between the beam and target complex. The strong effect of spatial filtering in turbine blade measurements is one result of the large beam width. On the other hand, a laser—which has a small beam width and is nearly ideal for precise measurement—cannot withstand the temperatures or low visibility conditions within the hot section of a turbine. It is a trade-off, but in the end the microwave sensor is a viable technology because of its ability to survive and operate in

the harsh environment of a turbine. To overcome an inherent lack of precision caused by the large spot size on the target, the complexity of the microwave system and its measurements needs to be understood. This research has focused on one portion of that complexity in order to set a path for progressing to a viable sensing system. The turbine blades are blurred as a result of spatial filtering, but a blurred view into the heart of a turbine is better than no view at all. If spatial filtering is understood well enough, the sensor's measurements may be interpreted to obtain correct blade tip data.

Experimentation and modeling used in the research are presented to improve the understanding of spatial filtering. The experimentation is in the form of a five-factor, full-factorial design of experiments, intended to increase qualitative understanding by revealing trends in data from geometric factors that vary in turbine performance. The experiments are idealized for the purpose of simplifying overall geometry.

The most notable result from the experimental DOE analysis and confirmed by the model analysis is that blade clearance is the only input factor that significantly affects the phase measurement at the tip of the blade during normal turbine operation. The other factors that significantly affect sensor response do not change much during normal operation—the blade width and twist angle of the blade design. Figure 60 summarizes the relative average influences as measured experimentally by the sensor.

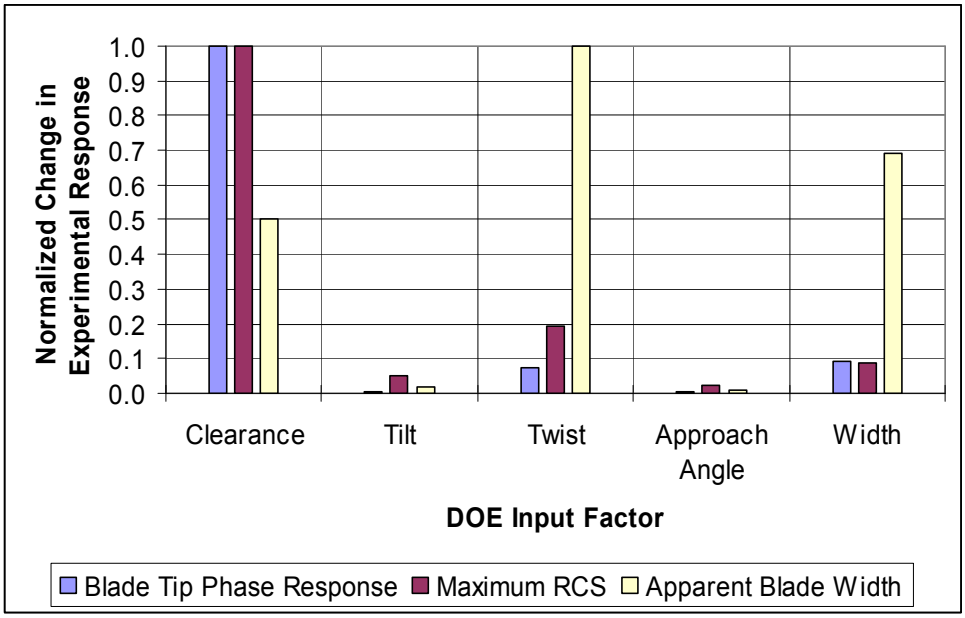

Figure 60. Experimental responses to the input factors of the DOE.

The trends derived from this analysis show that, even at their maximum possible variation in actual turbine operation, these factors influence phase response of the sensor by less than 1% each. This validates the use of the microwave sensor for relative tip clearance measurement because microwave measurements are directly proportional to phase. Phase measurements are only inaccurate relative to one another if blade width or blade twist greatly change, which does not happen in normal turbine operation. However, this also leads to the conclusion that the sensor must be calibrated to accurately compare blade clearance measurements between different geometric situations. If the blade twist and width vary from stage to stage, the affect of spatial filtering on the data is not consistent.

There is another valuable conclusion from this analysis: the factors in the DOE that may change during normal operation significantly affect maximum RCS and apparent blade width—though they do not affect phase response at the tip. Table 8

compiles all of the confidences of the relationships by the experimental and modeled DOE. The confidence levels indicate the significance of the fitted linear relationships relative to the noise in the system.

Table 8. All of the statistical confidences in the relationships between the input factors and responses to the DOE.

	Clearance	Tilt	Twist	Approach Angle	Width
Experimental	(%)	(%)	(%)	(%)	(%)
Tip Phase Response	100.0	39.1	100.0	31.1	100.0
Maximum RCS	100.0	100.0	100.0	99.8	100.0
Apparent Blade Width at 1.27 mm Depth	100.0	91.3	100.0	14.0	100.0
Apparent Blade Width at 2.54 mm Depth	100.0	77.6	100.0	48.1	100.0
Apparent Blade Width at 5.08 mm Depth	100.0	77.6	100.0	48.1	100.0
Modeled	(%)	(%)	(%)	(%)	(%)
Tip Phase Response	100.0	90.8	98.8	100.0	100.0
Maximum RCS	100.0	28.7	100.0	100.0	100.0
Apparent Blade Width at 1.27 mm Depth	100.0	100.0	100.0	100.0	100.0
Apparent Blade Width at 2.54 mm Depth	100.0	39.0	100.0	100.0	100.0
Apparent Blade Width at 5.08 mm Depth	100.0	39.0	100.0	100.0	100.0

Above 95% Confidence

Since these factors affect RCS and blade width measurements, it may be possible to draw more information about blade condition and geometry than just blade clearance. This may be accomplished by analyzing the RCS as well as the phase of measurements. These influences are likely to be small, but very accurate measurement might account for this. If the phase response does not change in a measurement and the RCS changes by 1-5%, this is an indication that blade twist, tilt, or approach angle may have changed.

The computational model developed in this thesis provides a method of comparing the theoretical basis of spatial filtering to reality. The model was subjected to the same DOE as the actual system was, and the results show the strengths and weaknesses of the theoretical basis and give insight that may develop the theoretical understanding further. Figure 61 summarizes the normalized results of this analysis.

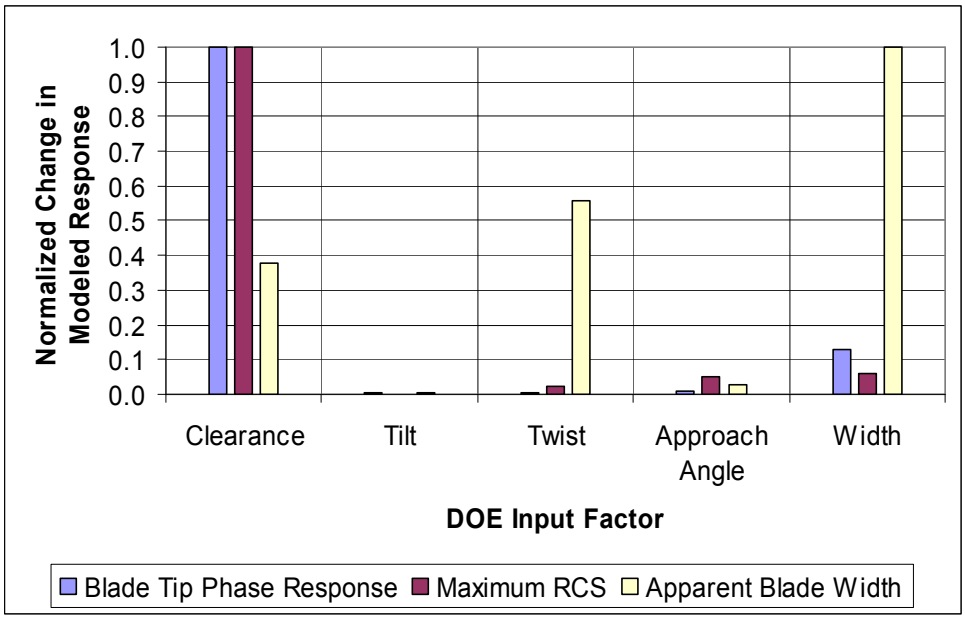

Figure 61. Modeled responses to the input factors of the DOE.

The prominent trend, found experimentally—that blade clearance is the most influential factor on sensor phase response—is predicted accurately by the computational model. In fact, the model predicts most of the strong trends of the influence of DOE input factors on sensor responses accurately. However, the model results diverge from experimental results in many small ways. Most notably, noise in the modeled RCS calculations due to insufficient discretization of the three-dimensional meshes leads to

low quality simulated measurements. Also, the lack of electromagnetic complexity in the ray-tracing model leads to the failure of the model at exactly predicting more sensitive trends in data.

The research of this thesis confirms that spatial filtering has a measurable effect on microwave measurements of turbine blades, and therefore, it needs to be considered and compensated for. However, the blurring of blade tips due to spatial filtering is not altogether detrimental to sensor measurements. If care is taken and further study is performed, it is possible to overcome this difficulty to make highly accurate blade tip clearance measurements. It is also possible that even more sophisticated blade tip measurements may be inferred from microwave sensor data. These measurements hold the potential to greatly enhance turbine operation and development in the future.

CHAPTER 11 FUTURE WORK

Much is left to be done before the effect of spatial filtering in microwave measurements of turbine blades is fully understood, but there is great motivation to complete this task. The goal of this thesis is to gain a more comprehensive theoretical and qualitative understanding of the phenomenon. It is possible that through a deeper, quantitative study, it may be feasible to remove errors caused by spatial filtering and perhaps measure more than simply the clearance of the turbine blade tip. However, before that may happen a number of tasks must be accomplished. Experimentation and modeling must both be extended and improved.

Experimental Progress

The first task that needs to be accomplished is the continued development of the microwave sensor and antenna for improved sensor operation. As the first sensor of its type, this microwave sensor represents very new and powerful technology with great potential. However, the sensor still needs to have that potential cultivated. One example of an area of sensor operation that must be developed is that of temperature sensitivity. The experiments in this thesis have been shown to be sensitive even to small temperature changes of the sensor electronics, cable, and antenna. Since this sensor is designed for operation in turbines, it must be able to function well with fluctuating temperatures and vibrations. The latest versions of the sensor have overcome this difficulty, but it was not available in time for this research.

Once sensor operation is improved, experimental analysis may proceed. The DOE described in this thesis provides valuable insight into the broad trends in the

phenomenon of spatial filtering. However, the results are mostly qualitative and lack sufficient detail to fully understand how the input factors influence spatial filtering. The next step in studying spatial filtering is to look at each of the five input factors in a more detailed, quantitative fashion. This is especially important for those factors that are most influential on the response of the sensor; the three most influential are blade clearance, twist, and width. A large set of sensitivity experiments in which the factors are varied one at a time, in small increments, over their full useful range, is the way to define this influence quantitatively. This quantitative analysis may then be applied to actual sensor measurements as a rough error map to correct for unwanted spatial filtering. Without this analysis or performing a full error map over the measurement range, the errors are present and uncompensated for.

Another shortcoming of the DOE is the limitation to five input factors. These five include the most obvious factors, but other factors such as the complex blade geometry need first to be analyzed qualitatively and then quantitatively to ensure complete measurement accuracy and robustness. Actual turbine blades are designed based on efficiency of airflow, not microwave reflection. In reality, they have some twist that changes along the blade length, the thickness is not consistent throughout, and the tip may not be flat. The radar cross-section of such blades is considerably different than the ideal flat blades used, and this must be studied.

The geometry of the surrounding are also changes significantly amongst different installations, possibly affecting the measurements as well. The sensor faces directly into a turbine stage with other stages nearby. Much of the surface inside a turbine reflects microwaves well. Analysis needs to be performed to determine how much these other

reflections affect measurements. The casing and disk are both excellent microwave reflectors, and blades passing by on either side also provide some oblique reflection if the antenna pattern is wide enough. Though blades directly in front of the sensor are still prominent, the effect of these other measurements needs to be quantitatively analyzed. All of these reflections add together through spatial filtering to result in the final measurement. Any unwanted reflection could alter the measurement taken by the sensor.

Model Improvement

The microwave model developed for this study of spatial filtering is a tool that holds much potential. Engineering design is always enhanced when models are developed that accurately predict reality. It is expensive to build a sensor, install it in a live turbine, and take measurements. On the other hand, it is not expensive to model the physical system in a computer and run calculations. If fine-tuning of sensors must be performed in order to determine the effects of geometry or other factors before final installation and operation, this computational model may provide the analysis rather than extensive physical testing. However, the model developed for this study must be further developed in order to meet this demand.

The fact that the model does not perfectly match experimental results leads to the conclusion that the theoretical basis for the model is incomplete. The model does not fully account for all that is happening in microwave measurements of turbine blade tips. It needs to be augmented in order to more closely resemble experimentation.

First, the model has many electromagnetic aspects that could use further development. Of these are multipath, diffraction, and near-field antenna pattern calculation. Multipath is a term referring to a returned signal containing reflections that

have taken multiple paths before being received back at the sensor. Indirect multipath occurs when a bounce off of some other surface in the surrounding environment occurs before the final reflection off of the target towards the sensor. Direct multipath is the case in which there are multiple reflections between the antenna and target before entering the antenna and being transmitted to the sensor. Since the final phase measurement of the sensor is the aggregate of all reflections, these waves, which have traveled different and longer paths, skew the final measurements. Adding multipath analysis to the model greatly increases the number of ray-tracing reflection calculations the model must complete; it also involves adding more surfaces for reflection than just the blade and sensor.

Another electromagnetic phenomenon that the model does not account for is diffraction around corners. The laws of diffraction are fairly complex and have to do with the relative size of the electromagnetic waves and the target or obstacle. Microwave diffraction may significantly affect actual measurements. Currently, the model does not run calculations on mesh points that are not within a direct line-of-sight of the antenna aperture. To be fully developed and accurate, the model needs to account for this effect.

Finally, the near-field antenna pattern and blade interactions might be included in the model to increase its effectiveness. To this point, the sensor is modeled as a set of point sources and receptors that all have the same transmission pattern. However, the physics involved are actually much more complex than this. The reactive near-field takes its name from the fact that the antenna reacts to the presence of objects within it. True electromagnetic finite-element models solve Maxwell's equations for electromagnetic energy transfer in order to resolve the antenna pattern of a specific geometric situation.

Geometric and material properties are considered in the analysis and are used in these calculations.

All of these ways in which the model could be enhanced are computationally intensive. A full three-dimensional mesh of a turbine stage including all of the surrounding surfaces may have millions of points. Furthermore, accounting for diffraction and multipath exponentially increases the number of calculations per element in the complete measurement. Solving Maxwell's equations for the transmission characteristics of the antenna adds even more on top of this. In order for these advances to be feasible, the computational efficiency of the model needs to be greatly increased. However, if the end result saves hours of installation and testing time and the expense of extensive experimentation, it may be well worth the effort.

APPENDIX A

Experimental Results

Phase Response

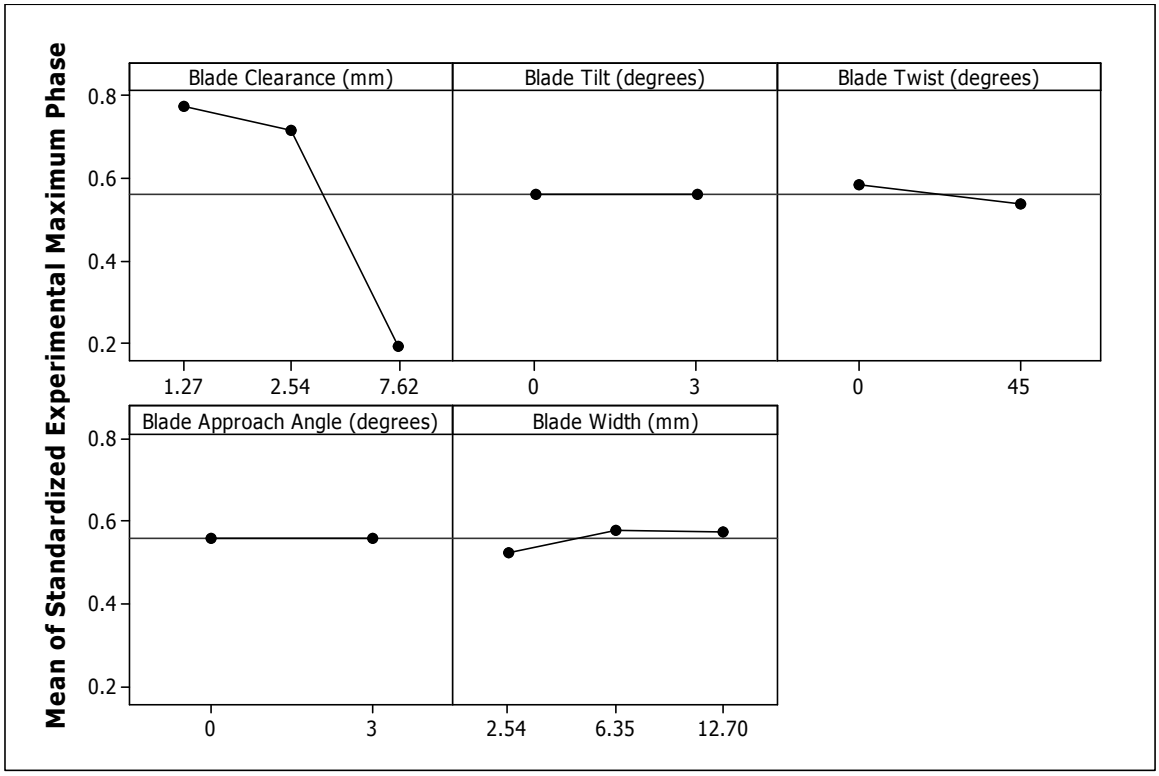

Figure 62. The main effects graphic for experimental phase response.

Table 9. The full ANOVA table for experimental phase response.

Source	DF	Seq SS	Adj SS	Adj MS	F	P
Blade Clearance (mm)	2	58.3523	58.303	29.1515	6070.67	0.000
Blade Tilt (degrees)	1	0.0015	0.0013	0.0013	0.26	0.609
Blade Twist (degrees)	1	0.4053	0.3904	0.3904	81.29	0.000
Blade Approach Angle (degrees)	1	0.0003	0.0008	0.0008	0.16	0.689
Blade Width (mm)	2	0.4837	0.4841	0.242	50.4	0.000
Repetition	3	0.002	0.002	0.0007	0.14	0.938
Error	839	4.0289	4.0289	0.0048		
Total	849	63.2738				
S	0.0692966					
R-Sq	0.9363					
Adjusted R-Sq	0.9365					

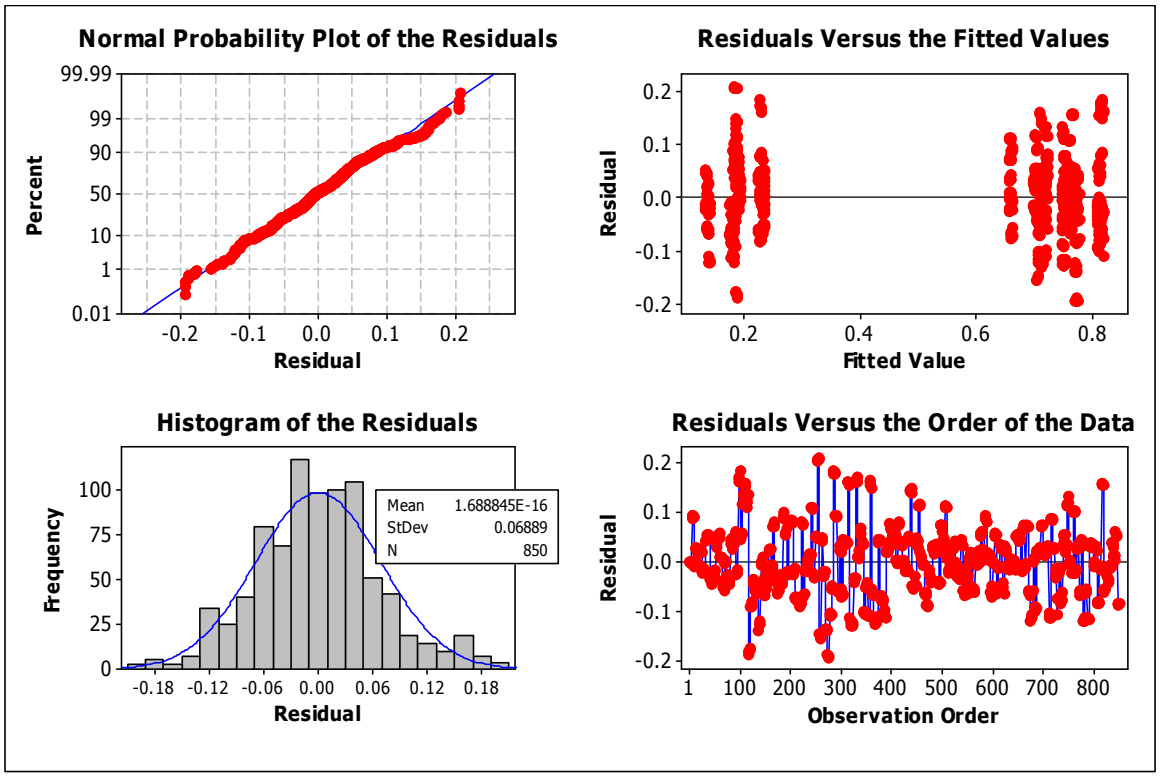

Figure 63. The residuals graphic for experimental phase response.

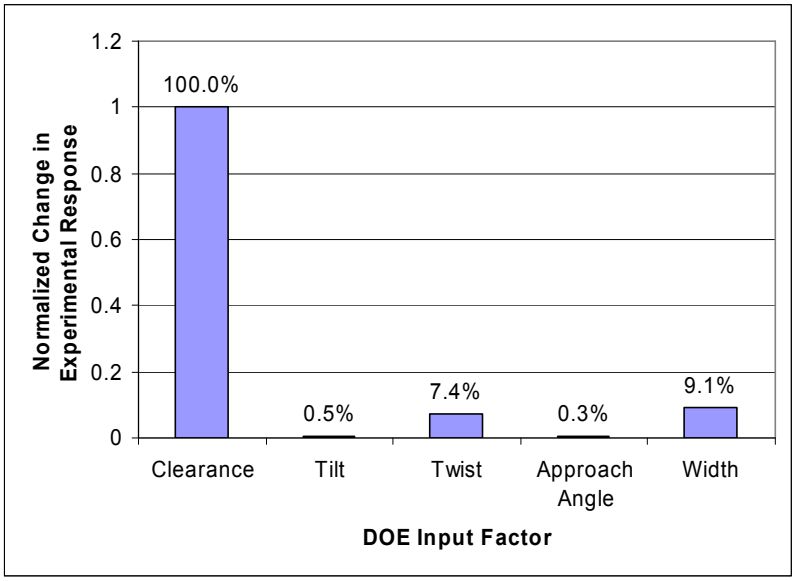

Figure 64. The relative influences of the input factors for experimental phase response.

Apparent Width Response

Apparent Width at 1.27 mm (0.0500 in.) Depth

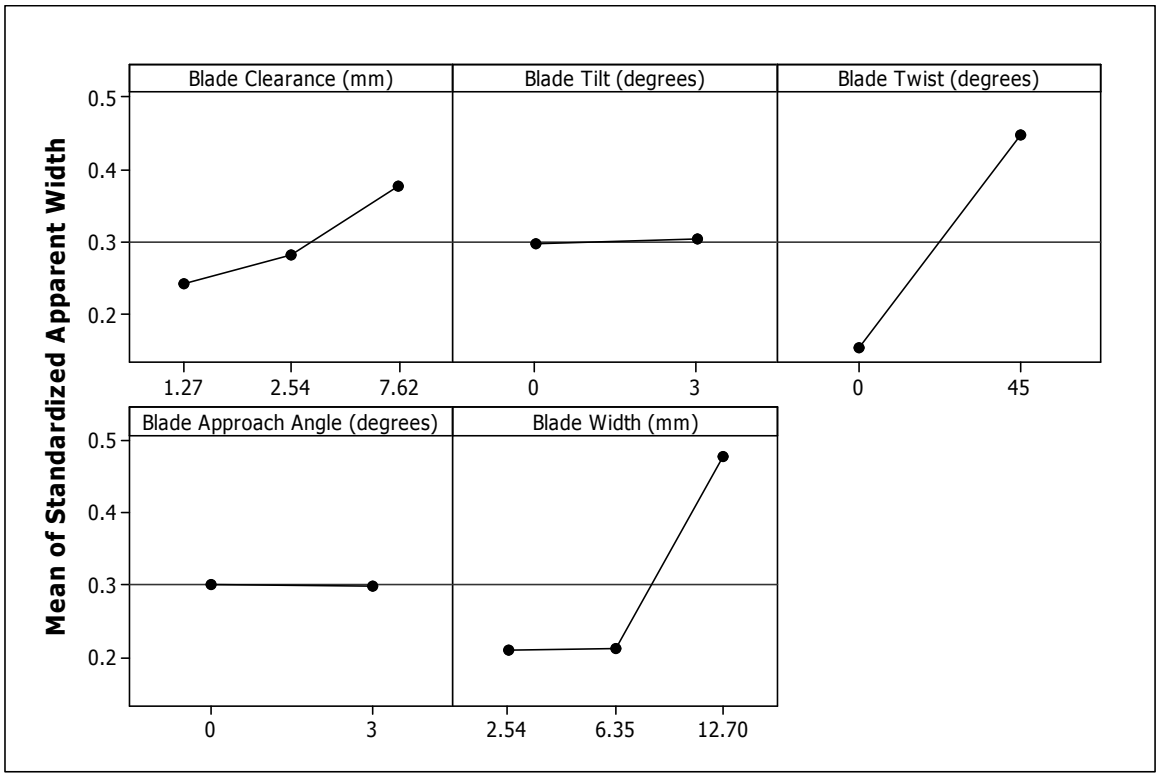

Figure 65. The main effects graphic for experimental apparent width at 1.27 mm (0.0500 in.) depth.

Table 10. The full ANOVA table for experimental apparent width at 1.27 mm (0.0500 in.) depth.

Source	DF	Seq SS	Adj SS	Adj MS	F	P
Blade Clearance (mm)	2	1.8605	2.4131	1.2066	361.19	0.000
Blade Tilt (degrees)	1	0.0044	0.0098	0.0098	2.93	0.087
Blade Twist (degrees)	1	18.756	17.313	17.313	5182.68	0.000
Blade Approach Angle (degrees)	1	0.0029	0.0001	0.0001	0.03	0.860
Blade Width (mm)	2	13.0631	13.0584	6.5292	1954.54	0.000
Repetition	3	0.002	0.002	0.0007	0.2	0.896
Error	801	2.6758	2.6758	0.0033		
Total	811	36.3647				
S	0.0577974					
R-Sq	0.9264					
Adjusted R-Sq	0.9255					

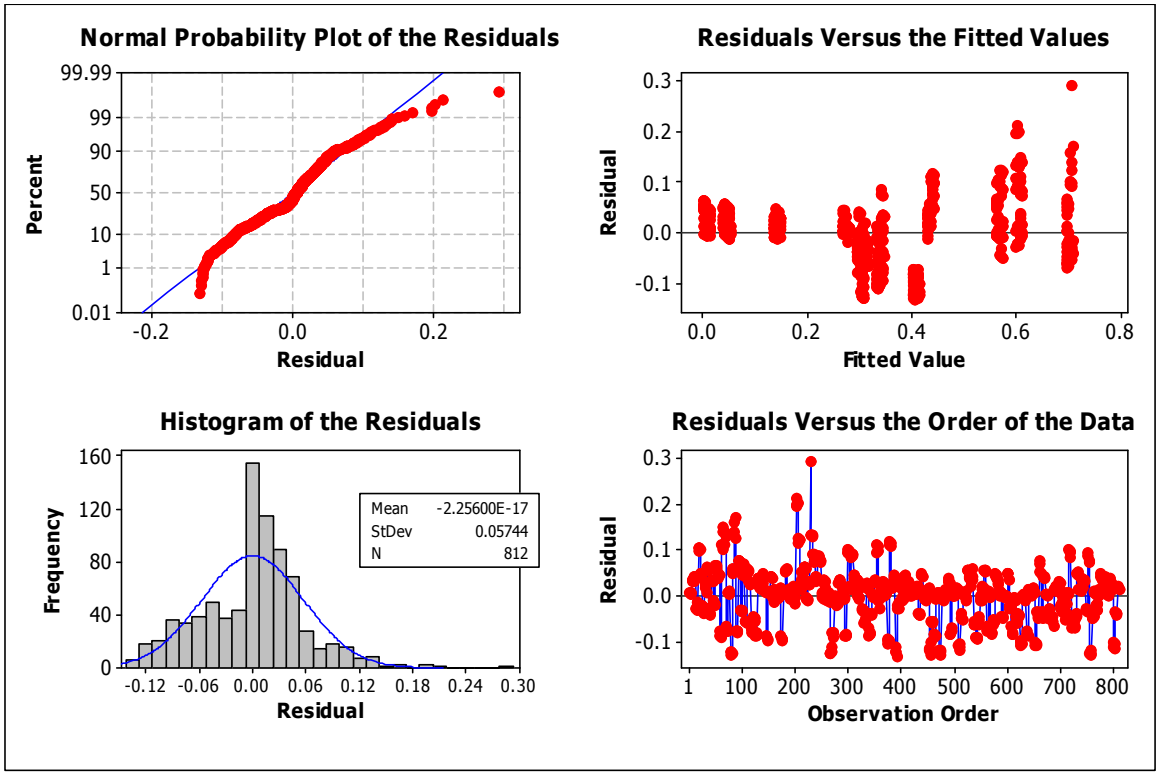

Figure 66. The residuals graphic for experimental apparent width at 1.27 mm (0.0500 in.) depth.

Apparent Width at 2.54 mm (0.100 in.) Depth

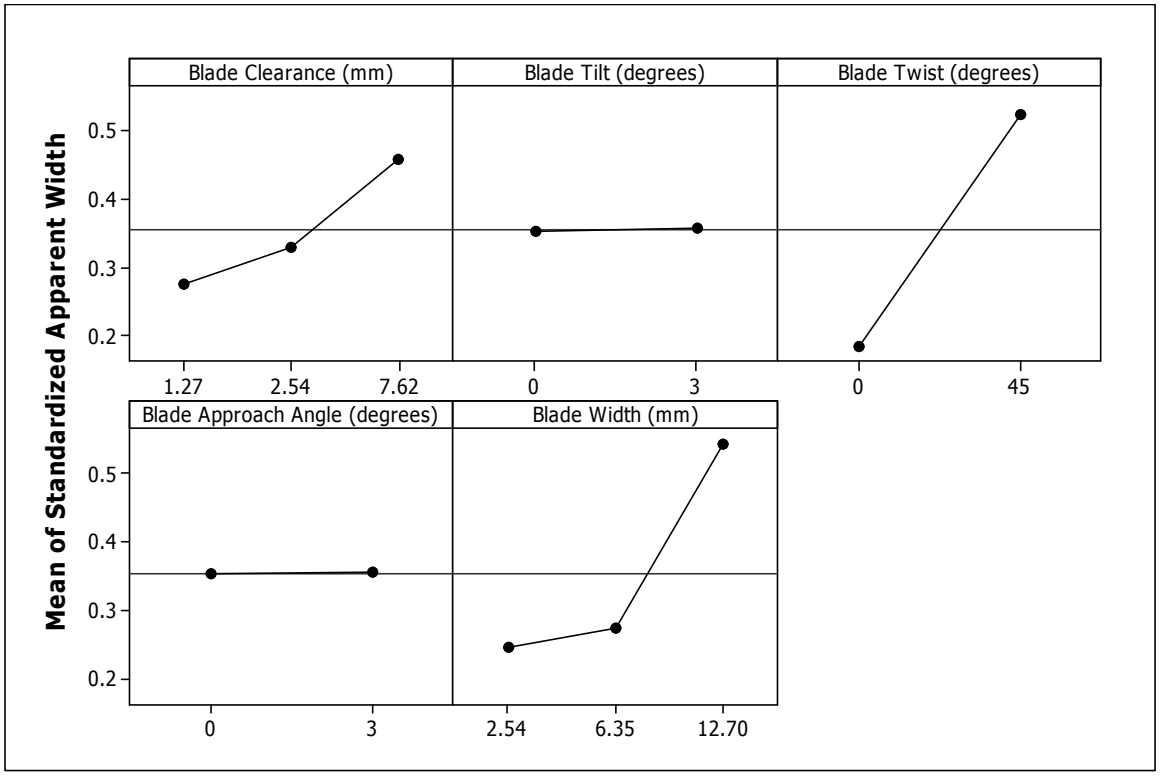

Figure 67. The main effects graphic for experimental apparent width at 2.54 mm (0.100 in.) depth.

Table 11. The full ANOVA table for experimental apparent width at 2.54 mm (0.100 in.) depth.

Source	DF	Seq SS	Adj SS	Adj MS	F	P
Blade Clearance (mm)	2	1.9055	3.6148	1.8074	609.94	0.000
Blade Tilt (degrees)	1	0.0048	0.0044	0.0044	1.48	0.224
Blade Twist (degrees)	1	24.2722	19.3671	19.3671	6535.88	0.000
Blade Approach Angle (degrees)	1	0.0004	0.0012	0.0012	0.42	0.519
Blade Width (mm)	2	13.6004	13.5941	6.797	2293.81	0.000
Repetition	3	0.001	0.001	0.0003	0.12	0.951
Error	727	2.1542	2.1542	0.003		
Total	737	41.9386				
S	0.0544353					
R-Sq	0.9486					
Adjusted R-Sq	0.9479					

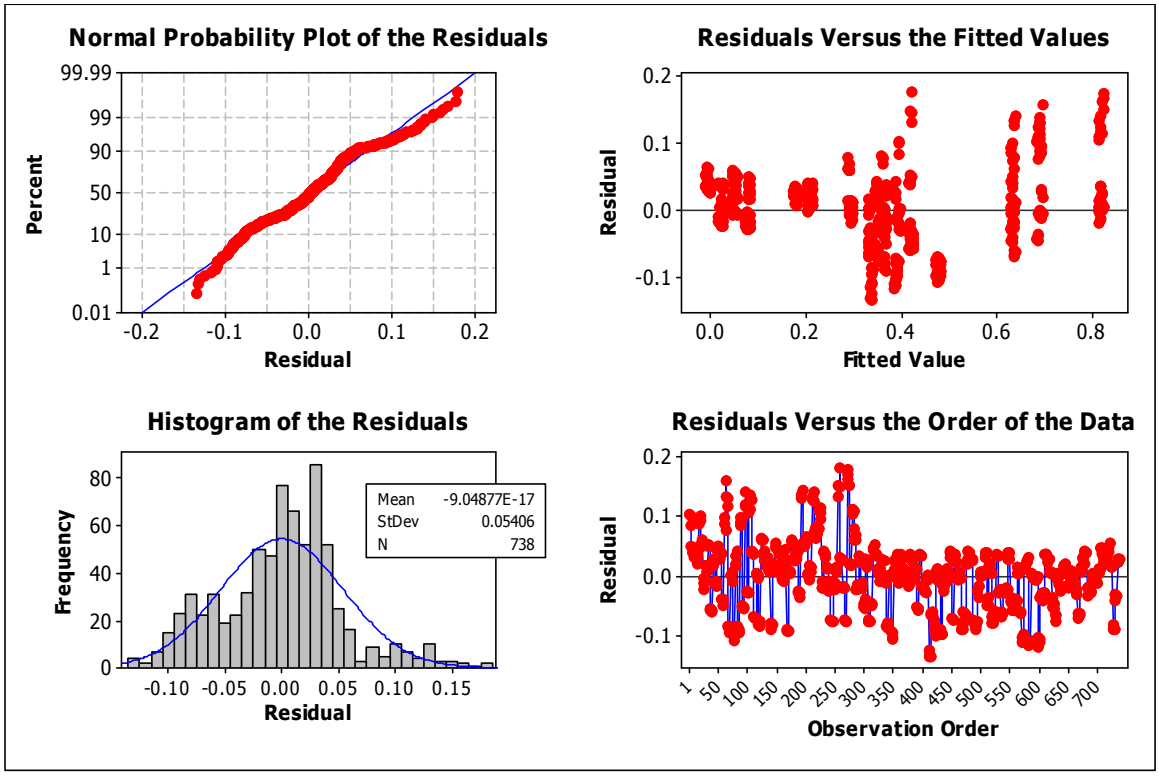

Figure 68. The residuals graphic for experimental apparent width at 2.54 mm (0.100 in.) depth.

Apparent Width at 5.08 mm (0.200 in.) Depth

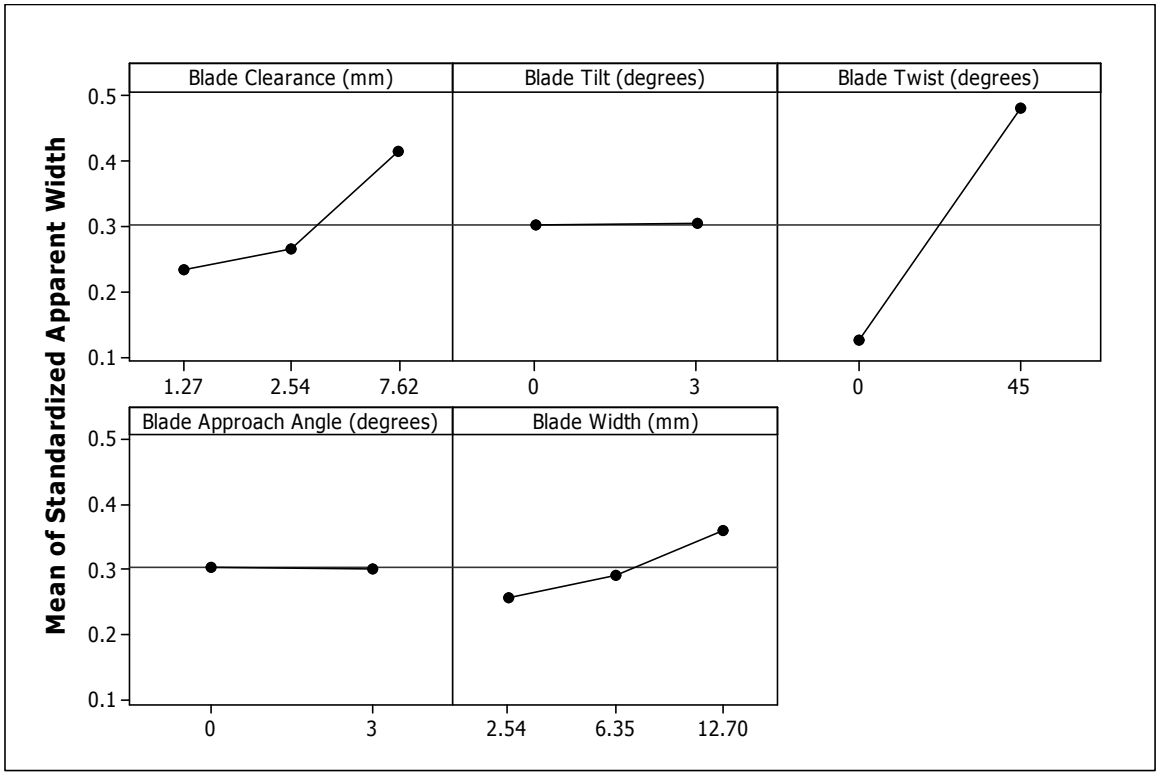

Figure 69. The main effects graphic for experimental apparent width at 5.08 mm (0.200 in.) depth.

Table 12. The full ANOVA table for experimental apparent width at 5.08 mm (0.200 in.) depth.

Source	DF	Seq SS	Adj SS	Adj MS	F	P
Blade Clearance (mm)	2	2.7267	4.5771	2.2886	239.23	0.000
Blade Tilt (degrees)	1	0	0.0034	0.0034	0.36	0.550
Blade Twist (degrees)	1	24.2522	24.2425	24.2425	2534.17	0.000
Blade Approach Angle (degrees)	1	0.0024	0.0041	0.0041	0.43	0.511
Blade Width (mm)	2	1.4556	1.4522	0.7261	75.9	0.000
Repetition	3	0.0505	0.0505	0.0168	1.76	0.153
Error	780	7.4617	7.4617	0.0096		
Total	790	35.9492				
S	0.0978072					
R-Sq	0.7924					
Adjusted R-Sq	0.7898					

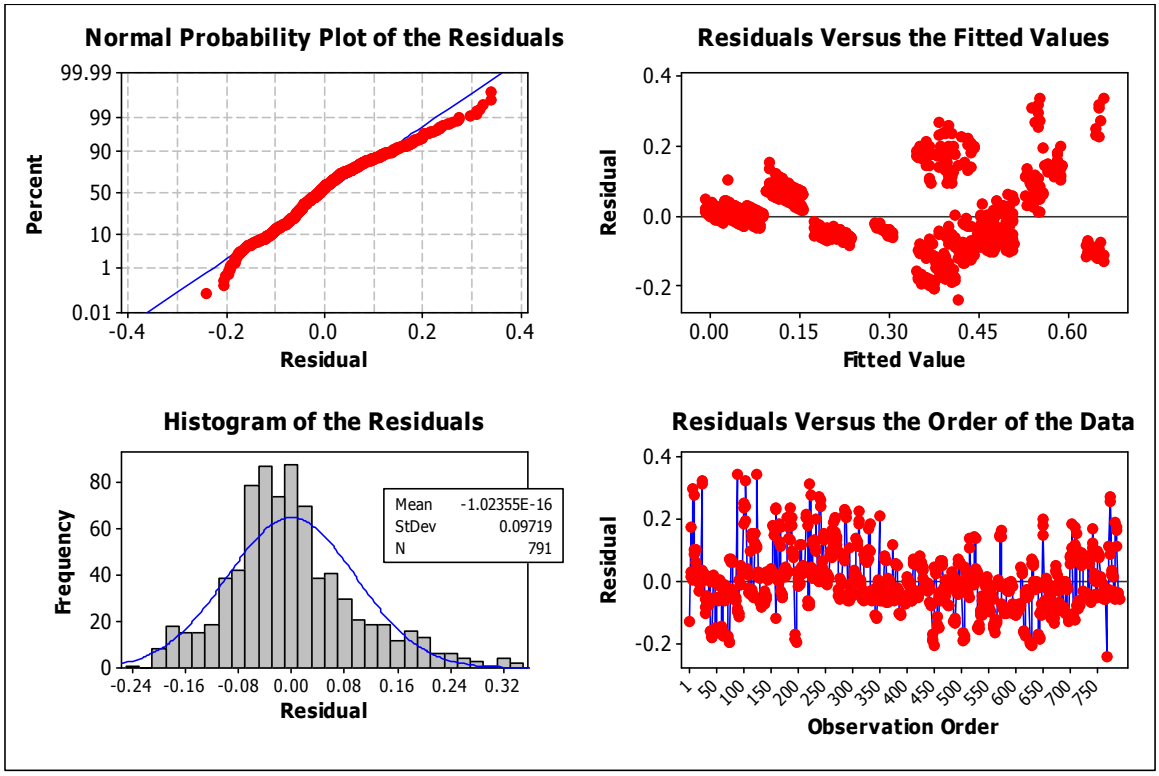

Figure 70. The residuals graphic for experimental apparent width at 5.08 mm (0.200 in.) depth.

Combined Width Results

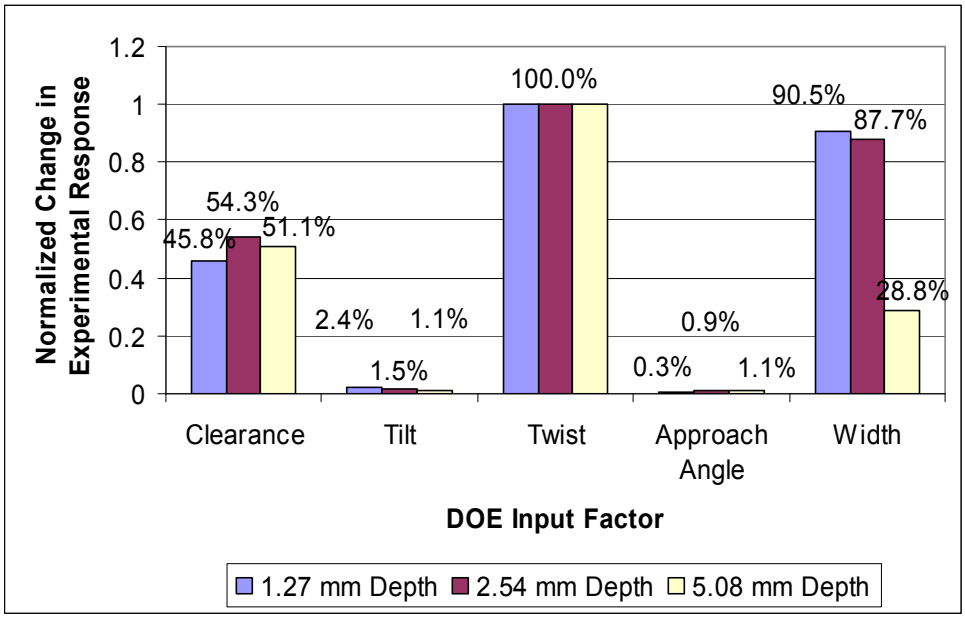

Figure 71. The combined relative influence of each of the input factors on apparent width response.

RCS Response

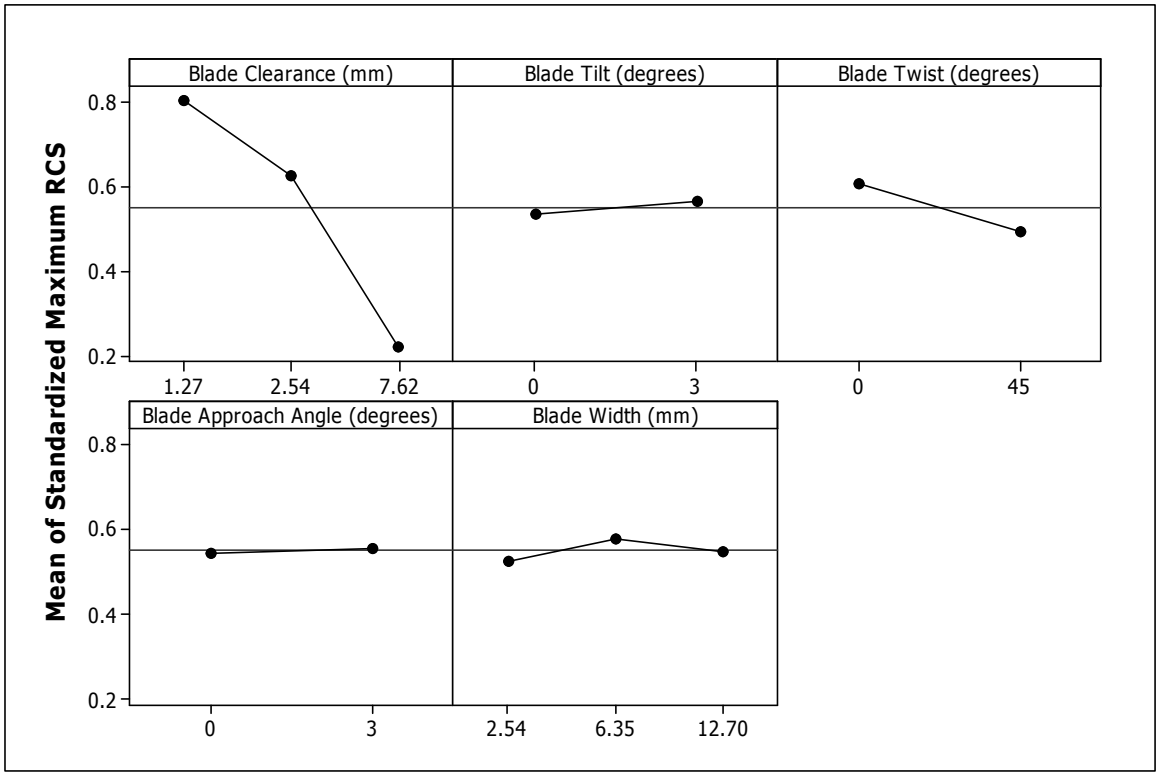

Figure 72. The main effects graphic for experimental RCS response.

Table 13. The full ANOVA table for experimental RCS response.

Source	DF	Seq SS	Adj SS	Adj MS	F	P
Blade Clearance (mm)	2	48.9628	48.592	24.296	6844.85	0.000
Blade Tilt (degrees)	1	0.18	0.1857	0.1857	52.32	0.000
Blade Twist (degrees)	1	2.5446	2.524	2.524	711.07	0.000
Blade Approach Angle (degrees)	1	0.0327	0.0337	0.0337	9.5	0.002
Blade Width (mm)	2	0.3565	0.3563	0.1781	50.18	0.000
Repetition	3	0.0101	0.0101	0.0034	0.95	0.415
Error	810	2.8751	2.8751	0.0035		
Total	820	54.962				
S	0.0595779					
R-Sq	0.9477					
Adjusted R-Sq	0.947					

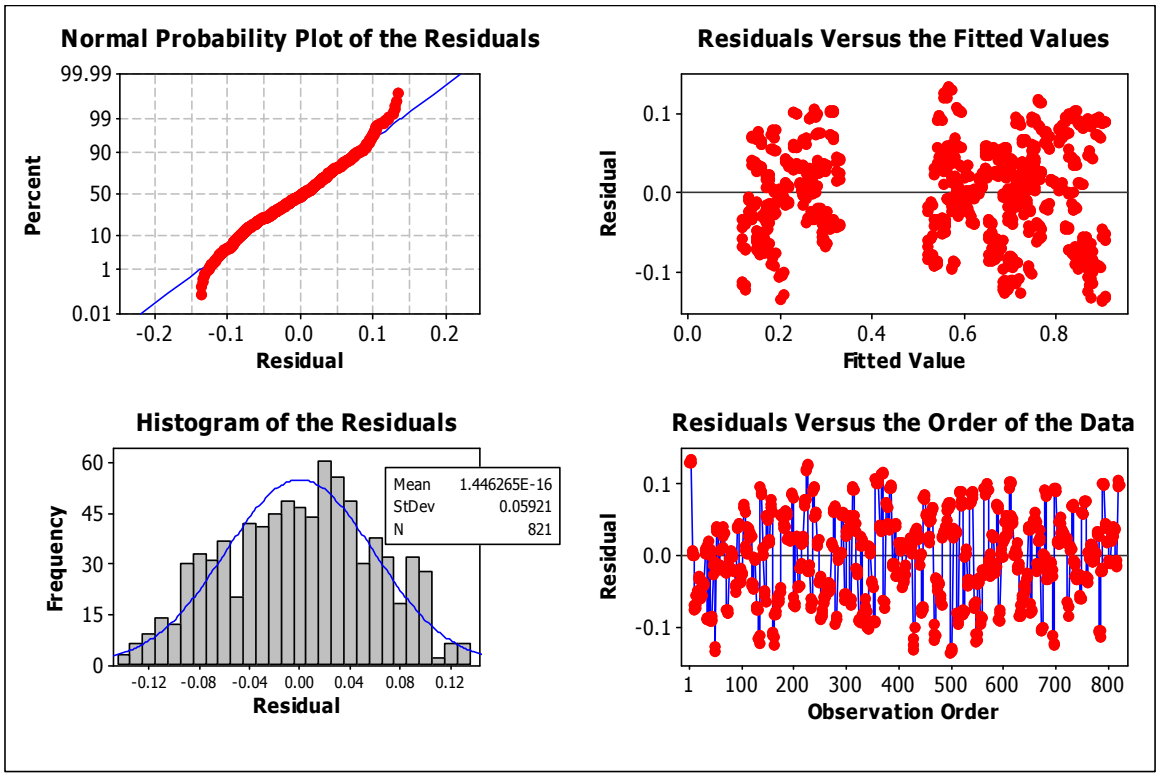

Figure 73. The residuals graphic for experimental RCS response.

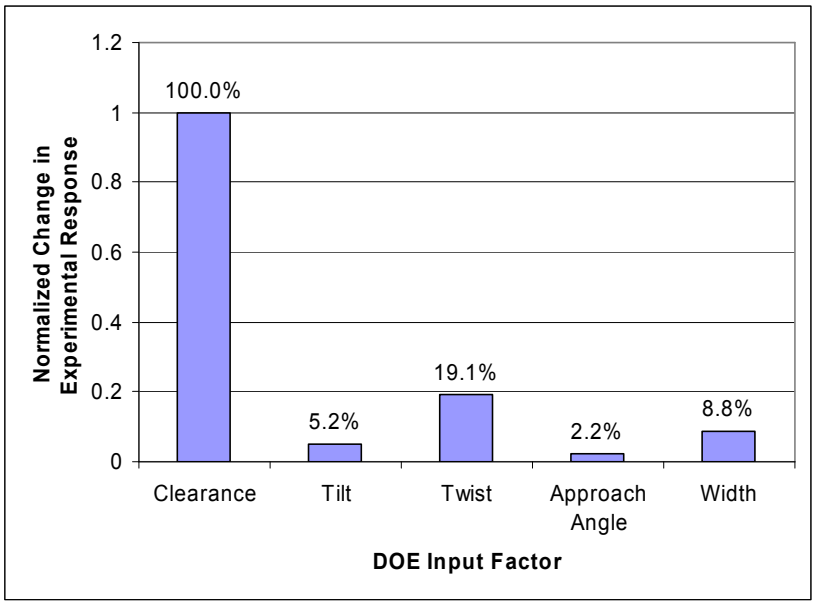

Figure 74. The relative influences of the input factors for experimental RCS response.

Model Results

Phase Response

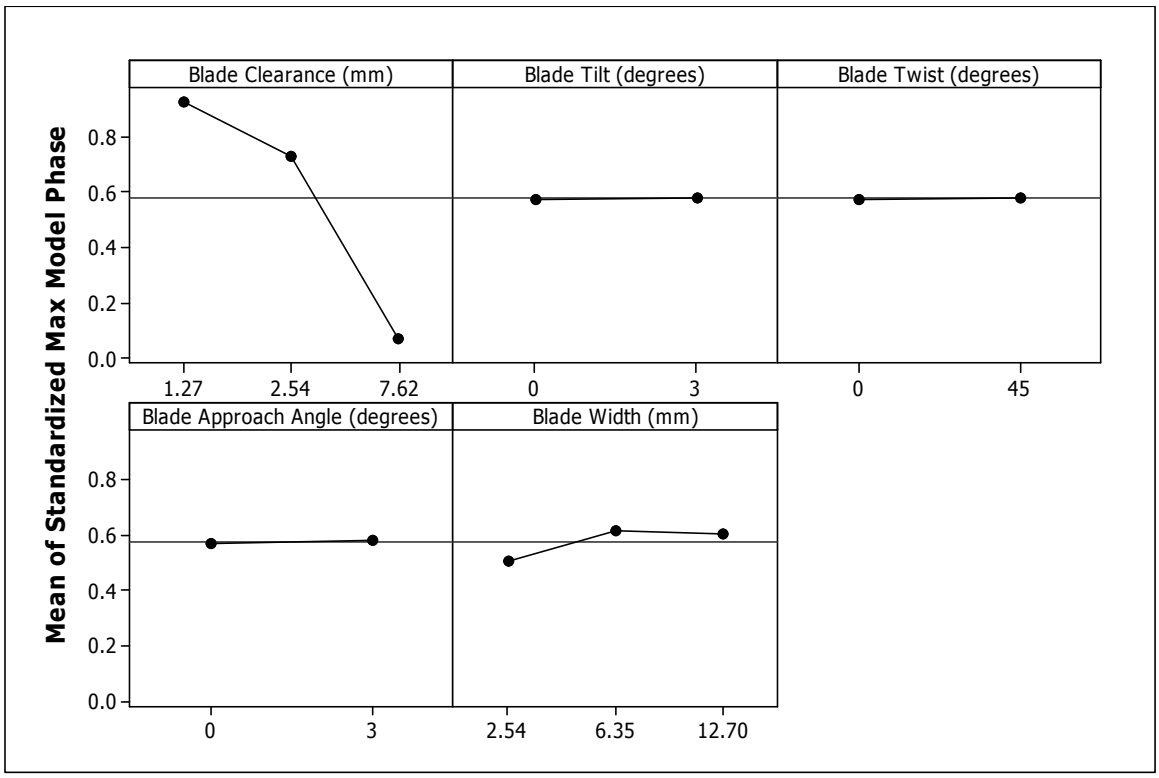

Figure 75. The main effects graphic for model phase response.

Table 14. The full ANOVA table for model phase response.

Source	DF	Seq SS	Adj SS	Adj MS	F	P
Blade Clearance (mm)	2	115.024	115.024	57.512	274496	0.000
Blade Tilt (degrees)	1	0.001	0.001	0.001	2.85	0.092
Blade Twist (degrees)	1	0.001	0.001	0.001	6.4	0.012
Blade Approach Angle (degrees)	1	0.012	0.012	0.012	57.69	0.000
Blade Width (mm)	2	2.213	2.213	1.107	5281.42	0.000
Repetition	3	0	0	0	0.03	0.994
Error	853	0.179	0.179	0		
Total	863	117.43				
S	0.0144748					
R-Sq	0.9985					
Adjusted R-Sq	0.9985					

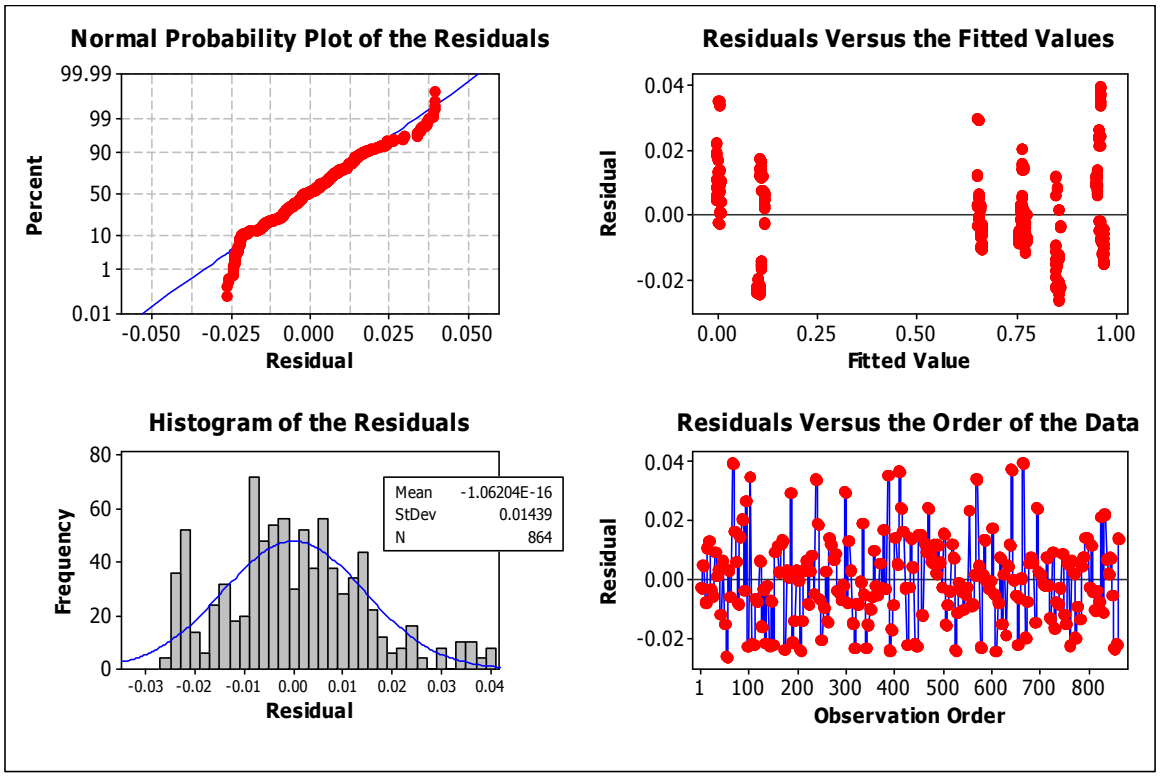

Figure 76. The residuals graphic for model phase response.

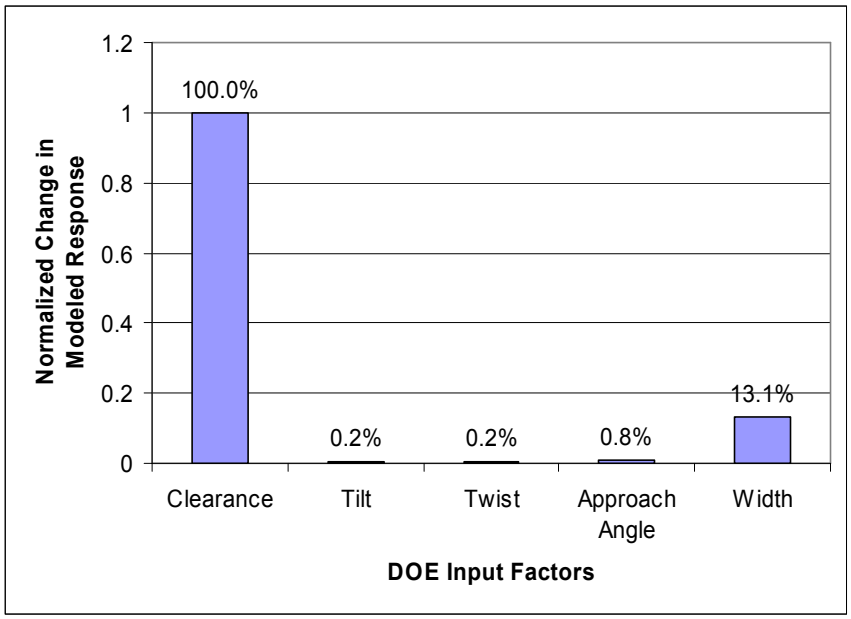

Figure 77. The relative influences of the input factors for model phase response.

Apparent Width Response

Apparent Width at 1.27 mm (0.0500 in.) Depth

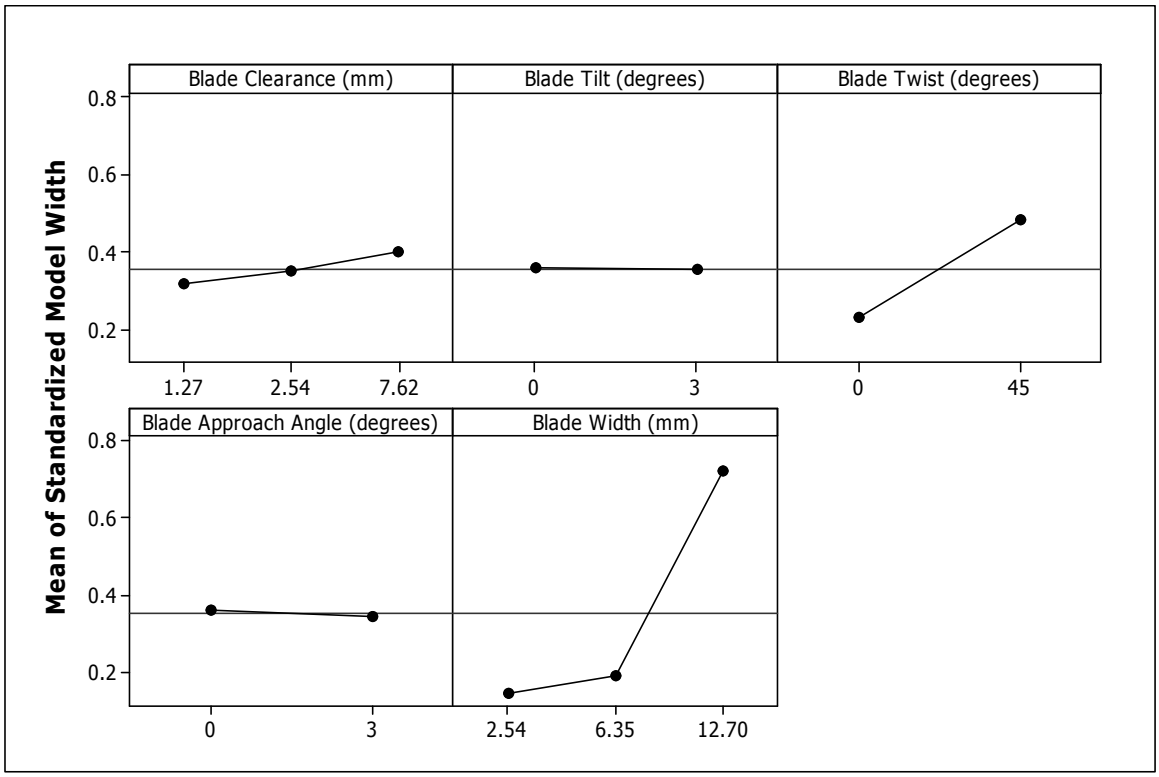

Figure 78. The main effects graphic for model apparent width at 1.27 mm (0.0500 in.) depth.

Table 15. The full ANOVA table for model apparent width at 1.27 mm (0.0500 in.) depth.

Source	DF	Seq SS	Adj SS	Adj MS	F	P
Blade Clearance (mm)	2	0.9743	0.9743	0.4871	129.44	0.000
Blade Tilt (degrees)	1	0.0023	0.0023	0.0023	0.6	0.439
Blade Twist (degrees)	1	13.8084	13.8072	13.8072	3668.84	0.000
Blade Approach Angle (degrees)	1	0.0799	0.0799	0.0799	21.24	0.000
Blade Width (mm)	2	58.0923	58.0863	29.0432	7717.34	0.000
Repetition	3	0	0	0	0	1.000
Error	853	3.2102	3.2102	0.0038		
Total	863	76.1673				
S	0.0613463					
R-Sq	0.9579					
Adjusted R-Sq	0.9574					

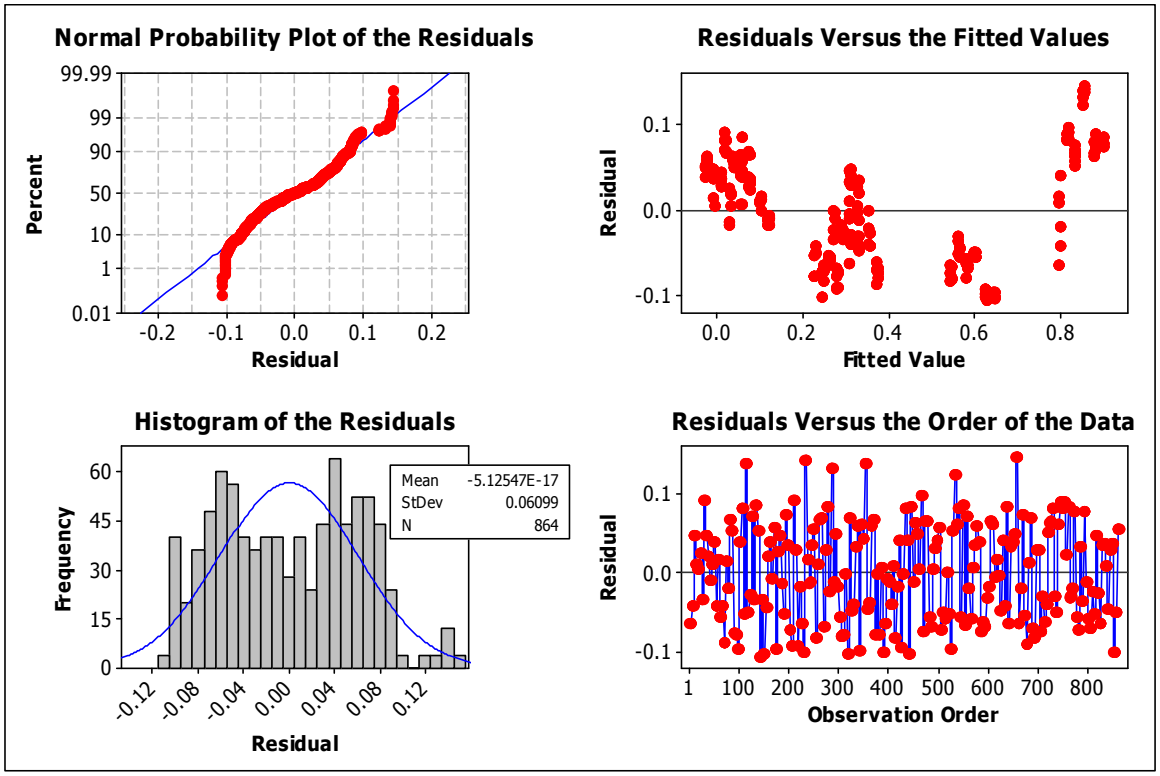

Figure 79. The residuals graphic for model apparent width at 1.27 mm (0.0500 in.) depth.

Apparent Width at 2.54 mm (0.100 in.) Depth

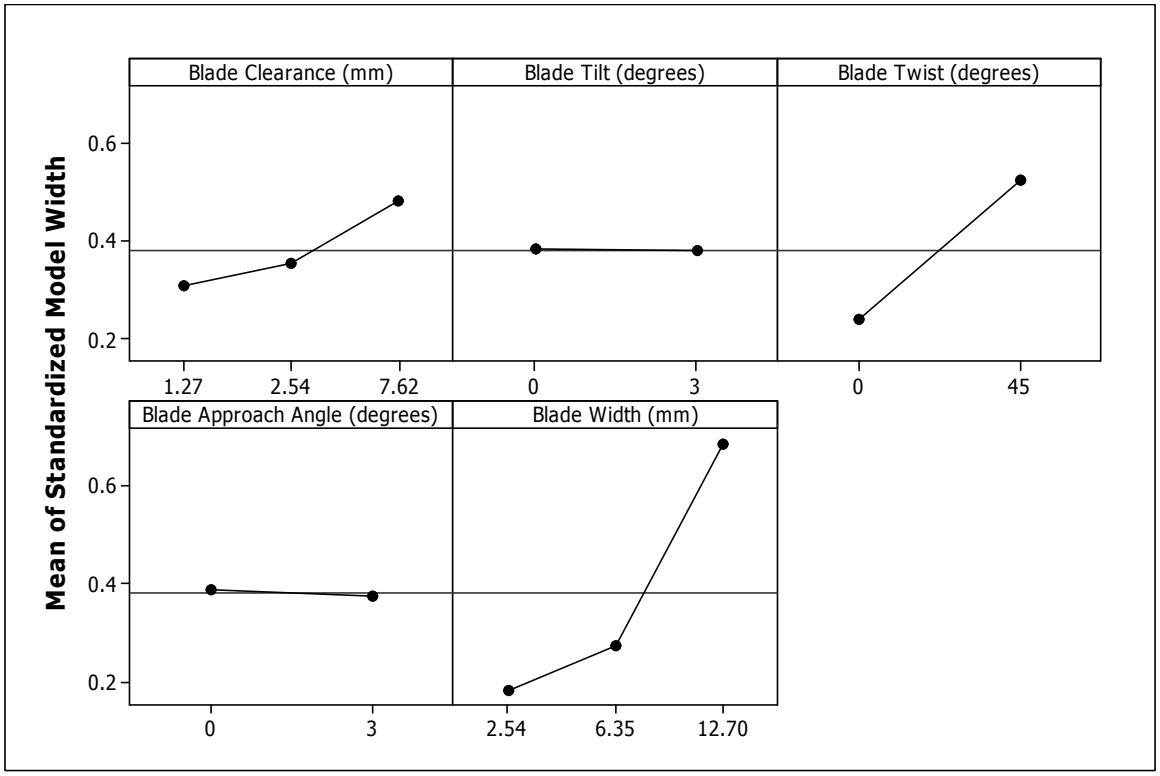

Figure 80. The main effects graphic for model apparent width at 2.54 mm (0.100 in.) depth.

Table 16. The full ANOVA table for model apparent width at 2.54 mm (0.100 in.) depth.

Source	DF	Seq SS	Adj SS	Adj MS	F	P
Blade Clearance (mm)	2	4.6707	4.6707	2.3353	790.85	0.000
Blade Tilt (degrees)	1	0.0008	0.0008	0.0008	0.26	0.610
Blade Twist (degrees)	1	17.2771	17.276	17.276	5850.44	0.000
Blade Approach Angle (degrees)	1	0.0366	0.0366	0.0366	12.41	0.000
Blade Width (mm)	2	41.3304	41.3249	20.6625	6997.24	0.000
Repetition	3	0	0	0	0	1.000
Error	853	2.5189	2.5189	0.003		
Total	863	65.8344				
S	0.054341					
R-Sq	0.9617					
Adjusted R-Sq	0.9613					

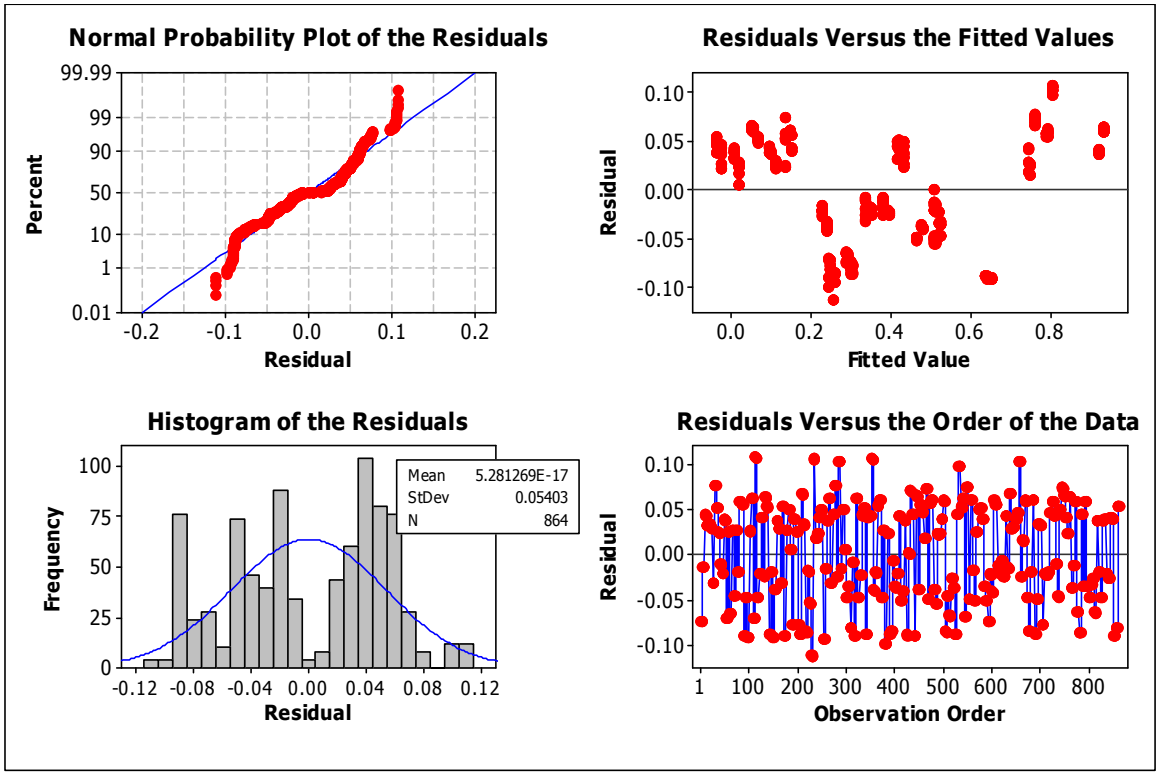

Figure 81. The residuals graphic for model apparent width at 2.54 mm (0.100 in.) depth.

Apparent Width at 5.08 mm (0.200 in.) Depth

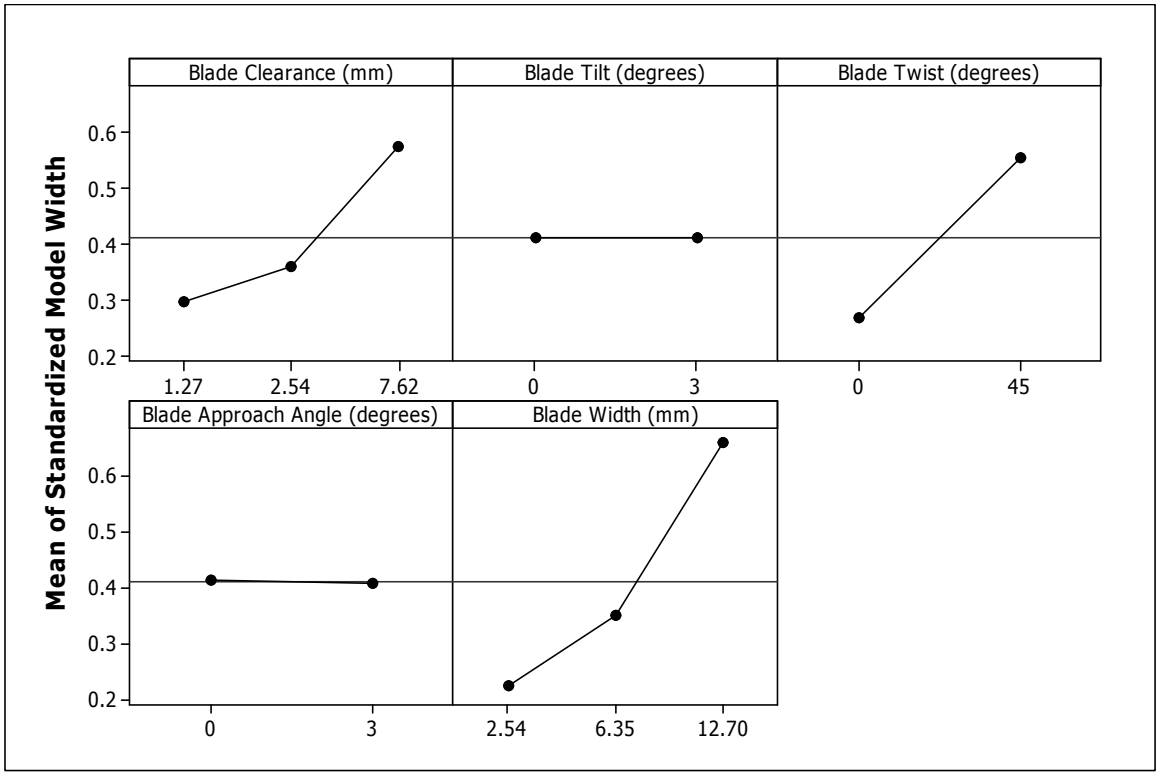

Figure 82. The main effects graphic for model apparent width at 5.08 mm (0.200 in.) depth.

Table 17. The full ANOVA table for model apparent width at 5.08 mm (0.200 in.) depth.

Source	DF	Seq SS	Adj SS	Adj MS	F	P
Blade Clearance (mm)	2	12.4419	12.4419	6.221	4587.36	0.000
Blade Tilt (degrees)	1	0.0004	0.0004	0.0004	0.28	0.594
Blade Twist (degrees)	1	17.9038	17.9027	17.9027	13201.5	0.000
Blade Approach Angle (degrees)	1	0.0097	0.0097	0.0097	7.18	0.008
Blade Width (mm)	2	28.5597	28.5555	14.2778	10528.45	0.000
Repetition	3	0	0	0	0.01	0.999
Error	853	1.1568	1.1568	0.0014		
Total	863	60.0723				
S	0.0368254					
R-Sq	0.9807					
Adjusted R-Sq	0.9805					

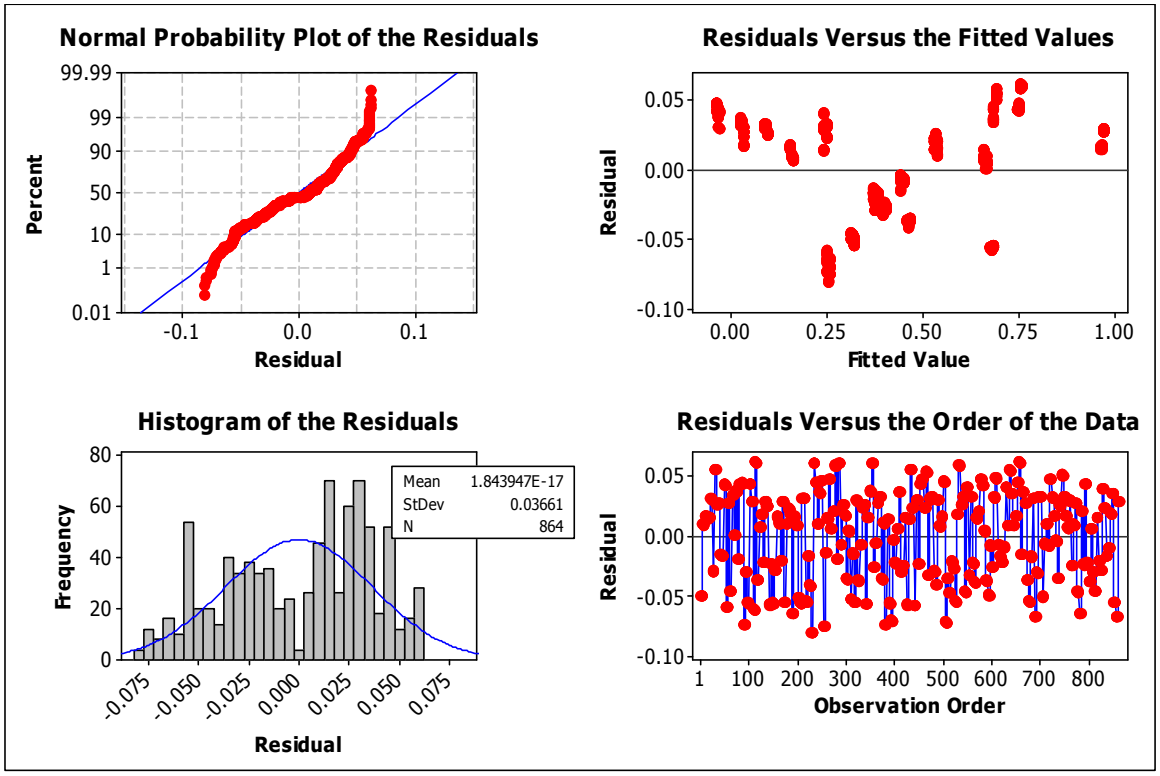

Figure 83. The residuals graphic for model apparent width at 5.08 mm (0.200 in.) depth.

Combined Width Results

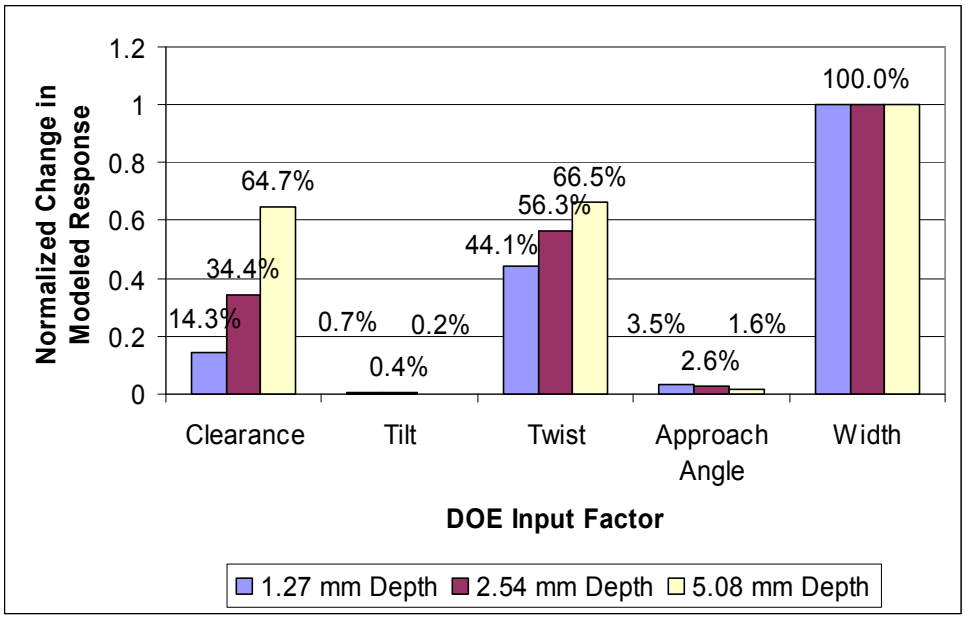

Figure 84. The combined relative influence of each of the input factors on apparent width response.

RCS Response

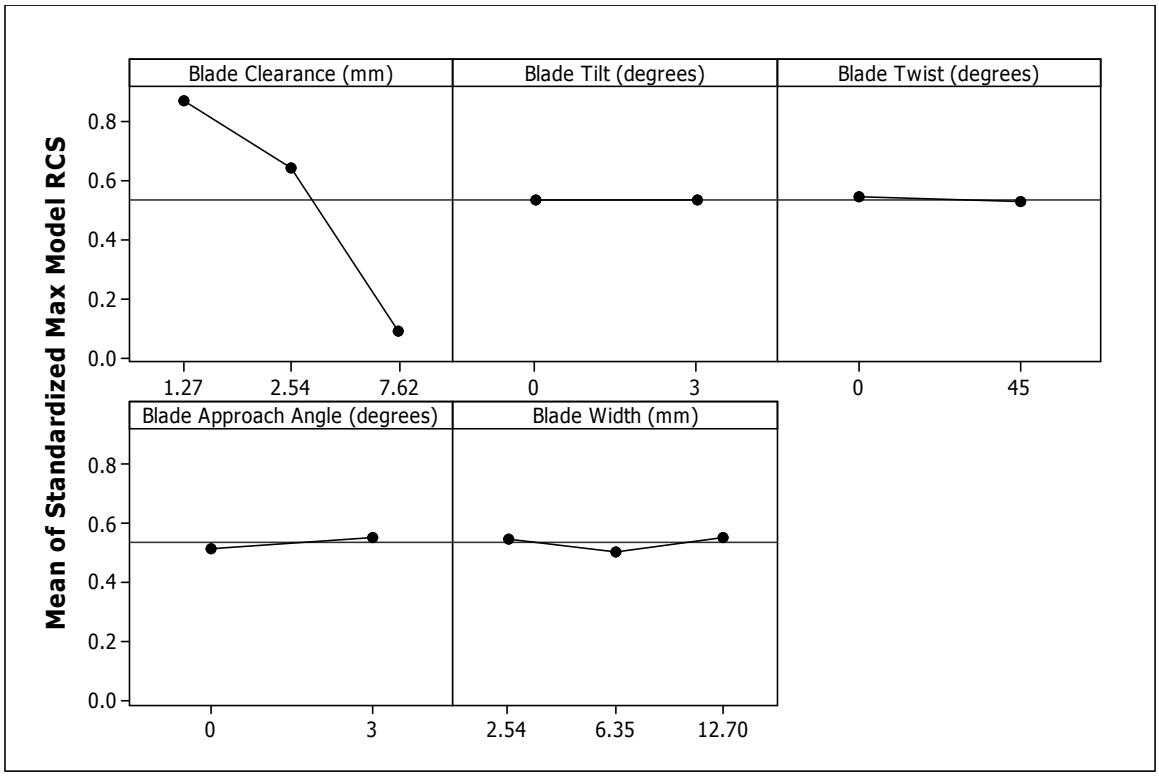

Figure 85. The main effects graphic for model RCS response.

Table 18. The full ANOVA table for model RCS response.

Source	DF	Seq SS	Adj SS	Adj MS	F	P
Blade Clearance (mm)	2	93.8414	93.7861	46.8931	16025	0.000
Blade Tilt (degrees)	1	0.0003	0.0004	0.0004	0.14	0.713
Blade Twist (degrees)	1	0.0577	0.0583	0.0583	19.93	0.000
Blade Approach Angle (degrees)	1	0.3427	0.3406	0.3406	116.4	0.000
Blade Width (mm)	2	0.3921	0.3921	0.1961	67	0.000
Repetition	3	0.0006	0.0006	0.0002	0.07	0.978
Error	849	2.4844	2.4844	0.0029		
Total	859	97.1191				
S	0.0540948					
R-Sq	0.9744					
Adjusted R-Sq	0.9741					

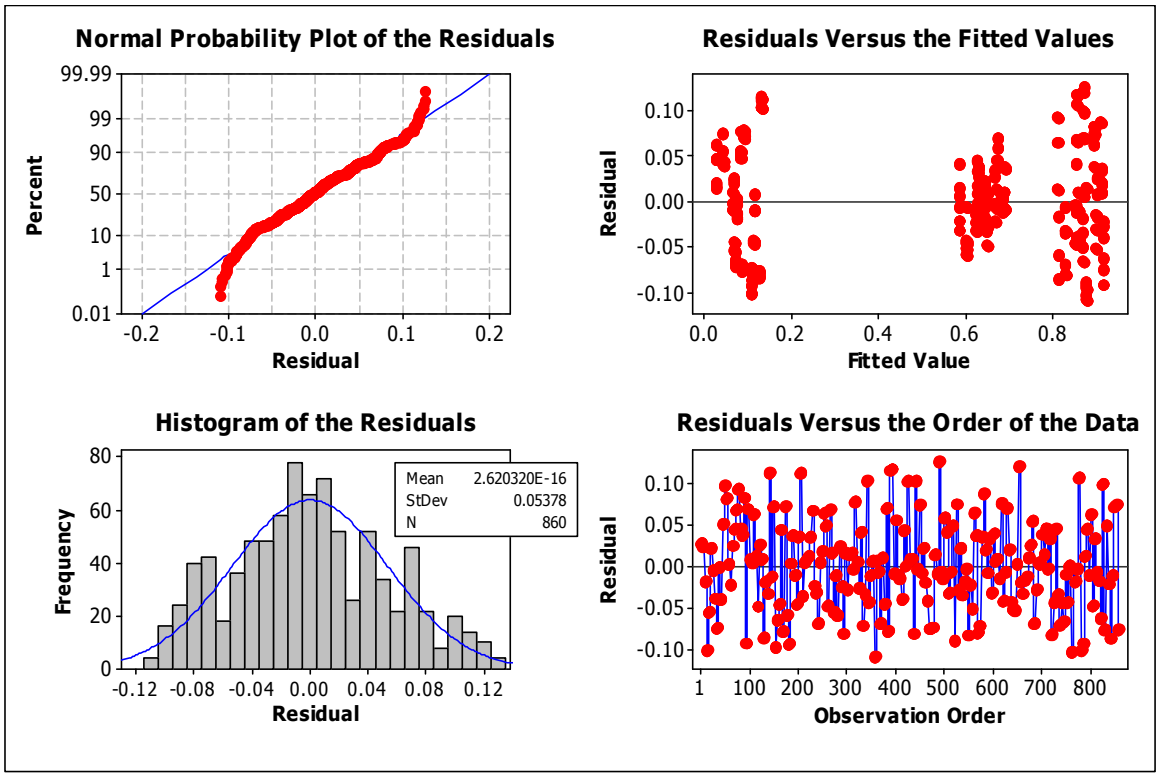

Figure 86. The residuals graphic for model RCS response.

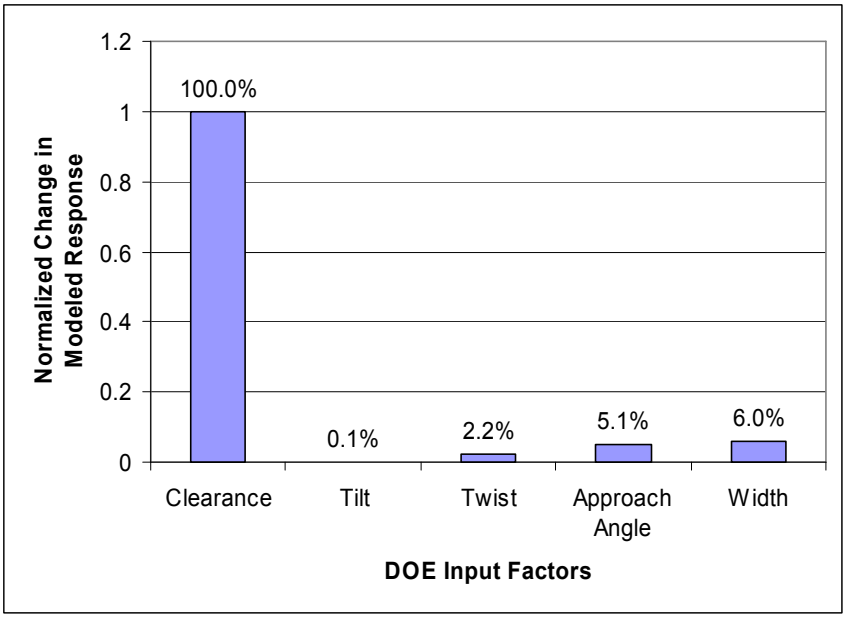

Figure 87. The relative influences of the input factors for model RCS response.

Combined Results

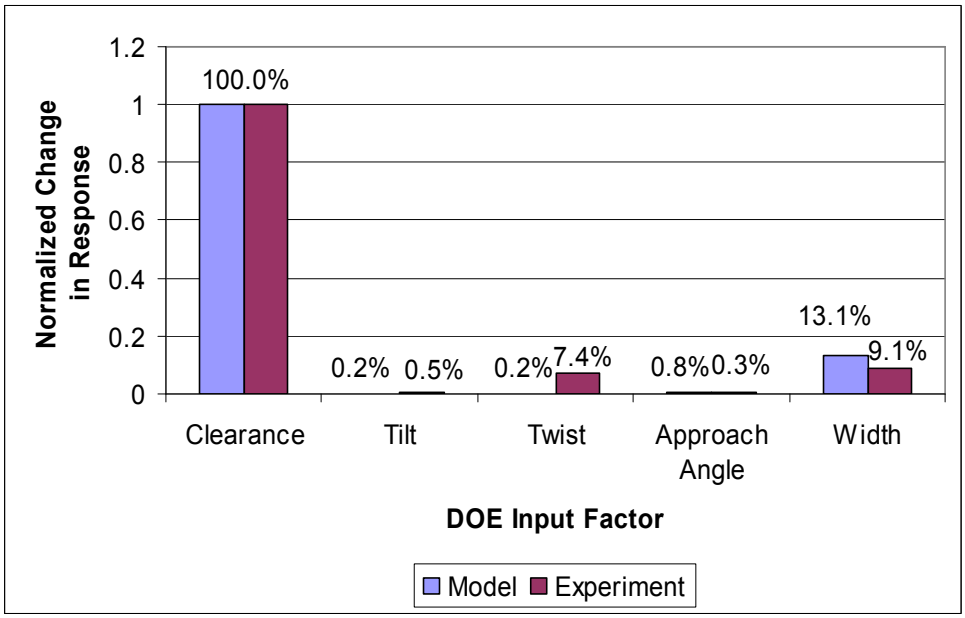

Figure 88. The combined relative influences of the input factors for model and experimental phase response.

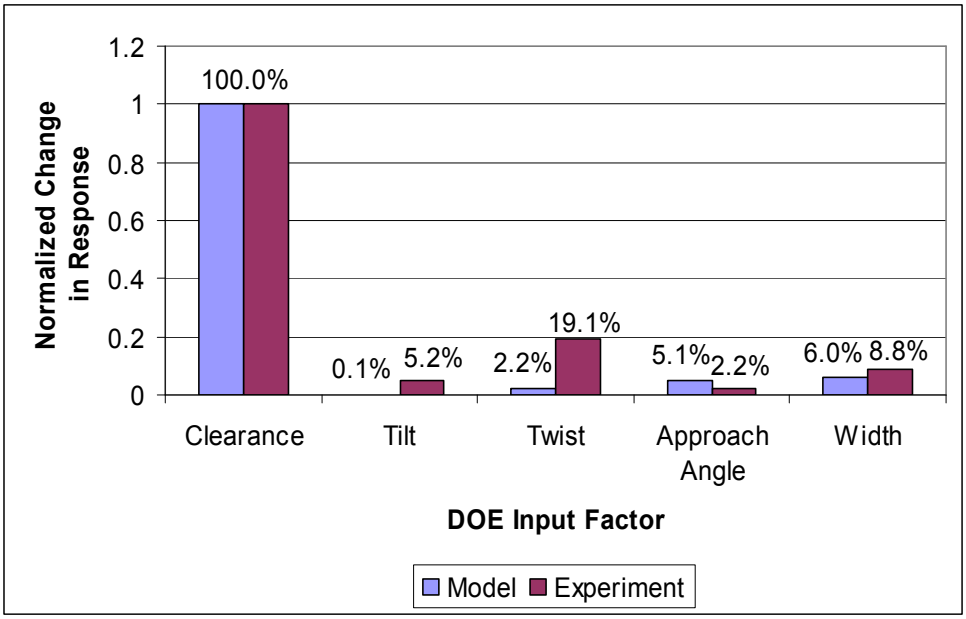

Figure 89. The combined relative influences of the input factors for model and experimental RCS response.

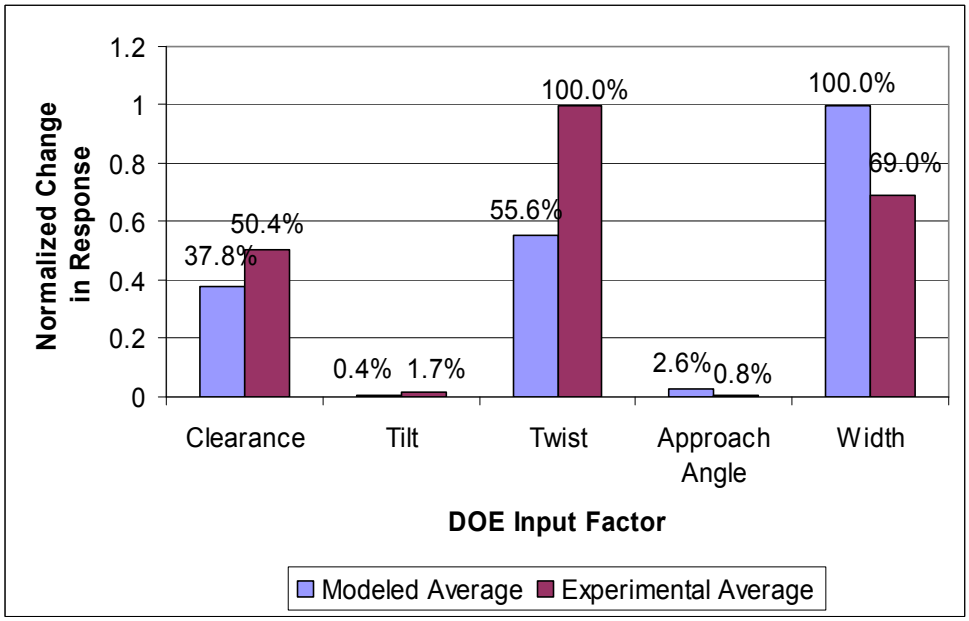

Figure 90. The combined relative influences of the input factors for model and experimental average apparent width response.

REFERENCES

Bailleul, G. D. and S. Albijat. "Review of Progress in the Development of Capacitive Sensors for Blade Tip Clearance Measurement," ASME 96-TA-1, 1996.

Bannister, R.L. and N.S. Cheruvu. "Turbines for the turn of the century," *Mechanical Engineering*, vol. 116 Issue 6 pp. 68-75, June 1994.

Belsterling, C. "Sensing with air." *Instrumentation Science and Technology*, vol. 18, no. 3, pp. 37-41, March 1971.

Bhaumik, S.K., T.A. Bhaskaran, R. Rangaraju, M.A. Venkataswamy, M.A. Parameswara and R.V. Krishnan. "Failure of turbine rotor blisk of an aircraft engine," *Engineering Failure Analysis 9*, pp. 287-301, 2002.

Bret, M. *Image Synthesis*, Dordrecht: Kluwer Academic Publishers, 1992.

Cazaux, J. "Errors in nanometrology by SEM. *Nanotechnology,* 15, pp. 1195-1199, 2004.

Chivers, J. W. H. "A Tecnnique for the Measurement of Blade Tip Clearance in a Gas Turbine," AIAA-89-2016, 1989.

Christodoulou, L. "Prognosis," Bidder's Conference and Workshop. DARPA/DSO. Alexandria, VA. 27 September 2002.

Chuckpaiwong, I. "Development of Position Sensor Using Phased-Based Continuous Wave Radar," PhD Thesis, Georgia Institute of Technology. Atlanta, GA, 2003.

Chuckpaiwong, I., S. Billington, J. Geisheimer, and T. Kurfess. "Development of A High Resolution Radar–Based Position Sensor," *ISA Emerging Technologies 2002,* Chicago, 2002.

Cohen, H., G. F. C. Rogers and H. I. H. Saravanamutto. *Gas Turbine Theory*, 3rd ed., New York: Longman Group UK Limited, 1987.

Cotgrove, R.M, and M.I. Wood. "Opportunities for advanced sensors for condition monitoring of gas turbines," Opportunities and Advances in International Power Generation, 18-20th March 1996, Conference Publication No. 419, IEE, pp. 119-124, 1996.

Davidson, D. P., R. D. DeRose and A. J. Wennerstrom. "The Measurement of Turbomachinery Stator-to-Drum Running Clearances," ASME 83-GT-204, 1983.

Dhadwal, H. S. and A. P. Kurkov. "Dual-Laser Probe Measurement of Blade-Tip Clearance," International Gas Turbine & Aeroengine Congress & Exhibition. ASME 98-GT-183, 1998.

Drumm, M., and W. Haase. "High performance rotor health monitoring," IEEE 0-7803-6395-7/00, pp. 6.E.4-1—6.E.4-8, 2000.

Ennos, A. E. and M. S. Virdee. "Precision Measurement of Surface Form by Laser Profilometry," *Wear*, 109, pp. 275-286, 1986.

Fabian, T., S. Kang and F. Prinz. "Capacitive blade tip clearance measurements for a micro gas turbine," IEEE Instrumentation and Measurement Technology Conference. Anchorage, USA. 21-23 May 2002.

Gallardo, J.M., J.A. Rodríguez and E.J. Herrera. "Failure of gas turbine blades," *Wear 252*, pp264-268, 2002.

Geisheimer, J., G. Greneker and S. Billington. *Phase-based sensing system,* United States Patents, *6489917*, December 3, 2002.

Gill, S. J., M. D. Ingallinera and A. G. Sheard. "Turbine Tip Clearance Measurement System Evaluation on an Industrial Gas Turbine," ASME 97-GT-466, 1997.

Giubbolini, L. "A Multistatic Microwave Radar Sensor for Short Range Anticollision Warning," *IEEE Tranactions on Vehicular Technology*, vol. 49, no. 6, pp. 2270-2275, November 2000.

Grzybowski, R., G. Foyt, W. Atkinson, W. Knoell, J. Wenger and D. Benz. "Microwave Blade Tip Clearance Measurement System," ASME 96-GT-2, 1996.

Hardman, B. "A Prognostic Development Methodology with Demonstration Examples," DARPA/DSO Prognosis Bidder's Conference. Alexandria, VA. 26-27 September 2002.

Hess, A. "The Prognostic Requirement for Advanced Sensors and Non-Traditional Detection Technologies," DARPA/DSO Prognosis Bidder's Conference. Alexandria, VA. 26-27 September 2002.

Holmes, David W. *Sensors and Methods for Sensing Displacement Using Radar*, United States Patents, 5760731, June 2, 1998.

Johnson, R. C., ed. *Antenna Engineering Handbook*, 3rd ed., New York: McGraw-Hill, 1993.

Jones, R. and M.S. Hazell. "The in-situ measurement of aero-engine blade flab using an optical sensor," *IEE Colloquium on 'Advanced Vibration Measurements, Techniques and Instrumentation for the Early Prediction of Failure'*, no. 105, London, 8 May 1992.

Karpur, P., B. G. Frock and P. K. Bhagat. "Wiener Filtering for Image Enhancement in Ultrasonic Nondestructive Evaluation," *Materials Evaluation*, pp. 1374-1379, 1990.

Kawasima, T., H. IINUMA and N. Minagawa. "Optical Semiconductor Blade Vibration Monitoring System for Gas Turbine Engine," *IMTC '94*, pp 601-605, Hamamatsu, May 10-12, 1994.

Kourtiche D., L. Ait Ali, L. Alliès and A. Chitnalah. "Harmonic propagation of finite-amplitude sound beams: second harmonic imaging in ultrasonic reflection tomography," *Measurement Science and Technology*, 15, pp. 21-28, 2004.

Mattern, D. and L. Jaw. "Experimental results of an active tip clearance control System for a centrifugal compressor," ASME 97-GT-32, 1997.

Mazzucato, E. "Microwave imaging reflectometry for the visualization of turbulence in tokamaks," *Nuclear Fusion*, vol. 41, no. 2, pp 203-213, 2001.

Mehrdadi, B., B. Kaghazchi and M.S. Beck. "Non-contacting level measurement of irregular surfaces using coded ultrasound and cross correlation analysis," *J. Phys. E: Sci. Instrum.,* vol 15, pp. 367-372, 1982.

Müller, D., A. G. Sheard, S. Mozumdar and E. Johann. "Capacitive Measurement of Compressor and Turbine Blade Tip to Casing Running Clearance," ASME 96-GT-349, 1996.

Neter, J., M. H. Kutner, C. J. Nachtsheim and W. Wasserman. *Applied Linear Statistical Models*, 4th ed., Chicago: Times Mirror Higher Education Group, 1996.

Novak, J. and Miks, A. "Modern Optoelectronic Methods for Non-Contact Deformation Measurement in Industry," *Journal of Optics A: Pure and Applied Optics*, vol. 4, pp. S413-S420, November 2002.

Pahk, H., J. Kim, and K. Lee. "Integrated Real Time Compensation System for Errors Introduced by Measurement Probe and Machine Geometry in Commercial CMMS," *Int. J. Mach Tools Manufact*, vol. 36, no. 9, pp. 1045-1058, 1996.

Richards, M. A. *Fundamentals of Radar Signal Processing*, Book Manuscript, 2002.

Rickman, Jr., J. D. "Eddy Current Turbocharger Blade Speed Detection," *IEEE Transactions on Magnetics*, vol. MAG-18, no. 5, pp. 1014-1021, 1982.

Roeseler, C., A. von Flotow and P. Tappert. "Monitoring Blade Passage in Turbomachinery Through the Engine Case (No Holes)," IEEE 0-7803-6599-2/01, pp. 6-3125--6-3129, 2002.

Salam, I., A. Tauqir and A.Q. Khan. "Creep-fatigue failure of an aero engine turbine blades," *Engineering Failure Analysis* 9, pp. 335-347, 2002.

Sheard, A. G. and B. Killeen. "A Blade by Blade Tip Clearance Measurement System for Gas Turbine Applications," ASME 94-GT-40, 1994.

Sheard, A. G. and S. R. Turner. "Electromechanical Measurement of Turbomachinery Blade Tip-to-Casting Running Clearance," ASME 92-GT-50, 1992.

Shen, Y. and M. E. Springer. "A Robust Pretravel Model for Touch Trigger Probes in Coordinate Metrology," *Transactions of the ASME*, vol. 120, pp. 532-539, 1998.

Skolnik, M. I. *Introduction to Radar Systems*, New York: McGraw-Hill, 1962.

Sullivan, R. J. *Microwave Radar Imaging and Advanced Concepts*, Boston: Artech House, 2000.

Tappert, P., A. von Flotow and M. Mercadal. "Autonomous PHM with Blade-Tip Sensors: Algorithms and Seeded Fault Experience," IEEE 0-7803-6599-2/01, pp. 7-3287--7-3295, 2001.

Wagner, M., A. Schulze, M. Vossiek, C. Stephelbauer, R. Weigel, N. Vortmeyer and P. Heide. "Novel microwave vibration monitoring system for industrial power generating turbines," *1998 IEEE MTT-S International Microwave Symposium Digest,*, vol. 3, pp. 1211-1214, 1998.

Walsh, Philip P. and P. Fletcher. *Gas Turbine Performance*, 2nd ed., Malden: Blackwell Science, 2004.

Wang, X. C., F. J. Xi, D. Li and Z. Qin. "Estimation and Control of Vibrations of Circular Saws," Proceedings of the 1999 IEEE International Conference on Control Applications, pp. 514-520. Kohala Coast-Island of Hawaii, Hawaii. 22-27 August 1999.

You, D., M. Want and P. Moin. "Large- Eddy Simulation and Analysis of Tip-Clearance Flows in Turbomachinery Applications," *Proceedings of the 2003 IEEE User Group Conference.*